ABSTRACT

Title of dissertation: FRUSTRATED MAGNETISM AND ELECTRONIC PROPERTIES OF HOLLANDITE OXIDE MATERIALS

Amber M. Larson, Doctor of Philosophy, 2017

Dissertation directed by: Professor Efrain E. Rodriguez
Department of Chemistry and Biochemistry

Microporous transition metal oxides with the hollandite structure type have been prepared by standard solid-state techniques with varying compositions. With a nominal formula of $A_xM_8O_{16}$ and a framework of edge and corner-sharing MO_6 octahedra, hollandites feature a pseudo-one dimensional tunnel occupied loosely by cation A. The metastability of these open-framework materials, combined with the ability of accommodating a variety of redox-active transition metals leads to unique and indispensable properties. Inherent to the triangular connectivity of the M cations in the hollandite framework, these materials frequently exhibit frustrated magnetic behavior.

This thesis demonstrates that it is possible to significantly affect the magnetic and transport properties of these microporous materials through tuning of their chemical compositions. We have shown that it is possible to synthesize polycrystalline and single crystal hollandite materials under ambient conditions utilizing salt flux techniques. Our efforts to characterize the structure-property relationships provide some of the first magnetic structure determinations of these complex

frameworks. The interesting behavior of these materials is a result of the interplay between charge, orbital, and spin degrees of freedom.

This work shows that the hollandite framework is quite versatile, leading to the real possibility of tuning the material properties to achieve desired effects and opening up many potential applications for these microporous oxides.

FRUSTRATED MAGNETISM AND ELECTRONIC PROPERTIES OF HOLLANDITE OXIDE MATERIALS

by

Amber Marie Larson

Dissertation submitted to the Faculty of the Graduate School of the
University of Maryland, College Park in partial fulfillment
of the requirements for the degree of
Doctor of Philosophy
2017

Advisory Committee:
Professor Efrain E. Rodriguez, Chair/Advisor
Professor Bryan Eichhorn
Professor Johnpierre Paglione
Professor Lawrence R. Sita
Professor Andrei Vedernikov

© Copyright by
Amber M. Larson
2017

Dedication

For Christian, Camille, and all of my family.

Acknowledgments

First and foremost I would like to thank Professor Efrain Rodriguez for his guidance and support. It has been a pleasure to work with and learn from such an extraordinary scientist. I am grateful for the opportunity he has given me to work on interesting and challenging projects over the past several years, and also for his kindness and patience as I have navigated graduate school while becoming a mother. Gratitude is also due the past and present members of the Rodriguez group. Their friendships and discussions have provided valuable insights into chemistry, physics, and life.

I would especially like to thank the support scientists at NCNR and the user facilities at University of Maryland, particularly Craig Brown, Jeff Lynn, Juscelino Leao, Peter Zavalij, and Karen Gaskell. I would also like to thank Professors Bryan Eichhorn, Lawrence Sita, Andrei Vedernikov, and Johnpierre Paglione for serving on my thesis committee and sparing their time to review this manuscript. I am grateful for the financial support I received from the National Institute of Standards and Technology (NIST) Center for Neutron Research (NCNR).

Finally, I owe my deepest thanks to my family. Christian and Camille, I love you more than anything. Words can not express the gratitude owed to my parents, who have always stood by and guided me. And special thanks goes to my grandmother, Mollyanne Hopkins, who sacrificed food, sleep and time to help me study for my AP Chemistry exam all those years ago.

Contents

List of Tables

List of Figures

List of Abbreviations

χ	magnetic susceptibility
λ	wavelength
μ_{eff}	effective magnetic moment
θ	angle of diffraction
θ_{CW}	Curie-Weiss temperature
AFM	Antiferromagnetim
BCMO	$Ba_{1.2}Co_xMn_{8-x}O_{16}$
BMO	$Ba_{1.2}Mn_8O_{16}$
BVO	$Bi_{1.7}V_8O_{16}$
CMR	Colossal Magnetoresistance
CW	Constant Wavelength
DM	Dzyaloshinsky-Moriya
FC	Field-cooled
FM	Ferromagnetism
H	Magnetic field
HIPD	High-Intensity Powder Diffractometer
ICP-AES	Inductively Coupled Plasma Atomic Emission Spectroscopy
ICP-MS	Inductively Coupled Plasma Mass Spectrometry
J	Magnetic exchange interaction
JT	Jahn-Teller
LANL	Los Alamos National Lab
LNSC	Lujan Neutron Scattering Center
M	Magnetization
MPMS	Magnetic Property Measurement System
MIT	Metal-Insulator Transition
NIST	National Institute of Standards and Technology
NCNR	NIST Center for Neutron Research
NPD	Neutron Powder Diffraction
PPMS	Physical Property Measurement System
Q	Momentum transfer
S	Magnetic spin
SQUID	Superconducting QUantum Interference Device
TOF	Time of Flight
UMD	University of Maryland
XPS	X-ray Photoelectron Spectroscopy
XRD	X-ray Diffraction
ZFC	Zero-field cooled

Chapter 1: Introduction

Transition metal oxides are a broad class of materials that display a uniquely wide range of electronic properties. The range of potential applications for transition metal oxides is vast, and chemists play a vital role in the synthesis and characterization of new materials. Chemical thinking, connecting the composition and the atomic structure of a material to their observed physical and electronic behaviors is essential for continued innovations and advances of technology.

Transition metal oxides with relatively open structures can be found in the form of the so-called octahedral molecular sieves (OMS).[1–5] Figure 1.1 shows a variety of Mn-based OMS materials, many of which are found naturally as mineral deposits. Growing interest in these compounds for potential technological applications has led to the development of synthetic analogues to these structure types.[6] As the name implies, the transition metals in OMS are octahedrally coordinated to oxide anions, with the connectivity of the octahedra creating microporous tunnels through the material. The general formula for OMS-materials is A_xMO_2 where the A cation is a non-framework cation, typically an alkali or alkaline earth metal, and the B cation is the framework transition metal, often a redox-active transition metal.[7]

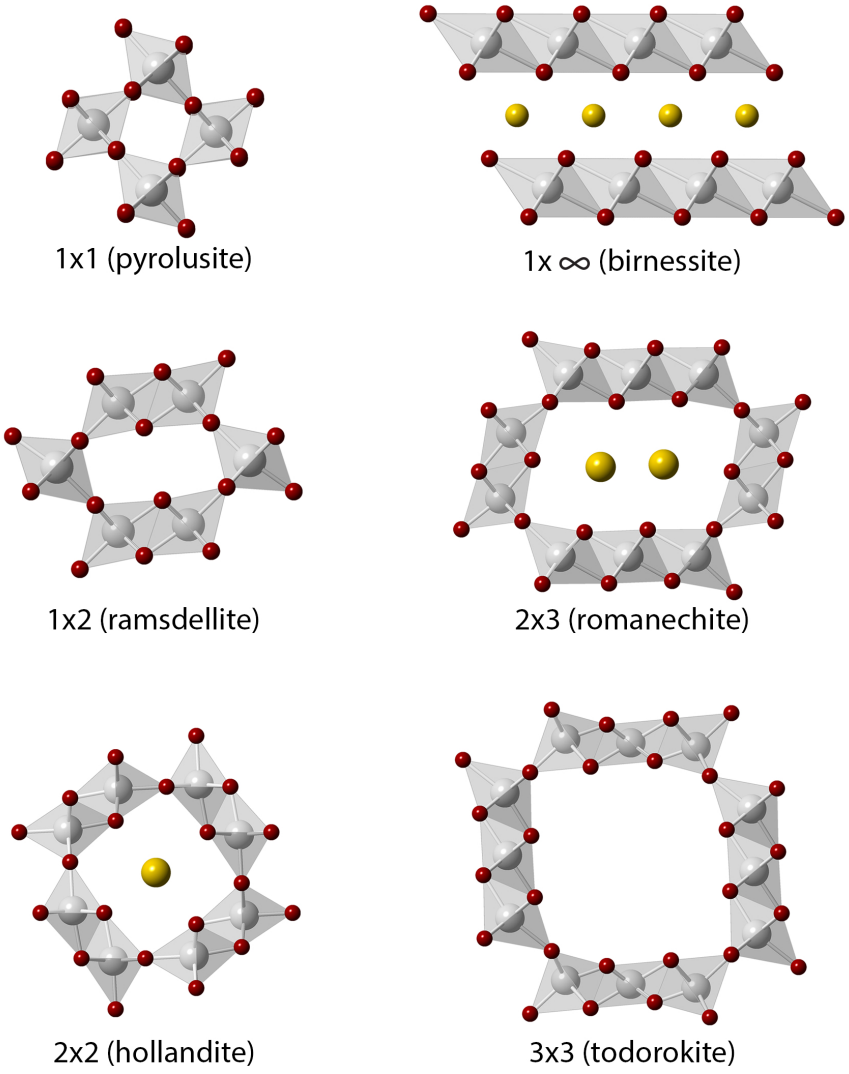

Figure 1.1: Schematic representation of different octahedral molecular sieve materials, showing the tunnel and layered structures formed by the MO_6 octahedral units. The mineral names provided are for A_xMO_2 materials with M = Mn.

These OMS materials with regular and open porous structures are generally metastable with respect to their denser phases,[8] and their existence arises from preparation under special reaction conditions.[9] The metastability of porous materials leads to unique and indispensable properties such as catalytic conversion of petroleum products into fuels and common feedstocks by zeolites.[10,11]

Motivated by the success of OMS-materials, zeolites, and other porous inorganic compounds, we have studied the hollandite OMS phase since it displays significant flexibility in accommodating different transition metals in its framework. This thesis details investigations of $A_xM_8O_{16}$ hollandites, primarily focusing on compositions where B = V or Mn and the physical properties arising from their crystalline structures.

1.1 Magnetic frustration

What is life without a little frustration from time to time? In physics, frustration often leads to exotic properties in materials. In this context, frustration refers to the existence of competing forces in a material, which cannot be satisfied simultaneously.[12–14]

Two geometric motifs recur frequently in materials studied for their magnetic frustration. In a structure featuring a triangular motif of Ising spins,[1] where the moment is constrained to point in one of two directions, three magnetic moments, each localized at one corner of the triangle, cannot mutually satisfy a preferred

[1] More details on magnetism and exchange mechanisms are discussed in Section 2.4.1.

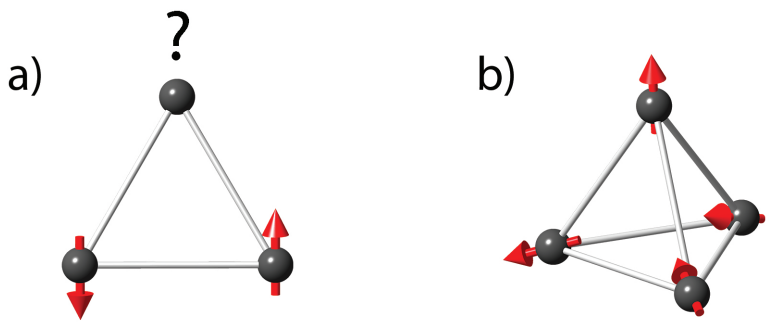

Figure 1.2: a) Magnetic frustration of a triangular Ising lattice when spins are coupled antiferromagnetically. b) Magnetic frustration in a tetrahedral 'spin-ice' model.

nearest-neighbor antiparallel arrangement (left side of Figure 1.2). Instead, the spins fluctuate, or order, in a less obvious manner. These systems are believed to not order elegantly at a single energy minimum, but instead display a large degeneracy of equally unsatisfied states as the ground state of the system.[15,16] In these systems, only short-range correlations between spins are found for all temperatures, $T > 0$. Analogous to the correlated state of molecules in an ordinary liquid, a triangular Ising antiferromagnetic network of spins has been termed a 'spin liquid' or described as a cooperative paramagnet.[12,17–20]

Frustrated arrangements of moments localized on tetrahedral corners have also been studied, where ferromagnetic nearest-neighbor exchange energies are stymied by the different Ising axes of the spins. To minimize the energy of this frustration, six different, energetically equivalent spin configurations are possible featuring two inward-pointing spins and two spins pointing out of each tetrahedra (as shown on the right side of Figure 1.2). The frustration in this tetrahedral config-

uration is analogous to the distribution of protons around oxygen atoms in frozen water, and as such has been termed 'spin ice', with the spins freezing into a set configuration below ~0.5 K.[12,17,21]

Transition metal oxides with triangular magnetic lattices can lead to new and interesting phenomena on account of their inherently frustrated geometry. A few materials known for magnetic frustration due to their triangular and corner-sharing motifs include kagomé lattices and pyrochlores (as shown in Figure 1.3 a & b), as well as other structure types including honeycomb lattices, spinels, garnets, and layered materials such as α-$NaMnO_2$ or $NaCoO_2$ (Figure 1.3 c).

Kagomé lattices have been investigated largely due to their observed magnetic frustration, but other interesting electronic behaviors have also been observed, including multiple magnetic phase transitions at low temperature for $Ni_3V_2O_8$ and $Co_3V_2O_8$.[22] The $KMn_3O_2(Ge_2O_7)$ kagomé structure exhibited weak ferromagnetism with concomitant insulating behavior.[23] Spin glass behavior was observed in $SrCr_{9p}Ga_{12-9p}O_{19}$, with a $\theta_{CW} \sim -500$ K,[2] but no observed spin ordering.[24–27] An absence of magnetic order was also observed in the $S = \frac{1}{2}$ kagomé lattice of herbertsmithite, $ZnCu_3(OH)_6Cl_2$ exhibiting strong magnetic frustration.[28–30]

Pyrochlores display properties ranging from electronic insulators ($La_2Zr_2O_7$), metallic conductors ($Bi_2Ru_2O_{7-y}$), ionic conductors and magnetocaloric materials ($Gd_{1.9}Ca_{0.1}Ti_2O_{6.9}$),[31] mixed ionic and electronic conductors, to spin ice systems ($Dy_2Ti_2O_7$), spin glass systems ($Y_2Mo_2O_7$), Haldane chain systems ($Tl_2Ru_2O_7$), and

[2] θ_{CW} is a convenient measure of the strength of magnetic interactions, discussed further in Section 2.4.

superconducting materials ($Cd_2Re_2O_7$).[12,32,33] A tunable response of the colossal magnetoresistance (CMR) was also observed in the $Tl_2Mn_2O_7$ pyrochlore upon substitution of Sc into the Tl atomic site, showing functional improvements for magnetic sensing applications compared to Mn-based perovskite materials.[34]

In two-dimensional (2D) (Delafossite) systems such as A_xMO_2, where A = alkali or alkaline earth and M = transition metal, the triangular lattice can exhibit a rich magnetic-structural phase diagram or exotic states such as spin liquids. No long range magnetic order was observed in $NaTiO_2$ down to 1.4 K, though a $\theta_{CW} \sim 1000$ K was observed. The $S = \frac{1}{2}$ nature of the Ti^{3+} suggests the possibility of exotic quantum behavior at low temperature where there is still no long range order.[24,35] 2D spin-half antiferromagnets have also generated considerable interest due to their observed superconductivity ($NaCoO_2$) and spin chirality.[12,36,37] The variation in physical properties in these materials is vast, but is closely related to their structures and the dimensionality of their correlated magnetic moments.

Less explored are materials in which a 2D triangular lattice is folded into three-dimensional (3D) space, leading to new topologies for studying magnetism. By rolling a triangular sheet (such as α-$NaMnO_2$) into a cylindrical tube, the 2D triangular lattice is transformed into a 3D tunnel, which at the same time constrains the system to a pseudo-1D topology (Figure 1.3 d). Such a folded triangular lattice can be realized in a group of metal oxides with the so-called hollandite structure type. This thesis focuses on compositional variations of hollandites and the resulting magnetic and electronic properties inherent to the structure and compositions of these materials.

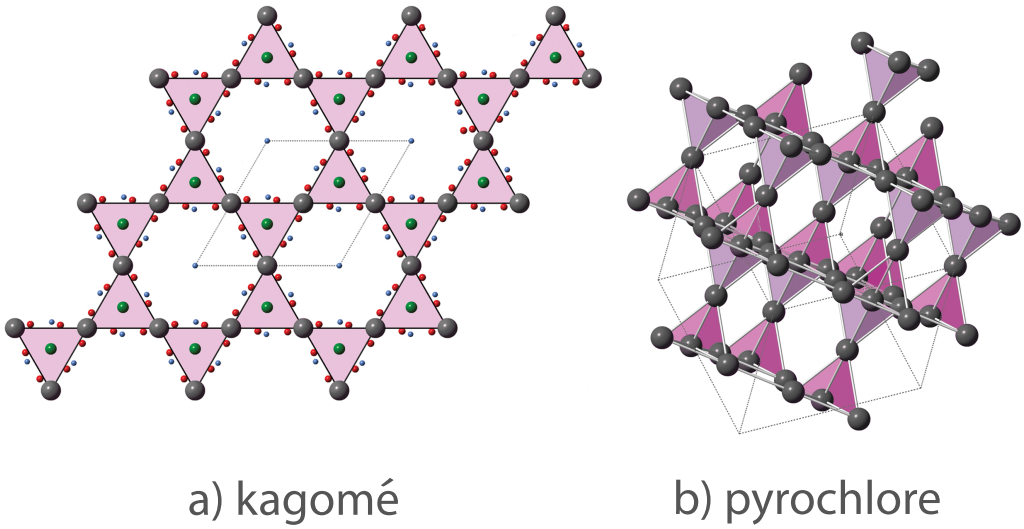

Figure 1.3: Magnetic frustration stemming from geometric constraints inherent in triangular lattices has been repeatedly observed in a) kagomé lattices (e.g. $YCa_3(MnO)_3(BO_3)_4$),[38] b) pyrochlores (e.g. $Tl_2Mn_2O_7$), c) layered (e.g. α-$NaMnO_2$) and d) tunnel structures (e.g. $Ba_{1.2}Mn_8O_{16}$). Some atoms have been omitted from each structure to provide more clarity in visualizing the triangular connectivity of the magnetic cations (in gray) in each framework.

No long range order is possible in one-dimension for $T > 0$, so one-dimensional (1D) magnets might be assumed to be tedious and uninteresting. In reality, the one-dimensionality allows the possibility of complex excitations which are still far from being completely understood. The study of systems with magnetic order limited to only one or two dimensions has been one of the most active areas recently in solid state physics and chemistry. Interesting magnetic phenomena occur as a result of the 1D, or even pseudo-1D nature of spin chains, spin ladders, and spinons. Novel Haldane spin-liquid ground states and spin-Peierls transitions have been observed in 1D spin-1 and spin-$\frac{1}{2}$ systems, respectively, such as the quasi-1D antiferromagnet $PbNi_2V_2O_8$.[39,40]

Though extensive studies have been conducted into the magnetic properties and the structure of nonporous perovskite and pyrochlore structures, little work has been done on porous oxide materials. The magnetic ordering in hollandite and todorokite materials has been reported, with both systems classified as spin glasses.[41] Many of these systems contain manganese in non-integral formal oxidation states, thereby offering interesting correlations between the structure and electronic interactions. These studies have increased in importance since the discovery of colossal magnetoresistance (CMR), in mixed-valent manganese perovskites and pyrochlores.

1.2 Hollandites

1.2.1 Crystal structure of hollandites

In 1906, Lewis Leigh Fermor provided the first description of what would come to be known as the mineral hollandite, honoring Mr. Thomas Henry Holland (then Director of the Geological Survey of India) as the mineral's namesake. The crystal structure of the hollandite mineral was not solved until 1945 by Byström and Byström, when it was decided to be isostructural to another known manganese-based mineral called cryptomelane.[42] Indeed, a series of minerals, including akaganeite, cryptomelane, coronadite, psilomelane, and others, feature the same crystallographic structure, with different names corresponding to different elemental compositions.[43–46] These materials have since been grouped together into the 'hollandite' family allowing a wide range of compositional flexibility.

With a nominal formula of $A_xM_8O_{16}$ (where $A \leq 2$), the hollandite structure can be described as MO_6 octahedra that share edges and corners to form a square tunnel, which is occupied by the A cations (Figure 1.4). Surrounded by eight oxygen atoms from metal-oxide framework, the A cation is often nonstoichiometric and orders Coulombically depending on its size and valency. This affects the oxidation state of the framework transition metal cations (M),resulting in mixed valency (usually a mix of 3+ and 4+ oxidation states). The tunnel walls are composed of edge-sharing MO_6 octahedra that connect the M centers in a triangular ladder, resulting in tunnel dimensions of $2 \times 2 \times \infty$ MO_6 octahedra.

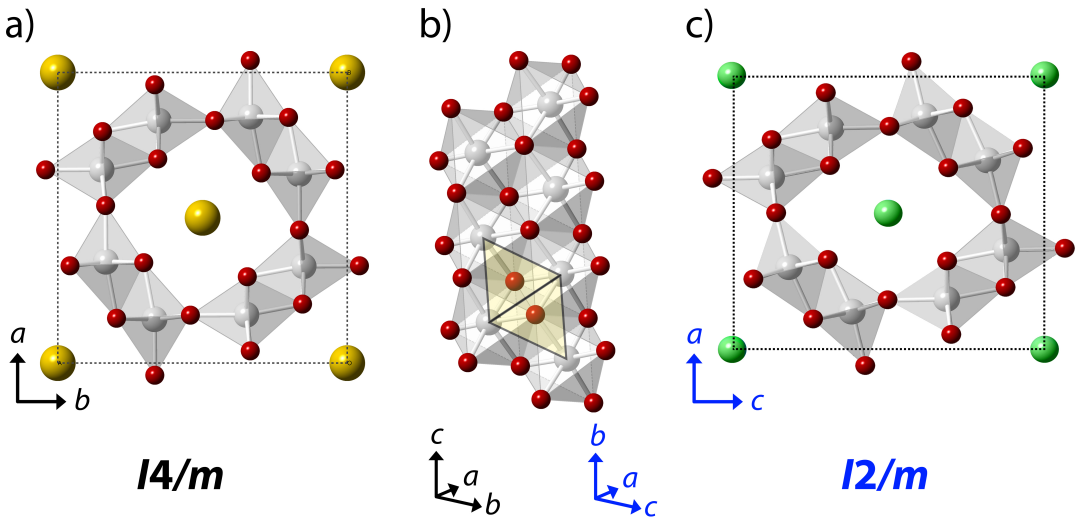

Figure 1.4: a) Tetragonal ($I4/m$) hollandite structure viewed down the tunnel direction, b) tunnel wall of hollandite showing the triangular ladder. c) Monoclinic ($I2/m$) hollandite structure viewed down the tunnel direction. For the nominal formula $A_xM_8O_{16}$, A is represented in yellow or green, M is gray, and O is red. Blue axes indicate the $I2/m$ crystallographic setting, black axes indicate $I4/m$.

In his original description of the mineral, Fermor wrote that "the crystals in their simplest form show what looks like a tetragonal prism surmounted by a flat tetragonal pyramid; but the few angular measurements yet made indicate that the mineral is either orthorhombic or triclinic, more probably the latter, and in either case very closely approaching the tetragonal form."[47] In the description of the unit cell, Byström claimed either a tetragonal or pseudotetragonal setting. The latter case was classified as monoclinic, with a β angle deviation from 90° of 0.5 - 1.5°, and a difference of 0.1-0.2 Å between the a and c unit cell parameters.[42] The debate on whether hollandite materials best fit the tetragonal (usually $I4/m$) or monoclinic ($I2/m$) setting depends on the composition of the material. Cheary et al observed a trend where hollandites featuring a large A cation, paired with a small M framework cation were usually tetragonal. Conversely, compositions featuring small A cations and large M cations were typically observed to fit the monoclinic setting. The rationale behind this trend was the supposition that the framework walls collapse in on the A cation, with the corner linkages of the MO_6 double chains acting as hinges, as shown in Figure 1.4. Proposing a correlation based on cation size, Cheary suggested a line of bifurcation at $r_M/r_A \sim 0.48$ as a predictive indicator for the hollandite symmetry, where r_M, r_A, and r_O are the ionic radii of M, A, and O, respectively.[48]

More recently, however, other researchers have rejected Cheary's indicator as overly simplistic. A second predictive measure for determining the symmetry of hollandites was proposed by Zhang and Burnham, claiming that if $r_A > \sqrt{2}(r_O + r_M) - r_O$, the structure could not be monoclinic, whereas if $r_A < \sqrt{2}(r_O + r_M) - r_O -$

0.15 the compound could not be tetragonal.[49] They also derived further equations for predicting the lengths of unit-cell edges,

$$a(\text{Å}) = 5.130(r_O + r_M) - 0.0291Z_M + 0.441\delta_A \tag{1.1}$$

$$c(\text{Å}) = \sqrt{2}(r_O + r_M) + 0.0366Z_M + 0.552\delta_M \tag{1.2}$$

where Z_M is the charge of the M cation, δ_A is the excess size of the tunnel cation A relative to the MO_6 framework, and δ_M is the excess size of the M cation relative to the octahedral cavity.

1.2.2 Potential applications for hollandites

Hollandites have several unique functionalities over other common microporous materials such as silicates and zeolites, including electrical conductivity, long-range magnetic ordering, and redox properties arising from partially filled d-states in the framework. To some extent, the d-orbital filling can be controlled through systematic incorporation of various transition metals into the frameworks and manipulation of their oxidation states. Thus, we can manipulate the electronic band structure of these microporous materials - a functionality lacking in mesoporous zeolites, for example.

The transition metal sites in hollandite structures can accommodate valencies from 2+ to 5+, and mixed valency is a common phenomenon in OMS materials. Just as mixed-valence manganates with the perovskite structure display interest-

ing and useful behavior such as colossal magnetoresistance (CMR),[34,50–52] mixed valences for M cations in hollandites could also lead to similar phenomena. Materials displaying CMR properties have aroused great interest due to their possible application in magnetic storage and sensing devices.[53] The tunability of the cations in the hollandite structure type makes these oxides highly functional for various applications such as molecular sieves, radiation waste storage, catalysts, and cathode materials in batteries.

The triangular M–M connectivity, coupled with mixed valency, can lead to interesting properties including insulating ferromagnetism,[54,55] frustrated magnetism,[56–58] and MITs.[59–61] Magnetic insulators are rare materials with potential applications in spintronics and multiferroics. The hollandites $A_xM_8O_{16}$, which contain mixed-valent transition metals, have demonstrated ferromagnetism combined with insulating behavior and provide a new platform for exploring the effects of magnetic frustration due to their 'folded' triangular lattice.

The most comprehensive studies on the physicochemical properties of these OMS-materials have been carried out on the Mn-based oxides.[5,6,41,62–65] Systematic studies to find other transition metals that may form these structures have been scattered and largely unconnected. There are, however, several other transition metals that can form the hollandite type structure including $K_xCr_8O_{16}$,[54,55,66,67] $K_xV_8O_{16}$,[68–70] $La_xMo_8O_{16}$,[71] $Ba_xRh_8O_{16}$,[72,73] and $A_xTi_8O_{16}$.[74–76] The physical properties of the Cr- and V-analogues show unique behavior, including metal-to-insulator transitions (MITs) and the unusual combination of semiconducting behavior coexisting with ferromagnetism.[54,55,59,60,77–80] Thus it is very likely that exploring hol-

landite materials containing not just mixed valence but also mixed metals will yield interesting properties. Indeed, doping and substitution at the M site in hollandites has already been undertaken by various researchers in efforts to tune the chemical properties.[48,70,74,75,79,81–95] Determining the location(s) of dopant atoms, as well as any potential charge ordering, is key to understanding new physics in the hollandites as well.

1.3 Objectives and outline of dissertation

In this dissertation, several different hollandite materials will be presented along with their accompanying magnetic and electronic properties. Developing magnetic models in complex structures is still very challenging. This dissertation focuses on a fundamental understanding of the interplay between structure and physical properties in hollandite materials.

In Chapter 2, fundamental theory and techniques are presented related to the following experimental results and analyses. The discussion focuses primarily on the basics of crystallography and magnetism, with some attention paid to transport and spectroscopic measurements.

In Chapter 3, the barium manganate hollandite, and its cobalt-substituted derivative are presented. The magnetic structure of $Ba_xMn_8O_{16}$ was tuned from a complex antiferromagnet with a Néel temperature (T_N) = 25 K to a ferrimagnet with Curie temperature (T_C) = 180 K via partial cobalt substitution for manganese. Both $Ba_xMn_8O_{16}$ and $Ba_xCo_yMn_{8-y}O_{16}$ were prepared by salt flux methods, and

combined neutron and X-ray diffraction confirm a monoclinic hollandite structure for both oxides. X-ray photoelectron spectroscopy reveals that the Co^{2+} substitution drives the average Mn oxidation state from 3.7+ to nearly 4.0+, thereby changing its d-electron count. Magnetization and resistivity measurements show that the cobalt-doped hollandite belongs to the rare class of ferrimagnetic insulators, with a high T_C of 180 K. Based on neutron diffraction measurements the first proposed solution of the magnetic structure of $Ba_xMn_8O_{16}$ is described, which consists of a complex antiferromagnet with a large magnetic unit cell. Upon substituting cobalt for manganese, the magnetic structure changes dramatically, destroying the previously large magnetic unit cell and promoting ferromagnetic alignment along the hollandite tunnel direction. The observed hysteresis at base temperature for $Ba_xCo_yMn_{8-y}O_{16}$ is explained as arising from uncompensated spins aligned along the (200) crystallographic planes.

Chapter 4 discusses the potassium manganate hollandite system, and the attempts made to determine the magnetic structure through several different neutron diffraction studies. Ambiguity in determining the symmetry ($I2/m$ vs $I4/m$) of the polycrystaline $K_{1.6}Mn_8O_{16}$ material complicates indexing the magnetic peaks.

Chapter 5 discusses a metal-insulator transition tuned by application of an external magnetic field that occurs in the quasi-one dimensional system $Bi_{1.7}V_8O_{16}$, which contains a mix of $S = 1$ and $S = \frac{1}{2}$ vanadium cations. Unlike all other known vanadates, the magnetic susceptibility of $Bi_{1.7}V_8O_{16}$ diverges in its insulating state, although no long-range magnetic ordering is observed from neutron diffraction measurements, possibly due to the frustrated geometry of the triangular

ladders. Magnetotransport measurements reveal that the transition temperature is suppressed upon application of an external magnetic field, from 62.5 K at zero field to 40 K at 8 T. This behavior is both hysteretic and anisotropic, suggesting t_{2g} orbital ordering of the V^{3+} and V^{4+} cations drives a first-order structural transition. Single crystal X-ray diffraction reveals a charge density wave of Bi^{3+} cations with a propagation vector of $0.846\mathbf{c}^*$, which runs parallel to the triangular chain direction. Neutron powder diffraction measurements show a first-order structural transition, characterized by the coexistence of two tetragonal phases near the metal-insulator transition. Finally, we discuss the likelihood that ferromagnetic V–V dimers coexist with a majority spin-singlet state below the transition in $Bi_{1.7}V_8O_{16}$.

In Chapter 6, preliminary studies into the mixed metal solid solutions of $Bi_{1.7}Cr_xV_{8-x}O_{16}$ and $K_{1.7}Mn_xTi_{8-x}O_{16}$ hollandite materials are discussed. Within the $Bi_{1.7}Cr_xV_{8-x}O_{16}$ set of materials, efforts are ongoing in driving the hollandite to a completely S=1 state, allowing investigation of the potential existence of Haldane behavior in the pseudo-1D hollandite structure. Understanding the effects of systematically changing the composition between two known end members of the hollandite family will allow for future tunability of the $K_{1.7}Mn_xTi_{8-x}O_{16}$ materials.

Chapter 7 provides the conclusion to this thesis, outlining future work to be done on materials with the hollandite structure type.

Chapter 2: Theory & Techniques

2.1 Overview

This chapter provides an overview of the experimental techniques and related theory utilized in characterizing the structure and properties of the materials reported within this thesis.

2.2 Synthesis techniques

Various synthetic techniques have been reported for synthesizing hollandite materials. Hydro- and solvothermal techniques, as well as redox chemistry resulting in precipitation of the desired product are synthetic methods often utilized in investigating the catalytic activity of hollandite materials.[3,41,64,89,96–101] The very small particles desired for catalytic studies have a high surface-to-area ratio, often resulting in low crystallinity of the materials, which is less than ideal for detailed structure-property analysis. Rather, in order to more fully investigate the relationships between the hollandite structure and the accompanying physical properties, highly crystalline materials are desired, and these wet synthetic techniques were for the most part disregarded.

High pressure techniques have been reported to produce single crystal samples of different hollandite materials.[54,66] Unfortunately, the small physical dimensions of the diamond anvil cells used in this technique limit both product yields and crystal sizes. Aside from the lack of access to equipment for high pressure syntheses, the desire to produce quantities of material suitable for neutron diffraction studies rendered this synthetic technique unhelpful for the studies herein.

The propensity of OMS materials to develop crystallographic defects, such as twinning and/or intergrowth of more than one OMS phase, make it difficult to grow crystals or prepare highly crystalline powders.[6] The fact that most inorganic systems are prepared by mixing dry ingredients and then firing at high temperature also makes it generically difficult to achieve very high purities. A range of crystal structures exist and each can often accommodate a range of magnetic ions, so the limits to this process are generally quite rigid. Further, not all chemical structures can be prepared with high purity and crystallinity, especially as single crystals, and particularly those obtainable only by high-pressure synthesis.

Because of the difficulty of preparing polycrystalline or single crystal hollandite materials under ambient conditions, little focus was given to making polycrystalline or single crystal samples of hollandites until 2001, when Kato et al and other researchers observed a metal-insulator transition in $Bi_xV_8O_{16}$.[102] Recently, Talanov et al and Moetakef et al have demonstrated high quality single crystal growth of hollandite oxides through flux methods.[75,103] Therefore, we have sought to prepare highly crystalline and phase-pure Mn-based hollandites by employing salt flux methods in order to fully explore the relationship between crystal struc-

ture and magnetic properties.

Solid state and salt flux techniques are thus the main focus of the synthetic work within this thesis.[74,85,104–106] Aside from producing polycrystalline or single crystal hollandites, these techniques have the added advantage of fairly facile scalability and working under ambient conditions.

2.2.1 Solid state reactions

Traditional solid state synthetic techniques are very straightforward. Powdered reactants are mixed together, then often pressed into pellets and heated in a furnace for a prolonged period of time. This synthetic method is intrinsically slow because of the inhomogeneity inherent at the atomic level. Nucleation of small crystals is able to occur at interfaces between different precursor grains, but in order for the[9]

2.2.2 Salt flux reactions

In contrast to crystal growth methods where the desired crystals have the same composition as the melt, precipitation methods involve the growth of crystals from a solvent of different composition. The solvent may be one of the constituents of the desired crystal, or the solvent may be an entirely separate liquid in which the crystals of interest are partially soluble. In these cases, the solvent melts are sometimes referred to as fluxes since they effectively reduce the melting point of the crystals by a considerable amount.[9]

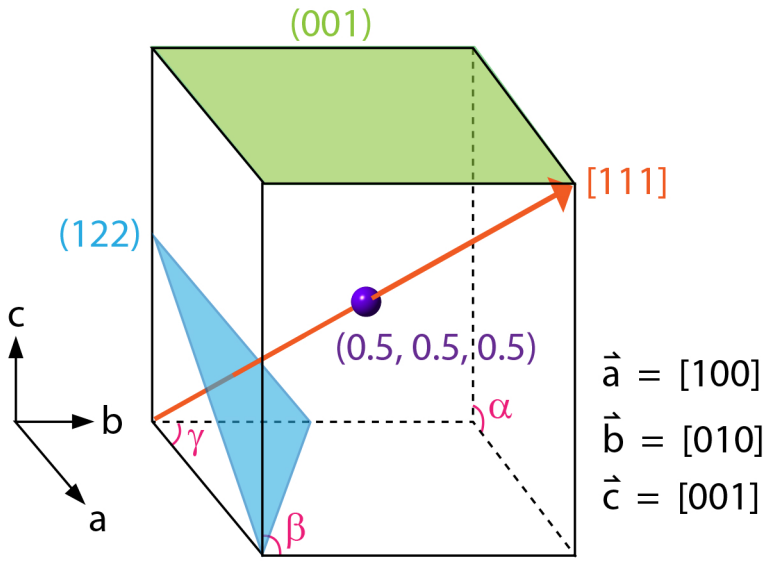

Figure 2.1: Representative unit cell depicting different features including lattice points (purple), directions (orange), and lattice planes (green and blue).

2.3 Crystallography & diffraction

A crystalline material is defined by the infinite repetition of a basic unit cell motif in three dimensions, where the unit cell is the smallest repeating unit that retains the full symmetry of the greater crystal structure. For a three-dimensional crystal, there are seven possible independent unit cell shapes, determined by the unit cell axes a, b, and c and angles α, β, and γ in real space (Figure 2.1).

Crystallographic techniques such as X-ray and neutron diffraction (discussed in subsequent sections) utilize reciprocal space in probing the structure of a crystalline material. The relationship between the physical crystal structure and its

reciprocal lattice (indicated by *) is given by

$$a^* = \frac{\vec{b} \times \vec{c}}{V_C}; b^* = \frac{\vec{c} \times \vec{a}}{V_C}; c^* = \frac{\vec{a} \times \vec{b}}{V_C} \tag{2.1}$$

where V_C is the volume of the unit cell, and hence;

$$V_C = \vec{a} \cdot (\vec{b} \times \vec{c}) \tag{2.2}$$

Within a crystalline material, a general point position is characterized by the coordinates u, v, w, or by the position vector $\vec{r}_{uvw}$:

$$\vec{r} = u\vec{a} + v\vec{b} + w\vec{c} \tag{2.3}$$

To indicate the direction along one of the unit cell edges, a, b, or c, the notations [100], [010], and [001] are used, respectively (Figure 2.1). Similarly, the notation [111] is used to indicate the direction of the cell diagonal.

Lattice planes extend in two dimensions throughout the crystal and are described by Miller indices, (hkl). This is achieved by taking the inverse of the point where the lattice plane intercepts the cell axes $\vec{a}/h; \vec{b}/k; \vec{c}/l$. For example, a plane that intersects the a axis one unit cell length away from the origin has an h value of 1. If the lattice plane intersects the b axis at its halfpoint, k = 1/2, and likewise for c with l, resulting in a Miller index of (122), as depicted in blue in Figure 2.1.[107]

The reciprocal lattice vector $d^* = ha^* + kb^* + cl^*$ is perpendicular to the direct lattice planes with Miller indices (hkl). The magnitude of d is the reciprocal of the

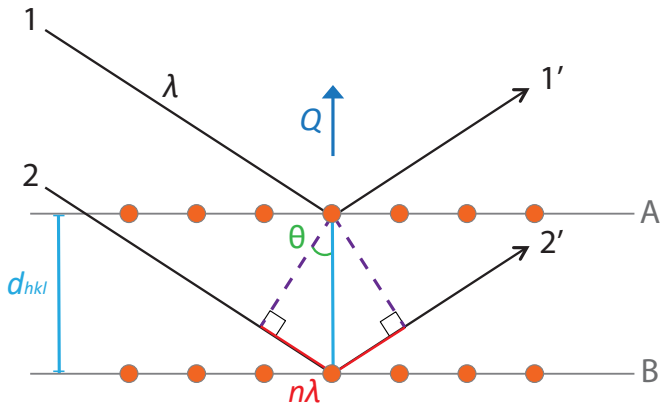

Figure 2.2: Bragg's formulation of diffraction by describing the phenomenon as reflections from uniformly spaced layers.

shortest distance between these (hkl) planes, as seen in Figure 2.2.

$$|d^*| = \frac{1}{d_{hkl}} \tag{2.4}$$

2.3.1 Diffraction theory

A useful representation of the diffraction process is given by picturing the atoms as arranged in a set of lattice planes (Figure 2.2). William H. and William L. Bragg regarded these planes as semi-transparent mirrors such that when a crystal is bombarded with some type of incident radiation, some of the beams are reflected by a plane, while the remainder are transmitted and later reflected by subsequent planes.

The spacing between parallel lattice planes, d, and the angle of incidence, θ,

is related to the distance traveled by Bragg's law,

$$n\lambda = 2d\sin\theta \tag{2.5}$$

where n is an integer, λ is the wavelength, d is the interlayer spacing, and θ is the angle of incidence.

If a crystal is comprised of uniformly spaced lattice planes A and B, for the reflected beams 1' and 2' to be in-phase, then the additional distance that beam 22' has to travel relative to 11' must be an integer multiple of the wavelength. Coherent scattering is only observed in the occurrence of constructive interference, where the path difference between scattered beams is an integer number of wavelengths. Out-of-phase reflections interfere destructively, resulting in cancellation or weakening of the reflected signal intensity.[108]

The position of diffracted radiation is determined by the distance between the Miller planes, and therefore, the lattice parameters of the crystal. The relative intensities of the Bragg reflections, I_{hkl}, are dependent mostly on the position of the atoms within the unit cell.

2.3.2 Diffraction techniques

Within a crystal, the scattering power for a reflection off the (hkl) lattice plane is defined by the structure factor, F_{hkl}, where I_{hkl} is the square of the amplitude of

the structure factor:

$$I_{hkl} = |F_{hkl}|^2 \tag{2.6}$$

For X-rays, the structure factor is written as

$$F_{hkl} = \sum_i f_i \exp[-2\pi i(hx_i + ky_i + lz_i)]\exp(-W_i) \tag{2.7}$$

and the structure factor for neutrons is

$$F_{hkl} = \sum_i b_i \exp[-2\pi i(hx_i + ky_i + lz_i)]\exp(-W_i) \tag{2.8}$$

where x_i, y_i, and z_i are the fractional coordinates of the ith atom, f_i is the scattering amplitude for X-rays, and b_i is the neutron scattering length. W_i is the Debye-Waller isotropic temperature factor taking into account the thermal vibration of the atoms.

$$W_i = \frac{8\pi^2 \sin^2\theta \langle u_i^2 \rangle}{\lambda^2} \tag{2.9}$$

where $\langle u_i^2 \rangle$ is the mean square displacement of the ith atom

Both X-ray and neutron diffraction techniques were heavily utilized in the studies herein.

The ability to scatter radiation varies by atom and type of radiation (Figure 2.3). For X-rays, the scattering amplitude (f_i) is proportional to the number of core electrons, and also depends on the radial distribution of electron density around the atomic nucleus. As a direct result, X-rays are not always reliable in determining

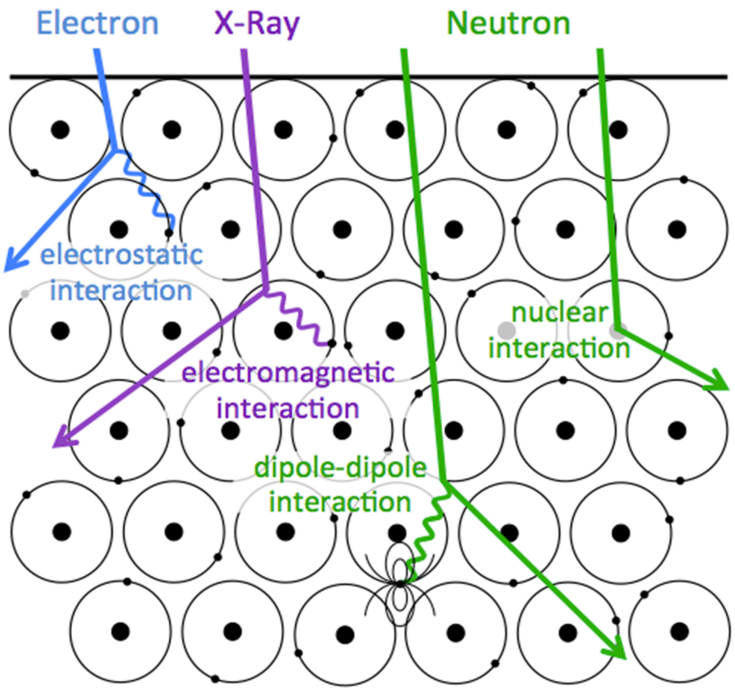

Figure 2.3: Schematic depicting the different scattering interactions of electrons, X-rays, and neutrons in matter. Electrons (blue) and X-rays (purple) interact with electron clouds via electrostatic and electromagnetic mechanisms, respectively. As a result of these interactions, neither medium is able to penetrate as deeply below the surface as neutrons (green), which interact with atomic nuclei. The nuclear interactions of neutrons are limited to very short ranges. Neutrons are also capable of dipole-dipole interactions with the magnetic moment of unpaired electrons in the material.

the location of light atoms within a structure, or for resolving parameters for two transition metals of close Z. The scattering factor for X-rays is also a function of the Bragg angle, with intensity dropping at higher values of 2θ.

With neutrons, coherent scattering (b_i) by nuclei occurs independently of the Bragg angle, resulting in higher peak intensities persisting at high values of 2θ. Unlike X-rays, the scattering strength of neutrons does not follow an intuitive trend, as depicted in Figure 2.4. The scattering length values result from variation in the nuclear properties (such as spin, energy levels, etc.) of any given nuclide. This is observed in the difference between the values for ^{1}H, ^{2}H, and ^{3}H, which are -3.7409 fm, 6.674 fm, and 4.792 fm, respectively.[109]

Neutrons are a spin-$\frac{1}{2}$ particle with a non-zero magnetic moment. Thus, in addition to interacting directly with the nucleus of an atom, neutrons are capable of dipole-dipole interactions with magnetic moments of unpaired electrons in the material, making neutrons an invaluable probe in determining the magnetic ordering in materials. Similar to the scattering factor for X-rays, however, the magnetic scattering factor is a function of the incident angle of radiation, resulting in magnetic Bragg peaks appearing at low values of 2θ.

The limitations of each type of scattering can largely be overcome by combining data collected by the different techniques, which will now be individually discussed in further detail.

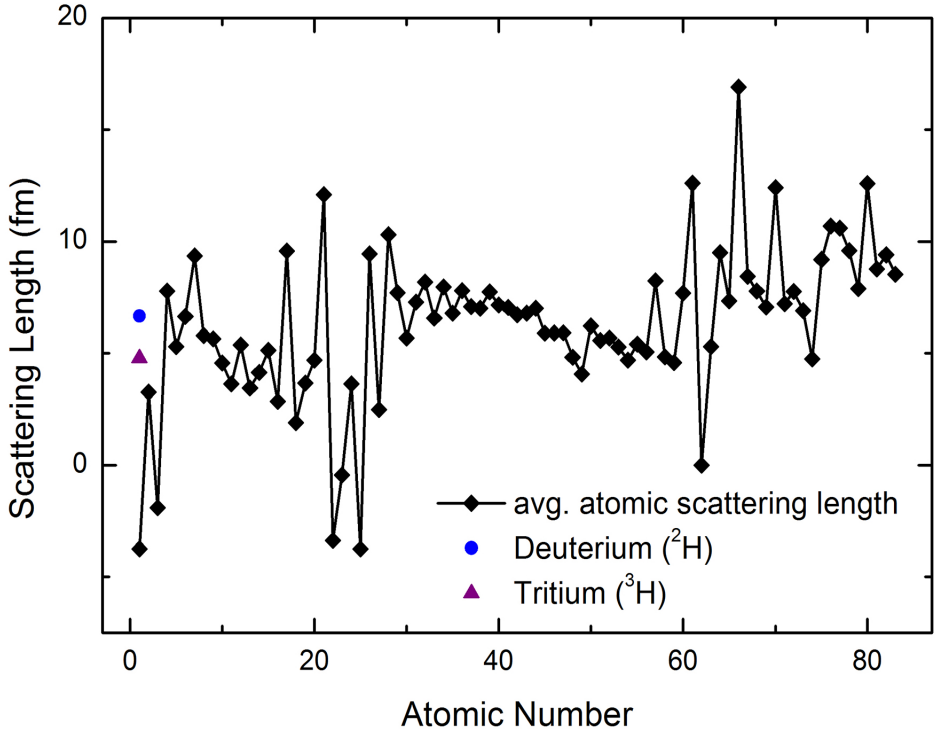

Figure 2.4: Neutron scattering lengths for elements Hydrogen through Francium. Different isotopes of the same element can have significantly different scattering lengths, as indicated by the values provided for hydrogen, deuterium and tritium.[109]

2.3.2.1 Powder X-ray diffraction

Laboratory X-ray diffractometers are composed of three primary components: a radiation source, a monochromator, and a radiation detector. A typical X-ray setup consists of a metal target, typically copper, in a tube under high vacuum. A filament (such as tungsten) is heated at one end of the tube, emitting a beam of electrons, which are accelerated towards the copper target. When the electrons collide with the copper, core K-shell electrons are emitted, causing electrons from higher filled shells to drop into the now vacant $1s$ orbitals.

The transitions from the outer L and M shells to the K ($1s$) shell (that is L→K and M→K) are designated as Kα and Kβ, respectively, resulting in the emission of electromagnetic radiation with a characteristic wavelength unique to every element.[2] The relaxation of electrons into the $1s$ orbital vacancies is governed by the transition selection rule, which requires a change in orbital angular momentum of one ($\Delta l = \pm 1$), thus dictating that the relaxing electron must come from the L ($2p$) or M ($3p$) orbitals, resulting in two intense lines in the emission spectrum. The emitted X-rays can then be passed through the monochromator, which diffracts the beams to produce radiation at a single wavelength.

Powder X-ray diffraction (PXRD) is beneficial for samples where it is difficult to obtain single crystals. An ideal sample for PXRD measurements is well-ground and prepared in such a way that the sample particles are randomly distributed over

[2]This phenomenon is exploited in the fundamentals of X-ray Photoelectron Spectroscopy, discussed and illustrated in Section 2.6.

every possible orientation. Successful powder diffraction measurements thereby give information for every possible reflection in a structure, producing a diffraction pattern where diffracted Bragg peaks from three dimensions are superimposed onto a 1D axis.

Powder X-ray data for the materials discussed in this thesis were collected using a Bruker D8 Advance X-ray diffractometer with a copper source, located at the X-ray Crystallography Center at the University of Maryland. Samples were finely ground and laid on a plastic disk, with efforts taken to minimize the effects of preferred orientation. Materials were typically studied from 8 to 90° two-theta, in steps of 0.04° at 1 second per step to verify phase purity. Collected data were then refined in most cases using the Rietveld method. Successful use of the Rietveld method is directly related to the quality of powder diffraction data, with better quality data increasing the likelihood of a reasonable, reliable structure. Thus, for the samples discussed herein, longer scans were utilized, measuring from 8 to 140° 2θ, in steps of 0.013° at 0.85 second per step.

2.3.2.2 Powder neutron diffraction

Neutrons are useful as a probe for investigating magnetism in condensed matter, providing experimental means to observe both light atoms, as well as the arrangements of magnetic moments in a material.

There are two types of facilities that produce neutrons at the appropriate energies to be used in neutron diffraction studies. The first method of neutron produc-

tion involves a fission reaction at a nuclear reactor. Uranium with enriched levels of ^{235}U is a very common fuel at these reactors, and through fission of the radioactive fuel, very high energy neutrons are produced in a flux of up to 10^{15} s^{-1} cm^{-2}.[109] It is then necessary for the neutrons to be slowed down via a moderating material such as heavy water (D_2O) to obtain an approximate energy. These neutrons are then guided through a collimator to produce a coherent beam, to a large single crystal monochromator, which directs radiation of a specific wavelength towards the sample in what is termed Constant Wavelength (CW) diffraction. The monochromation process results in the loss of a significant percentage of the original neutron flux produced, but allows for the angular deflections of the neutrons to be interpreted using the relations described in Bragg's law. Interaction of the incident neutrons with the sample then scatters the radiation, which is then measured by the detector.

A majority of the powder neutron diffraction data in this thesis was collected using the BT-1 high-resolution powder neutron diffractometer at the National Institute of Standards and Technology (NIST) Center for Neutron Research (NCNR) (Figure 2.5) in Gaithersburg, Maryland. The reactor at NCNR produces a thermal flux of 4×10^4 neutrons/cm^2·s using uranium as the reactor fuel. Three different collimators for the incident radiation allow the instrument response to be tailored to the experiment, and three different monochromators are available for BT-1 measurements, namely Ge(311), Cu(311), and Ge(733). Details for each monochromator are provided in Table 2.1. A rotating bank of 32 ^3He detectors at 5° intervals allows diffraction data to be collected over a 2θ range of 0 - 167°.[110]

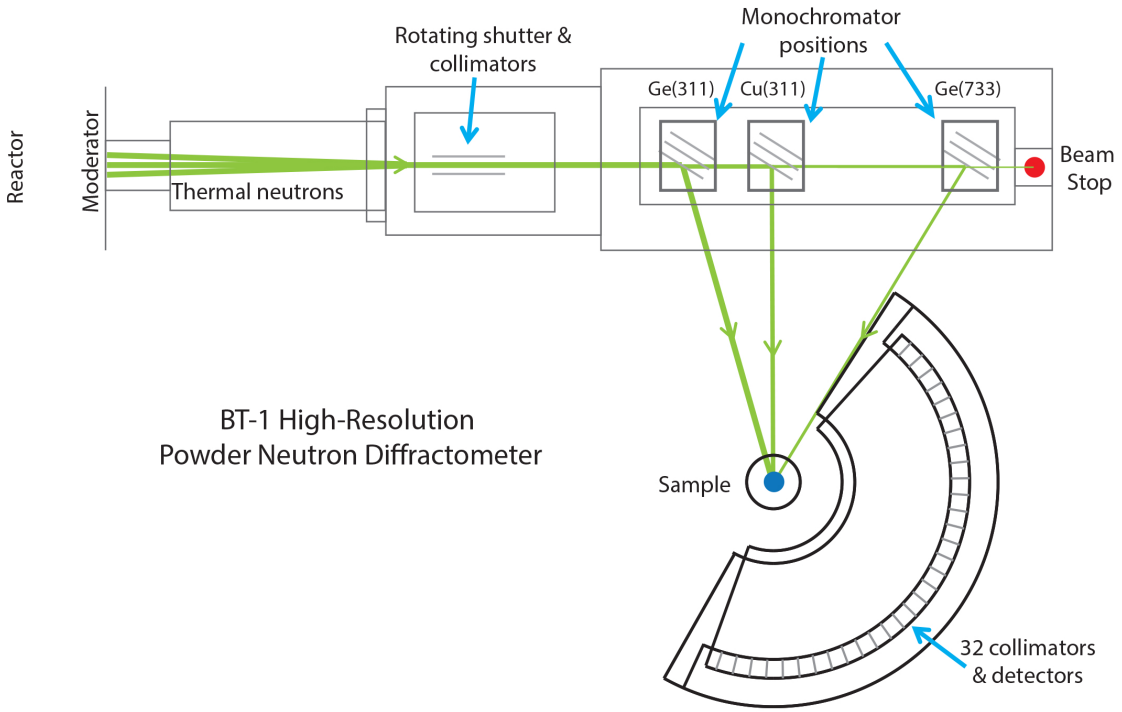

Figure 2.5: Schematic diagram of the BT-1 high-resolution powder neutron diffractometer operating at constant wavelength (CW). Adapted from Ref.[110] Notable features common to all CW neutron diffractometers include collimators to align the beam, monochromators to select for a particular wavelength, and detectors to measure the scattering after neutrons interact with the sample.

Table 2.1: Monochromator details for the BT-1 constant wavelength neutron powder diffractometer at NCNR.[111]

Monochromator	In-pile Collimation (arcmin)	Monochromator 2θ (°)	Relative Bragg Intensities	Flux ($n/(cm^2 \cdot s$)	λ (Å)	Relative Number of Reflections
Ge(311)	60’	75	5.78	1,160,000	2.079	50
	15’	75	2.86	570,000	2.079	50
	7’	75	1.44	290,000	2.079	50
Cu(311)	60’	90	1.84	870,000	1.540	100
	15’	90	1.00	440,000	1.540	100
	7’	90	0.54	230,000	1.540	100
Ge(733)	60’	90	0.31	330,000	1.197	200
	15’	90	0.20	200,000	1.197	200
	7’	90	0.11	120,000	1.197	200

Instead of using neutrons produced by a nuclear reactor, nuclear spallation provides a second technique for producing neutrons. This method requires a heavy metal source (such as mercury or tungsten) that gets bombarded by protons that have been accelerated to high energies (up to 1000 MeV), thus also requiring an accelerator such as those found at synchrotron facilities. Upon the proton's collision with the heavy metal, a burst of neutrons and other small particles is ejected from the source in all directions and at all frequencies, with a flux of ~20-30 neutrons for every proton that bombards the target.[112]

After the original pulse produces a white beam of neutrons, the spalled neutrons pass through a moderator, interact with the sample, and finally reach a detector, fixed at scattering angle $2\theta_0$. The total time from the initial pulse until the final detection event is carefully measured and is then used to calculate the scattered intensity as a function of neutron wavelength.

The relation between the wavelength of the neutron and the total time-of-flight (t) can be calculated by connecting the de Broglie equation to Bragg's law:

$$\lambda = \frac{ht}{m_n L} = 2d_{hkl}\sin\theta_0 \tag{2.10}$$

where m_n is the neutron mass, h is Planck's constant, $L = L_1 + L_2$ is the total flight path (L_1 is the distance the neutrons travel from the moderator to the sample, and L_2 the distance between the sample and detector), and $2\sin\theta_0$ is the fixed scattering angle. The spectral distribution of the incident beam is modeled by measuring isotropic scattering from a vanadium standard, accounting also for

necessary corrections in detector efficiency as a function of wavelength variation.

The technique utilizing Eq. 2.10 from a spallation source is known as time-of-flight (TOF) analysis, and allows for greater neutron flux at the sample as there is no monochromation required. Compared to the incident beams used in x-ray diffraction, however, even TOF neutron sources are considered to have low flux; thus all neutron diffraction studies require significantly more sample for analysis.

Two samples in this thesis were measured using TOF neutron diffraction, collected on the High Intensity Powder Diffractometer (HIPD) beamline at Los Alamos National Lab (LANL) Lujan Neutron Scattering Center (LNSC). HIPD has detector banks at 14, 40, 90, and 153 degrees, and can access a Q range from 0.2 to 50 $Å^{-1}$.

2.3.2.3 Single crystal diffraction

Having a single crystal for X-ray diffraction studies can significantly simplify the structural determination of a material, particularly if it is a novel structure.

Prior to 1970 almost all single crystal diffraction studies used film. The crystal was mounted in the center of the X-ray beam, causing the incident radiation to diffract, exposing the film. An alternative method of data collection allowed for the crystal to be rotated, diffracting X-rays from each of the atomic planes, onto a strip of film encircling the crystal. Modern electronic detectors featuring either X-ray counters or optical detection by CCD have improved the accuracy of X-ray intensity and count rates.

Scattering from a crystal is confined to distinct points in reciprocal space. The

intensity in each point is modulated by the absolute square of the unit cell structure factor. With a sufficiently large set of diffracted intensities from a given crystal it is possible to deduce the positions of the atoms in the unit cell.

The single crystal instrumentation used herein is a Bruker Apex2 diffractometer equipped with a molybdenum source and a CCD area detector, with a graphite monochromator. Single crystal X-ray data was measured by rotating crystals mounted in the incident radiation.

2.3.3 Powder diffraction data analysis

When an incident beam is diffracted off of randomly oriented crystallites in a powder sample, the observed diffraction pattern is a superposition of scattering that occurs in the three-dimensional crystallographic lattice onto a one-dimensional representation. Miller planes that have similar d-spacing, regardless of their orientation along the different crystallographic axes, subsequently diffract to similar 2θ angles. Oftentimes, these peaks overlap, making accurate measurement of the observed intensities difficult. Developing the computational tools to analyze all the Bragg peaks in a diffraction pattern simultaneously was a major breakthrough in powder analysis. These tools are described in the subsequent sections.

2.3.3.1 Indexing peaks

In order to solve a structure from powder data it is necessary to extract as many (hkl) reflectionsand intensity values as possible from the data set. Peak

locations tell the size of the crystallographic unit cell, whereas peak intensities relate to the contents of the unit cell. Atomic identities, partial or full occupancies, and thermal displacements affect the intensities, and microcrystalline properties affect the peak shapes.

Initially, peak positions are found in the data. Next, the pattern is indexed in order to determine the unit cell or lattice parameters. Then, space group determination follows based on symmetry and the presence or absence of certain reflections. Either Le Bail or Pawley techniques may be used to extract intensities and refine the unit cell.

Until the 1980s, accurate extraction of peak intensities was not feasible due to the overlapping nature of peaks in a powder diffraction profile. However, with the development of high-speed computers with large memories and high-resolution diffractometers, pattern decomposition became a viable and important part of the analyses of powder data.

In the Pawley technique, every reflection is assumed to have a peak position determined by the unit cell parameters and the 2θ zero error, with peak width determined by the resolution function parameters U, V, W, and a peak intensity I_{hkl}.

Pawley reduced the correlations by introducing both constraints and restraints into the least-squares procedure. As the difference between the calculated 2θ values of two adjacent peaks approaches zero, their intensities are constrained to be equivalent. When the $\Delta 2\theta$ is less than the step size, this is introduced as a hard constraint, and when larger, it is used as a soft restraint. Negative intensities may

occasionally be obtained.

The Pawley technique treats peaks individually, while the Le Bail technique is a method of whole pattern fitting. Le Bail fits can suggest a potential crystallographic setting, based off of the combination of peak locations.

When either the Le Bail or Pawley technique is employed to perform a full pattern decomposition, one must be careful to use suitably determined relevant parameters (background, peak shape, zero shift, or sample displacement, and unit cell dimensions) as the initial approximation.

The Le Bail method extracts intensities (I_{hkl}) from powder diffraction data. This is done in order to find intensities that are suitable to determine the atomic structure of a crystalline material and to refine the unit cell. For the Le Bail method, the unit cell and the approximate space group of the sample must be predetermined because they are included as a part of the fitting technique. The algorithm involves refining the unit cell, the profile parameters, and the peak intensities to match the measured powder diffraction pattern. It is not necessary to know the structure factor and associated structural parameters, since they are not considered in this type of analysis. Le Bail can be used to find phase transitions in high pressure and temperature experiments, and it generally provides a quick method to refine the unit cell, which allows better experimental planning.

Le Bail analysis fits parameters using a least squares analysis, which is an iterative process. First, the Le Bail method defines an arbitrary starting value for the intensities (I_{obs}). This value is ordinarily set to one, but other values may be used. While peak positions are constrained by the unit cell parameters, intensities are

unconstrained. The somewhat arbitrary choice of starting values produces a bias in the calculated values. The refinement process continues by setting the new calculated structure to the observed structure factor value. The process is then repeated with the new estimated structure factor. At this point, the unit cell, background, peak widths, peak shape, and resolution function are refined, and the parameters are improved. The structure factor is then reset to the new structure factor value, and the process begins again.[107]

The Le Bail technique is much better suited for dealing with overlapping intensities than using the Pawley technique, since the intensity is allotted based on the multiplicity of the intensities that contribute to a particular peak.

2.3.3.2 Rietveld refinement

In 1969, Hugo Rietveld proposed a refinement method to overcome the problem of peak overlap in powder diffraction data.[113] To a certain extent, the Rietveld method (known also as full pattern refinement) is similar to the full pattern decomposition using Pawley and/or Le Bail algorithms, except that values of integrated intensities are no longer treated as free least squares variables (Pawley), or determined iteratively after each refinement cycle (Le Bail). They are included into all calculations as functions of relevant geometrical, specimen, and structural parameters.

Rietveld's approach essentially compares a calculated diffraction model against the observed experimental data. The experimental powder diffraction data are uti-

lized without extracting individual integrated intensities or individual structure factors, and all structural and instrumental parameters are systematically refined as the calculated profile is fit to the observed data. This is accomplished by using a linear least squares minimization of the function, S_y,

$$S_i = \sum_i w_i (y_i - y_{ci})^2 \tag{2.11}$$

where y_i is the observed intensity for the ith point and y_{ci} is the calculated intensity at the ith point, and w_i is the weighting of the observables and is defined by

$$w_i = \frac{1}{y_i} \tag{2.12}$$

Since observed intensity is not associated directly with a Bragg reflection, for an accurate profile to be obtained, a reasonable starting model is required. The calculated intensity is dependent on the structure factor $|F_{hkl}|^2$ values taken from the model, which are calculated by

$$y_i = s \sum_{hkl} m_{hkl} L_{hkl} \left|F_{hkl}\right|^2 A_i G(2\theta_i - 2\theta_{hkl}) P_{hkl} T + y_i b \tag{2.13}$$

where s is the scale factor, m_{hkl} is the multiplicity factor, L_{hkl} is the Lorentz-polarization factor for the reflection (hkl), A_i is the symmetry parameter, $G(\theta)$ is the peak shape function, $2\theta_{hkl}$ is the calculated position of the Bragg peak, corrected for the zero point shift, P_{hkl} is the preferred orientation function, T is the absorption correction, and y_{ib} is the background intensity at the ith step.

The agreement between the observed and calculated structures is measured by the goodness of fit factors, defined as R_{wp}, for 'weighted profile', R_p, for 'profile R-factor', and R_{exp} for 'expected' goodness of fit, each defined as follows:

$$R_{wp} = \sqrt{\frac{\sum_i w_i (y_i - y_{ci})^2}{\sum_i w_i y_i^2}} \tag{2.14}$$

This compares how well the structural model under refinement accounts for relatively small and large Bragg peaks across the diffraction profile. The weighting factor is given by w_i.

$$R_p = \frac{\sum_i \left| y_i - y_{ci} \right|}{\sum_i y_i} \tag{2.15}$$

and

$$R_{exp} = \sqrt{\frac{(N - P + C)}{\sum_i w_i y_i^2}} \tag{2.16}$$

which accounts for the statistical quality of the data and the number of variables used in the refinements, where N is the number of profile points, P is the number of refined parameters, and C is the number of constraints used.

During the course of a structural refinement, the goodness of fit factor, χ^2, can be used to compare the quality of the data.

$$\chi^2 = \left(\frac{R_{wp}}{R_{exp}} \right)^2 \tag{2.17}$$

When the structural model, which makes both physical and chemical sense yields integrated intensities with similar peak and background features to the ob-

served data, the fully refined crystal structure of a material should result in a calculated powder diffraction pattern closely resembling collected data. In other words, the difference between the measured and calculated powder diffraction profiles should be close to zero, and a value close to one observed for χ^2.

The Rietveld technique provides a wealth of noncrystallographic structural information including reliable phase composition, amorphous content, grain size, microstrain information, texture analysis, and more. When a material is only available in a fine-grained, powdered, untextured thin film or other states, Rietveld refinement is by far the most robust approach for analyzing the structure. Further, powder diffraction provides a more accurate view of the sample bulk, whereas single crystals may have slight variations between different specimens.

Various software programs are available, such as GSAS, FullProf,[114] or Topas,[115] for utilizing the Rietveld refinement technique to analyze diffraction data obtained from facilities around the world. The majority of refinements carried out within this thesis were performed using the Topas software suite unless otherwise indicated.

2.4 Magnetism

Because electrons are present in all matter, everything possesses some type of magnetism. Diamagnetism occurs when electrons are paired, such as the electrons filling the core levels of an atom, making diamagnetism an underlying property of all matter. Magnetism becomes much more interesting, however, when considering unpaired electrons occupying partially filled d or f orbitals.

The magnetic properties of unpaired electrons are regarded as arising from two causes, electron spin and electron orbital motion. These interact to define the magnetic moment of an ion by

$$\mu_{(S+L)} = \sqrt{4S(S+1) + L(L+1)} \tag{2.18}$$

where L is the orbital angular momentum quantum number for the ion and S is the sum of the spin quantum numbers of the individual unpaired electrons. For first row transition metal ions, due to the smaller size of the d-orbitals, it is more common to calculate effective magnetic moments by using the spin-only formula,

$$\mu_s = g\sqrt{S(S+1)} \tag{2.19}$$

where g is the gyromagnetic ratio, and usually has a value of approximately 2.00. Such a spin-only formula indicates that all orbital contributions to the moment have been quenched.

Magnetic susceptibility (χ) is a dimensionless measure of the magnetic response (Magnetization, M) of a material upon application of an external magnetic field (H).

$$\chi = \frac{M}{H} \tag{2.20}$$

The relationship between the magnetic moment, μ, of a material and its mag-

netic susceptibility, χ, is given by

$$\chi = \frac{N\mu_B^2\mu^2}{3k_BT} \tag{2.21}$$

where N is Avogadro's number, μ_B is the Bohr magneton, and k_B is Boltzmann's constant.

The pairing of electrons in a diamagnet results in very low change in the magnetic susceptibility of that material, as there are no unpaired electrons to interact with an external magnetic field. Thus, the susceptibility of a diamagnet is very small and slightly negative, due to the decrease in flux density experienced under an applied field.

Paramagnetism occurs when there are unpaired electrons in a system, but the spins on those electrons are randomly oriented and do not interact with each other in an ordered manner. In a paramagnetic material, the magnetic susceptibility diverges at low temperatures according to the Curie law, which states that magnetic susceptibility is inversely proportional to temperature, T.

$$\chi = \frac{C}{T} \tag{2.22}$$

where C is the Curie constant, and is specific to the material being measured. Truly paramagnetic materials that obey the Curie law yield a positive slope with an intercept of 0 K when $1/\chi$ is plotted against temperature.

As thermal energy is removed from the system, or as magnetic field is applied, spins in a paramagnetic state may couple together, with varying magnetic

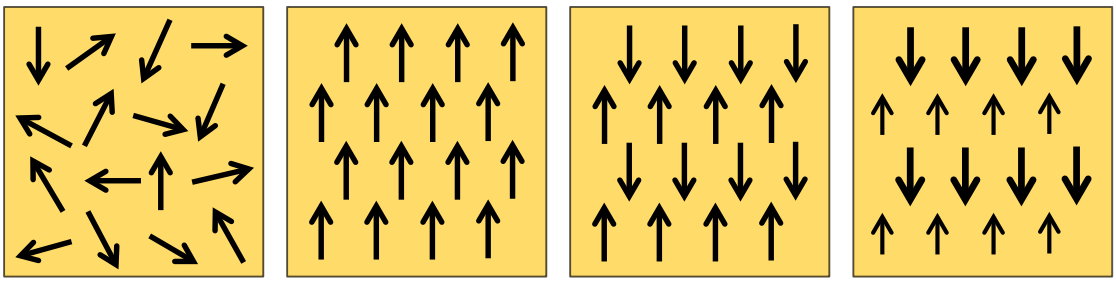

a) Paramagnetic (PM) b) Ferromagnetic (FM) c) Antiferromagnetic (AFM) d) Ferrimagnetic (fM)

Figure 2.6: a) Paramagnetic ordering (PM), where spins are oriented randomly with no net magnetization in absence of an external field. b) Ferromagnetic ordering (FM), with spins aligned parallel to produce net magnetization. c) Spins aligned anti-parallel, yielding no net magnetization for antiferromagnetic ordering (AFM). d) Spins aligned anti-parallel, but with moments of different magnitudes which fail to completely cancel each other out, producing net magnetization for ferrimagnetic (fM) ordering.

behaviors occurring in response to this cooperative interaction. The different types of magnetic order are summarized below.

A system displays a ferromagnetic response when the unpaired electrons are correlated in such a way that all of the spins are oriented in the same direction (all spin up or all spin down), giving a net magnetic moment in one direction. This ordering occurs at and below the Curie temperature, T_C. Unlike diamagnets and paramagnets, the addition of an external field to a ferromagnetic material can cause a strong coupling interaction as the moments align. This long range magnetic order can persist even after the field is removed, resulting in magnetic hysteresis, as shown in Fig. 2.7.

Upon application of the external field, the magnetization increases from the

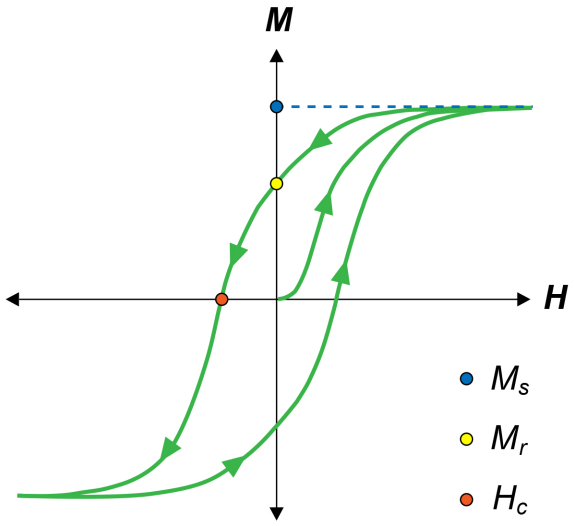

Figure 2.7: Hysteresis loop for a typical ferromagnet. M_s is the saturation magnetization, or the maximum value of observed magnetization. M_r is the remnant magnetization, or the amount of magnetization remaining when the applied field is returned to zero. H_c is the coercive field (the applied reverse field necessary to bring the magnetization back to zero).

origin until reaching the saturated value M_s. At this point, all available spins have aligned to the direction of the magnetic field and the value of M_s will not increase further, even with application of higher field. Once saturation has been achieved, decreasing the applied field back to zero does not eliminate the magnetization in a ferromagnetic material, leaving some remnant or residual magnetization (M_r). The reversed field required to reduce the magnetization to a value of zero is called the coercive field, H_c. Further reversal of the field achieves magnetic saturation in the reverse direction, resulting in a hysteresis loop featuring an inversion symmetry about the origin.

Antiferromagnetism occurs when the spins are antialigned in a 1:1 ratio, such that for every spin up electron there is a spin down and net magnetization is zero. The onset of antiferromagnetic ordering corresponds to a decrease in magnetization below the ordering temperature, called the Néel temperature, T_N.

If the magnitude of the spins, either spin up or spin down, are not completely counterbalanced by the antialigned moments, the ordering is called ferrimagnetic and a net magnetic response is observed.

Magnetic ordering causes the susceptibility to deviate from the Curie law, in ways often unique to the specific material. When a material displays magnetic order below a critical temperature, the Curie-Weiss law then applies to the system, where

$$\chi = \frac{C}{(T + \theta_{CW})} \tag{2.23}$$

In the Curie-Weiss law, θ_{CW} is the Weiss constant, corresponding to the temperature where the straight line (extrapolated from the high T paramagnetic regime in the observed data) intercepts the x-axis when $1/\chi$ is plotted against temperature. A negative Weiss constant indicates an antiferromagnetic interaction, whereas a positive Weiss constant is indicative of ferromagnetic coupling. The magnitude of the Weiss constant is indicative of the strength of the interaction.

Essentially, θ_{CW} is the sum of the exchange interactions in a magnetic system, thereby setting the energy scale for the magnetic interactions. In a system with little or no frustration, strong deviations from the Curie-Weiss law are expected for $T \sim |\theta_{CW}|$, with an onset of long range magnetic order occurring near $|\theta|$. For ordered ferromagnets this is nearly realized, as $|\theta_{CW}|/T_C \sim 1$. In antiferromagnetic systems the situation is more complex, depending on the exact magnetic structure which is adopted. Typical values for non-frustrated AFM lattices show $|\theta_{CW}|/T_N$ values in the range of 2 to 4 or 5, and the somewhat arbitrary condition, $|\theta_{CW}|/T_N > 10$, has been proposed as the threshold for notable frustration.[12,24]

2.4.1 Mechanisms for magnetic exchange

A first approximation of the Hamiltonian for nearest neighbor metal-metal magnetic exchange is

$$\mathscr{H} = -2\sum J_{ij}\mathbf{S_i}\cdot\mathbf{S_j} \tag{2.24}$$

where the sum is taken over all pair-wise interactions of spins i and j in a

lattice.

Direct exchange occurs when electrons on neighboring atoms interact without an intermediary. This requires sufficient orbital overlap. The direct exchange interaction (J_{ij}) coupling the spins, $\mathbf{S}_i$, of localized electrons in insulators can be described by the model Heisenberg Hamiltonian

$$H_{ex} = -\sum_{ij} J_{ij} \mathbf{S}_i \cdot \mathbf{S}_j \tag{2.25}$$

If the two states of interest are electronic states in a free atom, then the exchange integral, J_{ij} that couples them is positive and the spins align parallel, as reflected in Hund's rules. If the interaction takes place between electrons localized on different neighboring atoms, J_{ij} tends to be negative; this corresponds to the situation in which two electrons align antiparallel to form a covalent bonding state. The direct-exchange interaction falls off rapidly with distance, so that the interaction between further neighbors is effectively zero.

There are several different mechanisms possible for indirect exchange.

Superexchange, first described in the $La_{1-x}Ca_xMnO_3$ oxides with the perovskite structure, is the mechanism that describes the interaction of magnetic moments through a nonmagnetic intermediate, such as an O^{2-} anion. The rules were first formulated by John B. Goodenough and Junjiro Kanamori, and are subsequently known as the Goodenough-Kanamori rules.[116–118] Superexchange can be described by a Heisenberg Hamiltonian, in which the sign of J_{ij} is determined by the metal-oxygen-metal (M-O-M) bond angle and the d electron configuration on the transi-

tion metal. This interaction is an important source of metal-metal interactions or magnetic exchange in insulating compounds of the transition metal ions.

When d-orbitals of two transition metal cations are oriented towards each other, overlapping with opposing lobes of an intermediate p-orbital of an O^{2-} ion, the superexchange mechanism leads to antiferromagnetic coupling between pairs of filled ($M1_f$ and $M2_f$) or empty ($M1_e$ and $M2_e$) d-orbitals, as shown in Figure 2.8. This occurs in accordance with the Pauli exclusion principle, which states that for two electrons to occupy the same orbital, their spins must be paired and in opposite orientations. The entire M1-O-M2 configuration is arranged linearly, and this is known as 180° exchange. When the oxygen anion is mediating between one filled ($M1_f$) and one empty ($M2_e$) transition metal d-orbital, the resulting interaction is ferromagnetic. $M1_f$ accepts the electron from the oxygen with spin opposing the electrons already occupying the $M1_f$ d-orbital. The empty d-orbital of M2 then accepts the other oxygen electron, which has the same spin type as the other d-electrons forming its magnetic moment in accordance with Hund's rule. The strength of the interaction will depend on the amount of overlap.

Ferromagnetic ordering comes about by a 90° exchange path. Similar to the 180° exchange mechanism, the transfer occurs between d-orbitals of the transition metal and the p-orbitals of the oxygen, resulting in the overlap of two different p-orbitals, p_x and p_y, with the corresponding d-orbitals of the two transition metal sites. This results in two electrons or p-holes present on the oxygen in the excited intermediate state. Depending on the two transition metal ions, the remaining p-electrons will either have spins which are parallel or antiparallel since Hund's rules

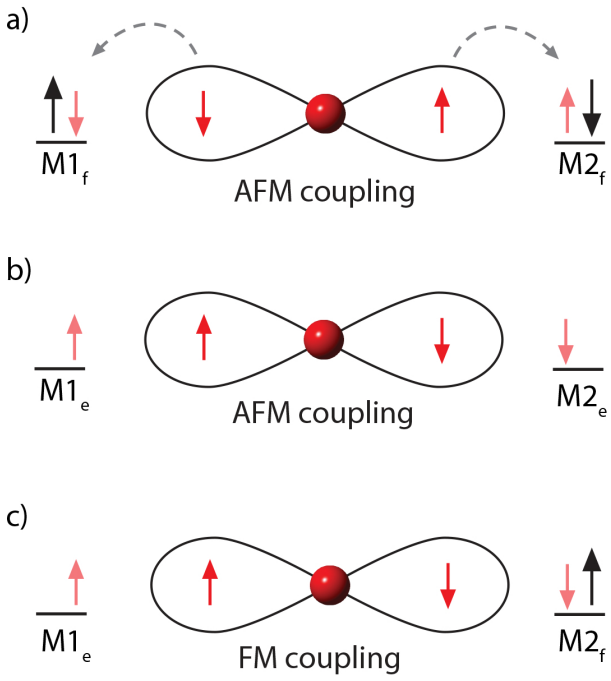

Figure 2.8: a) Schematic of the superexchange mechanism between two d^5 cations, where every d orbital is occupied by one electron. b) Schematic of the superexchange mechanism between a d^5 cation and another cation with at least one empty orbital. c) Schematic of the superexchange mechanism between two d^n cations, where $n \leq 4$ and each cation has at least one empty orbital.

suggest that the two electrons would have the lowest energy when they are parallel. This means that the spins on the two transition metal ions must also be parallel, and therefore, ferromagnetic behavior should be observed. These dependencies are articulated in the semi-empirical Goodenough-Kanamori-Anderson rules.[116–118]

Double exchange, introduced in 1951 by Clarence Zener, is a mechanism for spin coupling that arises from electron delocalization.[119] In the double exchange mechanism, an electron is shuttled from one metal cation to another through an intervening O^{2-}. As the oxygen p-orbitals are doubly occupied, the translocation first involves the movement of an electron from oxygen to M1, followed by a transfer of a second electron from M2 into the newly vacated oxygen orbital. According to Hund's rules, metallic conduction from hopping e_g electrons can only occur if the electrons of the t_{2g} orbitals for both the M1 and M2 ions are ferromagnetically aligned. Used to explain the magneto-conductive properties of mixed-valence solids, particularly doped Mn perovskites, the double-exchange mechanism thus accounts for both ferromagnetic and metallic behavior.

Expanding the nearest neighbor Hamiltonian (Eq. 2.25) to read

$$\hat{\mathscr{H}} = -2\sum J_{xy}(S_{ix}S_{jx} + S_{iy}S_{jy}) + J_z S_{iz}S_{jz} \tag{2.26}$$

three different models for exchange can be considered.

The Heisenberg model lets $J_{xy} = J_z$, allowing the spins to point in any direction. This requires isotropic exchange interactions, suggesting that the metal ions should reside at atomic sites with high symmetry.[120]

The XY model, where spins are free to point anywhere in a fixed plane, is obtained when $J_z = 0$

When $J_{xy} = 0$, the Ising exchange model is obtained, where spins are constrained to lie parallel or antiparallel to a particular direction.[120]

A one-dimensional line of spins is a spin chain. Spins may be constrained to align in one, two, or three dimensions according to the Ising, XY, or Heisenberg models, respectively. Spin chains can be approximately realized in crystals if the crystal structure keeps the chains reasonably far apart. The single ion anisotropy due to the crystal field splitting may lead to the magnetic moments behaving as Ising, XY, or Heisenberg spins, or somewhere in between. Very often these systems show three-dimensional long range order at very low temperatures because there will always be some small interchain interaction which can couple the chains together.

2.4.2 Measuring magnetic properties

2.4.2.1 SQUID magnetometry

SQUID (Superconducting QUantum Interference Device) instruments are capable of sensitive magnetization measurements, detecting very minute magnetic fields. A SQUID consists of two superconductors separated by thin insulating layers to form two parallel Josephson junctions. These junctions are superconductors separated by a thin layer small enough to allow the tunneling of Cooper electron pairs to pass through the junction. The current in the SQUID oscillates with changes

in phase at the two junctions, which depend upon the change in the magnetic flux. Counting the oscillations provides a measurement of how the flux has changed.

The sample being measured produces its own magnetic field, which is measured by a bridge circuit consisting of a primary coil and two secondary coils, wound in opposition and connected in series. When the two secondary coils are perfectly balanced, the induced voltage in the device would perfectly cancel out, but introducing a sample into one of the coils disturbs the balance of the bridge and produces a net current. This current then induces a field across the SQUID, causing the critical current to fluctuate. A constant biasing current is passed through the ring, so the voltage across the ring will fluctuate. These fluctuations are then measured while the sample is moved through the pickup coil. The field inducing the current in the pickup loop is proportional to the magnetic moment of the sample, divided by the cube of the distance between the sample and the loop. The relationship of the voltage across the SQUID and this distance allows the calculation of the dipole moment of the sample, thereby allowing the magnetization and susceptibility of the sample to be determined.

DC magnetic susceptibility measurements were collected using a Quantum Design Magnetic Property Measurement System (MPMS) SQUID instrument, located at the University of Maryland Center for Nanophysics and Advanced Materials. Measurements were taken in zero-field cooled (ZFC) and field cooled (FC) environments, from 1.8 to 300 K. Applied magnetic fields were typically 100 or 1000 Oe.

2.4.2.2 Magnetic structure determination from neutron diffraction

All methods of diffraction are sensitive to the structural symmetry of the probed material. Magnetic ordering within a structure reduces the symmetry of a material, so materials that undergo magnetic ordering at low temperatures produce different neutron scattering patterns when measured above and below their Curie or Néel temperatures. If the magnetic structure is ordered such that there are repeating patterns of moments, this will be reflected in observed magnetic Bragg peaks. When a sample is subjected to a temperature high enough to disrupt the ordering of the magnetic moments, the magnetic behavior of the material becomes the same as that observed in a paramagnet, and the scattering due to magnetic interactions fades into incoherent background on the diffraction pattern.

Another way of reaching the relationships observed in Bragg's law is through considering $\mathbf{Q}$, where $\mathbf{Q}$ represents the momentum transfer that occurs when an incident wave vector $\mathbf{k}_i$ is diffracted into final wave vector $\mathbf{k}_f$ (Figure 2.9), and is represented by the relationship

$$\mathbf{Q} = \frac{4\pi \sin\theta}{\lambda} \tag{2.27}$$

With magnetic scattering, $k_i = k_f$. When this condition is upheld, the scattering is considered elastic. (Though not discussed in Section 2.3.1, elastic scattering is a necessary condition in Bragg's law.) Unlike the variables involved in the traditional representation of Bragg's law, $\mathbf{Q}$ provides a way to study magnetic structure, regardless of the wavelength or technique used.

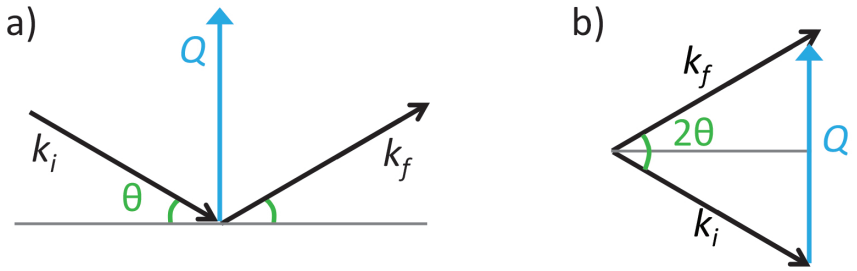

Figure 2.9: a) A schematic representation of elastic scattering, where $|\mathbf{k}_i| = |\mathbf{k}_f|$. b) A rearrangement of the scattering vectors to demonstrate wavevector transfer $\mathbf{Q}$.

The dipole-dipole interaction involved in magnetic scattering is very specific. The polarity results in highly anisotropic or directional scattering. Only the magnetization component on an atom that is perpendicular to $\mathbf{Q}$ will be reflected in the differential cross-section of the magnetic scattering. Thus, in ferromagnetic materials, the magnetic interaction can be 'turned off' if all of the atomic moments can be aligned parallel to $\mathbf{Q}$. Even more than the atomic form factor in X-ray diffraction, the magnetic form factor is dependent on the electrons present in the material, and decays at high angles of measurement.

In solving the magnetic structure of a material it is helpful to use neutron diffraction data in conjunction with other analytical techniques such as SQUID magnetometry, synchrotron X-ray scattering, Mossbauer and/or NMR spectroscopy, etc. It is not possible to solve the magnetic structure without any pre-existing understanding of the crystal structure. As mentioned previously, two types of scattering occur due to interaction with a neutron beam, and both contribute to the

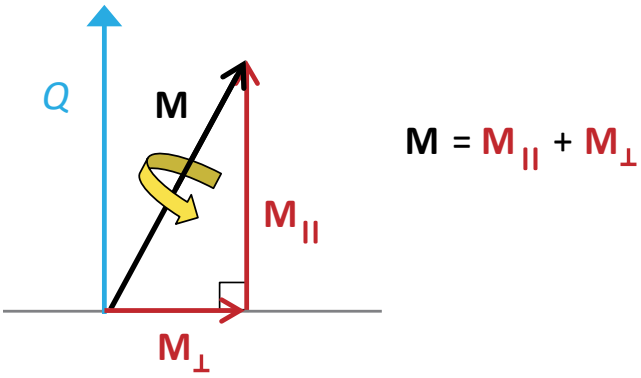

Figure 2.10: For magnetic scattering, only the magnetization component $M_\perp$ to the scattering vector **Q** contributes to the magnetic scattering length.

measured pattern. Without any prior understanding of the crystal structure of the material, it may be very difficult (if not impossible) to distinguish between the peaks occurring as a result of magnetic scattering and those caused by nuclear scattering.

Determining a magnetic structure via neutron diffraction is not a trivial process, and was first achieved by Shull and Smart in 1949 in a sample of MnO.[121,122] With the help of modern computational capabilities, Rietveld analysis may be carried out on a diffraction pattern in efforts to determine the magnetic structure.

Upon obtaining a neutron scattering pattern, there are three possible methods for refining the magnetic structure of the material. In the case where the system is simple and the unit cell has $P1$ symmetry, the magnetic structure can be solved by refining the moments in all three axis directions. A second method uses the nuclear space group observed in X-ray diffraction or high temperature neutron diffraction

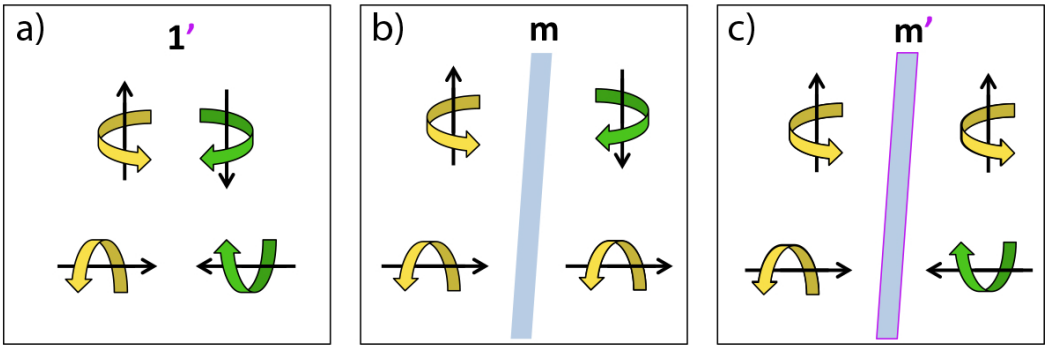

Figure 2.11: a) The time-inversion magnetic symmetry operation on an electric current loop causes the current to be reversed and the axial vector, which represents the magnetic moment, to be inverted. b) The effect of a vertical mirror plane on a current loop. The current is unchanged when the loop is parallel to the plane of the mirror. When the current loop is perpendicular to the mirror plane, the reflection symmetry operation causes the loop to reverse direction and the axial vector flips direction. c) The combination of time-inversion and a reflection symmetry operation on an electric current loop.

analyses. Anti-symmetry operations (represented by a ' in Figure 2.11) are then applied to constrain the magnetic moments within the material until a good fit is acquired. The anti-symmetry operations involved in this methodology are those proposed by Shubnikov, and are also known as 'time-reversal elements' for spin (Figure 5). In total, there are over 1600 magnetic space groups to consider when including antisymmetry elements in three dimensions, making this route somewhat tedious.

The third and most rigorous method is to utilize group theory and the irreducible representations of space groups to determine the magnetic structure. The basis vectors within the space groups will constrain the moment directions, and Rietveld analysis can then determine the goodness-of-fit. Breaking this methodology

into more detail, the first step of magnetic structure refinement is to locate and fit the individual magnetic peaks in the observed neutron data. Next, the propagation vector k is calculated based on the observed magnetic peaks. Using k and the known nuclear space group of the material, the corresponding irreducible representations and basis vectors are systematically applied, fitting the coefficients in the refinement. The basis vectors resulting in the lowest χ^2 represent the magnetic structure that best fits the observed data.

Magnetic structure refinements carried out within this thesis were predominantly performed using FullProf.[114] Another program, SARAh, is useful in validating the irreducible representations that correspond to the given space group and propagation vector.[123]

2.5 Transport measurements

The four probe van der Pauw method was employed for transport measurements on pellet samples. In order to use the van der Pauw method, the sample must be flat, of a uniform thickness, and ideally symmetrical. The length and width of the sample must be significantly larger than the sample thickness, with contacts located at the sample edge, and the area of contact minimized to the extent possible.[124,125] For transport measurements of samples described herein, contacts were established by attaching gold wires to samples with silver paint.

To make a measurement, a dc current is applied along one edge of the sample (for instance, I_{12} in figure 2.12 a) and the voltage across the opposite edge (in this

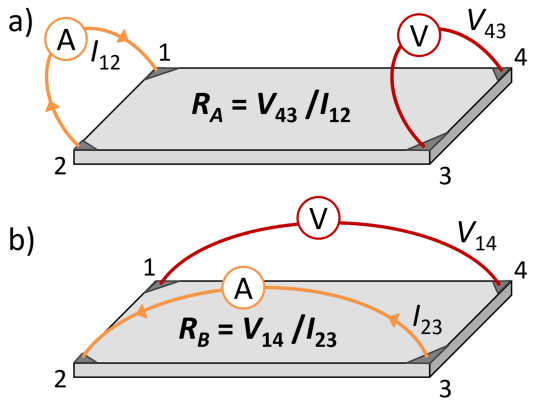

Figure 2.12: The van der Pauw technique.

case, V_{43}) is measured. From these two values, resistance (R) can be found using Ohm's law, $R = V/I$. The leads are then changed so that current is applied from contact 3 to contact 2 (I_{23} in figure 2.12 b) while voltage V_{14} is measured.

The van der Pauw equation, used to solve for the sheet resistance (R_S), is

$$\exp(-\pi R_A/R_S) + \exp(-\pi R_B/R_S) = 1 \tag{2.28}$$

where $R_A = V_{43}/I_{12}$ and $R_B = V_{14}/I_{23}$.[126] Resistivity (ρ) of the material can then be calculated by

$$\rho = \frac{AR}{l} \tag{2.29}$$

where R is the resistance, A is the area of the pellet and l is the length.

Magnetoresistance (MR) is the relative change in electrical resistance of a

material on the application of a magnetic field defined by

$$MR = \rho(H) - \rho(0)/\rho(0) \tag{2.30}$$

where MR is the magnetoresistance, $\rho(0)$ is the resistivity in zero field and $\rho(H)$ is the resistivity in an applied field.

Transport data herein was acquired using a Quantum Design physical property measurement system (PPMS) located at the University of Maryland Center for Nanophysics and Advanced Materials. Typical measurements first record the electrical resistance upon cooling the sample, then again as the sample is heated back to room temperature.

2.6 X-ray photoelectron spectroscopy (XPS)

X-ray photoelectron spectroscopy is a technique for determining the chemical composition of a surface, down to the range of parts per thousand. This is done by irradiating a sample with X-rays in a high-vacuum environment to ionize atoms and release core-level photoelectrons. The kinetic energy of the escaping photoelectrons limits the depth from which emitted photoelectrons can emerge to a few nanometers, making XPS a surface technique. Emitted photoelectrons are detected and analyzed by the instrument to produce a spectrum of emission intensity versus electron binding energy.

Since each element has a unique set of binding energies, XPS can be used to identify the elements on the surface of a material, according to an equation pro-

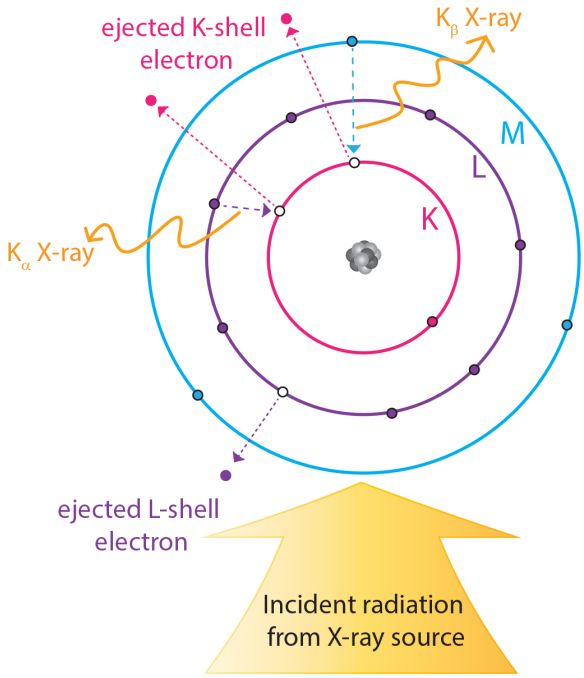

Figure 2.13: Photoelectric effect.

posed by Ernest Rutherford,

$$E_{BE} = h\nu - (E_k + \phi)$$

where E_{BE} is the binding energy of the electron, $h\nu$ is the energy of the incident X-ray photons, E_k is the kinetic energy of the emitted photoelectron measured at the detector, and ϕ is a work function dependent on both the material and the spectrometer. Peak areas at nominal binding energies can be used to quantify the concentration and ratios of the elements. Small shifts in these binding energies provide powerful information about the chemical states and short-range chemistry in a material.[127]

XPS measurements herein were taken in a high sensitivity Kratos AXIS 165

X-ray photoelectron spectrometer at the Surface Analysis Center at University of Maryland. Both the monochromatic Al Kα and the dual anode (Mg Kα and monochromatic Al Kα sources) capabilities were utilized, depending on the experimental needs as described in following chapters.

Chapter 3: $Ba_{1.2}Mn_8O_{16}$ and $Ba_{1.2}Co_xMn_{8-x}O_{16}$

The research described within this chapter was published in *Chemistry of Materials* **2015**, *27*, pg. 515-525. Dr. Pouya Moetakef, Dr. Karen Gaskell, Dr. Craig M. Brown, Dr. Graham King, and Dr. Efrain Rodriguez were contributing authors on the manuscript.

3.1 Introduction

While extensive studies have been conducted into the magnetic properties and the structure of Mn-based perovskite and pyrochlore structures, significantly less has been reported on the magnetic structures of Mn-based hollandites. Studies of the Mn-based hollandites and todorokites indicate that they are semiconducting with relatively small band gaps, whereas their magnetic behavior has been described as either long-range antiferromagnetic, ferrimagnetic, or spin glassy.[41,106] With respect to their oxidation states, the OMS-materials are understood to contain a mixture of Mn^{3+}/Mn^{4+} sites, and mineralogists and crystallographers have even identified the Jahn-Teller distorted Mn^{3+} cation (t_{2g}^3, e_g^1 electronic configuration) in certain structures. Electrochemists have studied Mn-based OMS materials for applications such as cathodes in rechargeable batteries since they are redox active

and their tunnel structures allows facile insertion and removal of cations such as Li^+. The research group of Steven Suib has also pursued catalytic studies with OMS-materials on account of their porosity including oxidation of organics such as alcohols and formaldehyde.

Manganese oxides show a range of magnetic moments due to the dependence on valence states, $S = \frac{5}{2}, 2$, and $\frac{3}{2}$ for Mn^{2+}, Mn^{3+}, and Mn^{4+} respectively. The magnetic moments are also affected by octahedral splitting resulting in high spin/low spin dependencies. Manganese oxides, MnO, Mn_3O_4, β-MnO_2, have been shown to have magnetic responses ranging from antiferromagnetic to ferromagnetic to helical magnetism, respectively. Most OMS materials generally show properties of spin glasses and paramagnetic behavior for temperatures above 100 K. Among different OMS materials, KOMS-2 is a stable form that can be synthesized with numerous methods. KOMS-2 is composed of MnO_6 edge- and corner-sharing octahedra with potassium in the tunnels to provide charge balance and stabilize the structure. Manganese atoms in the KOMS-2 structures are able to be replaced with other transition metals, which may be either diamagnetic or paramagnetic in nature. In replacing Mn with other metals, there is tunability in the magnetic response of the material.

Within the research that has been done on manganese-based hollandites, those with tunnel cation Ba^{2+} are rather under-represented compared to the K^+ analogue (Chapter 4). A reported salt flux reaction combined $Ba(NO_3)_2$ with Mn_2O_3 and KCl in a 1.2:4:12 molar ratio to produce polycrystalline samples of $Ba_xMn_8O_{16}$, with impurity phases obtained for $1.1 \leq x \leq 1.3$.[104] In another study, nanoribbons

of $Ba_{1-\delta}Mn_8O_{16}$ were prepared by mixing $BaMnO_3$ in a 1:1 molar KCl/NaCl flux and heating to 800° C for five hours, achieving phase pure product with good crystallinity.[106]

Different strategies to modify the physical and chemical properties of Mn-based hollandites have involved introducing, exchanging, or removing ions in the tunnels and/or framework, but only two studies have reported these effects on barium manganate hollandites. In 2014, Liu et al reported a "gel-collection" synthetic technique to produce mixed metal hollandites, where A = Ba, and M = Mn, Ti hollandites.[87] Their reported technique combined the more traditional solvothermal and sol-gel synthetic techniques, with barium isopropoxide, manganese acetylacetonate, and titanium isopropoxide mixed together in a 1:3:4 molar atomic ratio, using pure ethanol as the solvent. Heating this solution in an autoclave at 150° C for 24 hours produces a 'gel-rod', which is then removed from the supernatant and sintered at 700° C to yield $BaMn_3Ti_4O_{14.25}$. Broad diffraction peaks indicated low crystallinity, but the hollandite structure was confirmed by synchrotron XRD and pair distribution function (PDF) refinements, as well as spherical-aberration corrected STEM measurements. Electric and magnetic property measurements of the sample hinted at multiferroic behavior, though reproducing these measurements on samples with improved crystallinity would be more convincing.[87]

Barbato et al used solid state salt flux reactions to synthesize $BaMMn_7O_{16}$, where M = Mg, Mn, Fe, or Ni.[85] Broad diffraction peaks in their X-ray diffraction data indicated poor crystallinity of the samples, all of which were identified as monoclinic. In the hollandites synthesized by Barbato et al, small changes were

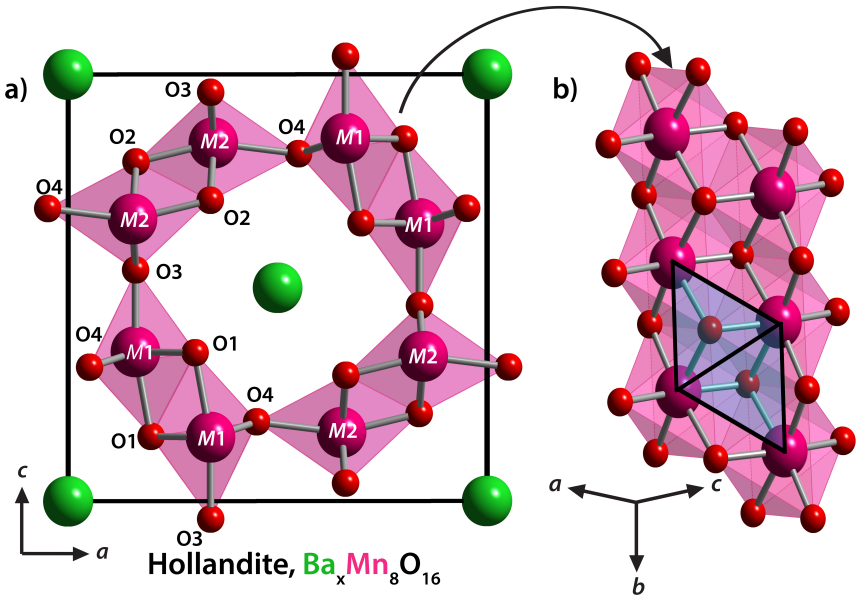

Figure 3.1: a)$Ba_{1.2}Mn_8O_{16}$ hollandite structure viewed down the *b* axis in the *I*2/*m* setting. b) Tunnel wall of hollandite showing the triangular ladder.

observed in lattice parameters corresponding to the cationic radius of the *M* cation incorporated into the framework. Their study focused on the ability of Li^+ cations to insert into the tunnels of each material for electrochemical applications, with *M* = Ni displaying the maximum reactivity.

Despite the paucity of reports on the barium manganate hollandite, doping of low- or high-valent transition metal ions into the framework should result in novel physical and electronic properties, especially as the oxidation state of the manganese atoms is so dependent upon the identities of the other framework cations.

In the 2006 investigation of the physical properties of $Ba_{1.2}Mn_8O_{16}$ Ishiwata et al observed a magnetic transition at 40 K, and at low temperatures, sintered pellets of $Ba_{1.2}Mn_8O_{16}$ demonstrated high resistivity.[104] Low temperature neutron

data displayed broad magnetic Bragg reflections indexed with a (1/2 0 1/2) superlattice, though no detailed magnetic structure was proposed.

The combination of ferrimagnetism with insulating properties is uncommon, and further analysis of the $Ba_{1.2}Mn_8O_{16}$ framework was desired. The prescribed synthetic route producing the polycrystalline $Ba_{1.2}Mn_8O_{16}$ material also accommodated the synthesis of a related derivative with Co incorporated into the framework.

This chapter presents a detailed characterization of the $Ba_{1.2}Mn_8O_{16}$ hollandite system, and its Co-substituted analogue, where one stoichiometric equivalent of cobalt was added into the Mn_8O_{16} framework. The choice of Co as a dopant is advantageous due to its magnetic properties, as well as its similarity in size, allowing facile incorporation into the manganese oxide framework. A combination of inductively coupled plasma- mass spectrometry (ICP-MS), conventional lab and synchrotron X-ray diffraction (XRD), X-ray photoelectron spectroscopy (XPS), neutron powder diffraction (NPD), magnetometry, and transport measurements have been employed to study the composition, magnetic structure and physical properties. Of particular interest is how the presence of cobalt affects the complex, frustrated magnetism of the system.

3.2 Synthesis & experimental details

3.2.1 Sample preparation

Samples were synthesized through the salt flux method described by Ishiwata et al. to produce the polycrystalline hollandite, $Ba_{1.2}Mn_8O_{16}$.[104] Starting

reagents included KCl (99.2%, J.T. Baker), Mn_2O_3 (99%, Sigma-Aldrich), Co_3O_4 (74%-gravimetric Co, Sigma-Aldrich), $Ba(NO_3)_2$ (99.999%, Sigma-Aldrich). Reagents were used without further purification.

A powder mixture with molar ratio of 1.2:4:12 of $Ba(NO_3)_2$, Mn_2O_3, and KCl was ground with an agate mortar and pestle to obtain a target stoichiometry of $Ba_{1.2}Mn_8O_{16}$ (BMO). For the cobalt-doped sample a stoichiometric mixture of the metals is mixed with the KCl flux in a 1:12 ratio to target a stoichiometry of $Ba_{1.2}CoMn_7O_{16}$ (BCMO). Both materials were then heated in covered alumina crucibles under ambient atmosphere. Heating was maintained at a rate of 100 K/h up to 1123 K, soaked for 72 h, then cooled to room temperature at 100 K/h. The obtained samples were washed in DI water to dissolve KCl, then dried at 373 K for one hour. Small impurities of $BaCO_3$ were removed by stirring samples in 1M HCl for 30 min, then washing with DI water until pH returned to neutral.

For inductively coupled plasma mass spectrometry (ICP-MS) measurements, ~10 mg of sample was stirred in 5 mL concentrated HCl until completely dissolved, then diluted appropriately for analysis. For resistivity measurements sample powders were pressed into pellets 1 mm thick and 13 mm in diameter. Pellets were sintered at 1173 K for 24 h.

3.2.2 Diffraction, magnetization, and spectroscopy

Room temperature powder X-ray diffraction (XRD) data was collected on a Bruker D8 X-ray diffractometer with Cu Kα radiation, λ = 1.5418 Å, (step size=0.013°,

with 2θ range from 8°-140°). Time-of-flight (TOF) neutron powder diffraction (NPD) data was collected on the High Intensity Powder Diffractometer (HIPD) beam line at the Lujan Neutron Scattering Center at Los Alamos Neutron Science Center. Low temperature constant wavelength (CW) neutron diffraction data was collected on the BT-1 high resolution powder neutron diffractometer at the NIST Center for Neutron Research. Cu(311) and Ge(311) monochromators produced neutron beams of λ = 1.5403 Å and λ = 2.078 Å, respectively. Scans were taken at 5 K, 10 K, and 50 K for BMO, and at 10 K, 40 K, 80 K, 120 K, 160 K, 180 K, 250 K, and 300 K for BCMO.

Magnetic susceptibility measurements were carried out using a magnetic property measurement system (Quantum Design MPMS). Both field-cooled (FC) and zero-field-cooled (ZFC) magnetic susceptibility measurements were taken from 2 K - 300 K in direct current mode with an applied magnetic field of 0.01 T (100 Oe). Hysteresis measurements were carried out at 2 K in magnetic fields between ± 7 T.

A Quantum Design physical property measurement system (PPMS) was used for temperature dependent resistivity measurements using a four-probe, or Van der Pauw geometry.[124,125] Sintered pellets were mounted onto a PPMS puck with electrical continuity established by using silver paste to connect gold wires from the pellet to the sample mount.

X-ray photoelectron spectroscopy (XPS) measurements were taken in a high sensitivity Kratos AXIS 165 X-ray photoelectron spectrometer operating in hybrid mode to analyze the composition and average transition metal oxidation state at the surface. For the Mn 2p peaks, monochromatic Al Kα at 280 W was used as

the X-ray energy source, whereas both Mg Kα and monochromatic Al Kα sources were utilized (at 280 W) in studying the Co 2p peaks in efforts to better resolve peak overlaps. CasaXPS software was used for quantification and peak fitting after application of Shirley backgrounds using relative sensitivity factors from the Kratos vision library. Pressure was at or below 5×10^{-8} Torr during data collection, and charge neutralization was required to minimize surface charging.

3.3 Results and discussion

3.3.1 Crystal structure

As-synthesized XRD patterns were taken to measure crystal structure and purity. Rietveld refinement of both BMO and BCMO structures were carried out with the TOPAS 4.2 software.[115] The patterns of as-synthesized samples showed good fit to the structure reported by Ishiwata et al, including an impurity peak at $2\theta \sim 24.1-24.5°$, which was reported in the literature but remained unidentified.[104] This peak corresponds to the impurity phase $BaCO_3$. Stirring the sample in 1M HCl for 30 min followed by washing until the pH returned to neutral removed most of the $BaCO_3$ phase without diminishing the crystallinity of the oxides.

The crystal structures of BCMO and BMO at room temperature were solved by simultaneously fitting banks 1, 3, and 5 of the TOF neutron diffraction data measured on HIPD (Figures 3.2 and 3.3, respectively). The resulting patterns were fit with a monoclinic cell (space group $I2/m$) with the parameters presented in Tables 3.1 and 3.2.

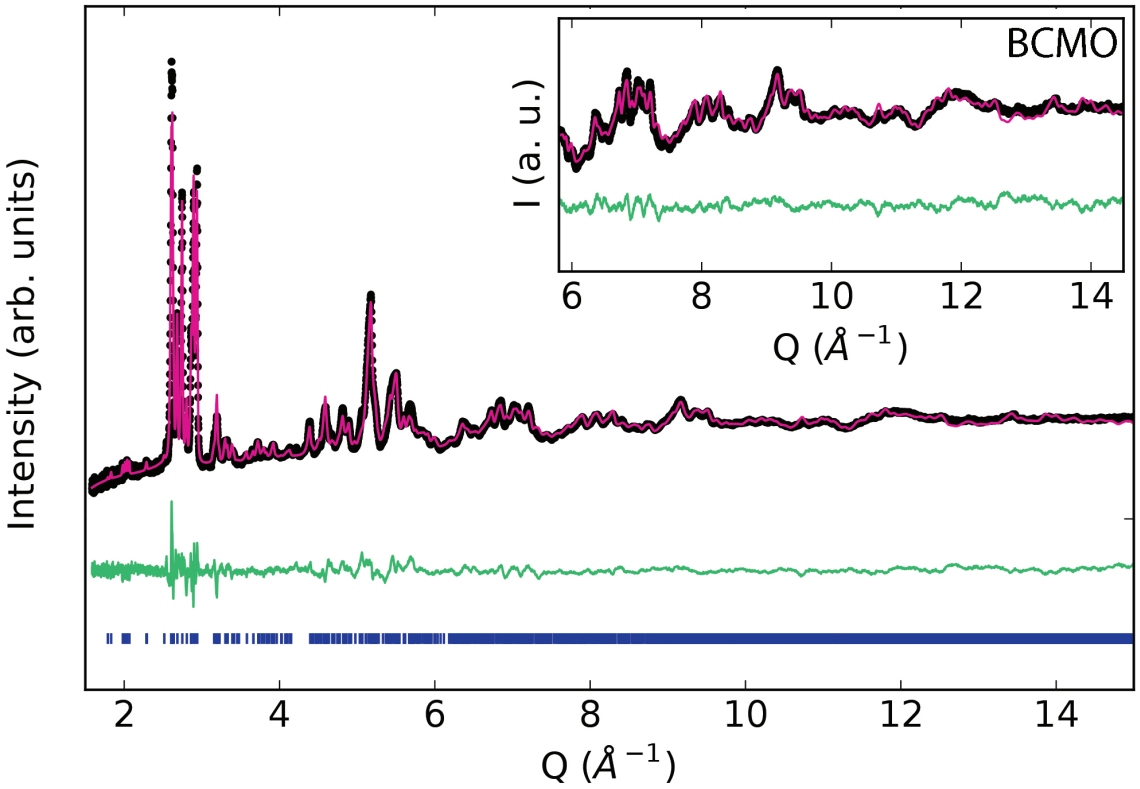

Figure 3.2: Rietveld refinement of the TOF neutron data (HIPD, Los Alamos) for the structure of BCMO. The highest resolution is found in the backscattering 153° bank, which also has the highest Q-range. The blue tick marks indicate expected positions of hollandite reflections, the green line indicates the difference between the observed data (black circles) and the calculated model (pink). The inset allows for better visualization of the structural details and refinement that occur at $Q > 6\text{Å}^{-1}$. The BCMO fit to the data measured at the 90° and 40° detector banks are available in Appendix B.

The refined occupancy of the Ba site is 0.28(2) in BMO and 0.27(2) in BCMO, slightly less than the targeted stoichiometry (0.3 per site). This discrepancy can be accounted for in the $BaCO_3$ impurities removed by HCl washing, which may have also leached a small amount of Ba cations from the hollandite tunnels. The large values for the Ba thermal displacement parameters are likely a result of the loose coordination environment of the Ba cation within the framework, allowing increased tunnel cation mobility. Previous studies of hollandite frameworks have seen incommensurate modulations of the tunnel cation, visible in electron microscopy images as sharp satellite peaks or diffuse intensity normal to the tunnel direction.[86,88,128]

Composition analysis via Rietveld refinement of neutron data provides a first approximation of whether or not cobalt was successfully incorporated into the hollandite structure. The refined Co occupancy in BCMO is 0.40(8) per unit cell, in contrast to the expected value of one Co atom per cell. However, as the overall Co concentration is small, the error relative to the total amount of Co is large. Although the neutron scattering lengths of Co and Mn have fairly good contrast, (2.49 fm in Co vs. -3.73 fm in Mn), the absolute values of the scattering lengths are fairly small relative to those of either Ba (5.07 fm) or O (5.803 fm).[109] Thus, small changes in composition between Mn and Co are expected to only affect small changes in the observed diffraction pattern. The refined composition from neutron data therefore are useful in confirming the presence of Co, but other elemental analyses are capable of achieving greater compositional precision between Mn and Co. These methods are presented in the Elemental Analysis section.

Further evaluation of the metal-oxide bond distances determined from diffraction data allow inference of the amount of Mn^{3+} and Co^{2+} present in BMO and BCMO, respectively. The target stoichiometry of $Ba_{1.2}Mn_8O_{16}$ would lead to an average oxidation state of 3.7+ per manganese cation. Introduction of Co^{2+} into the framework structure should cause the manganese to oxidize in order to maintain charge balance, with an expected oxidation state per manganese cation of 3.94+ for the target stoichiometry of $Ba_{1.2}CoMn_7O_{16}$. From a bond valence perspective, the lower valent cations are larger than Mn^{4+} and should thus lead to larger average *M*-O bond distances.

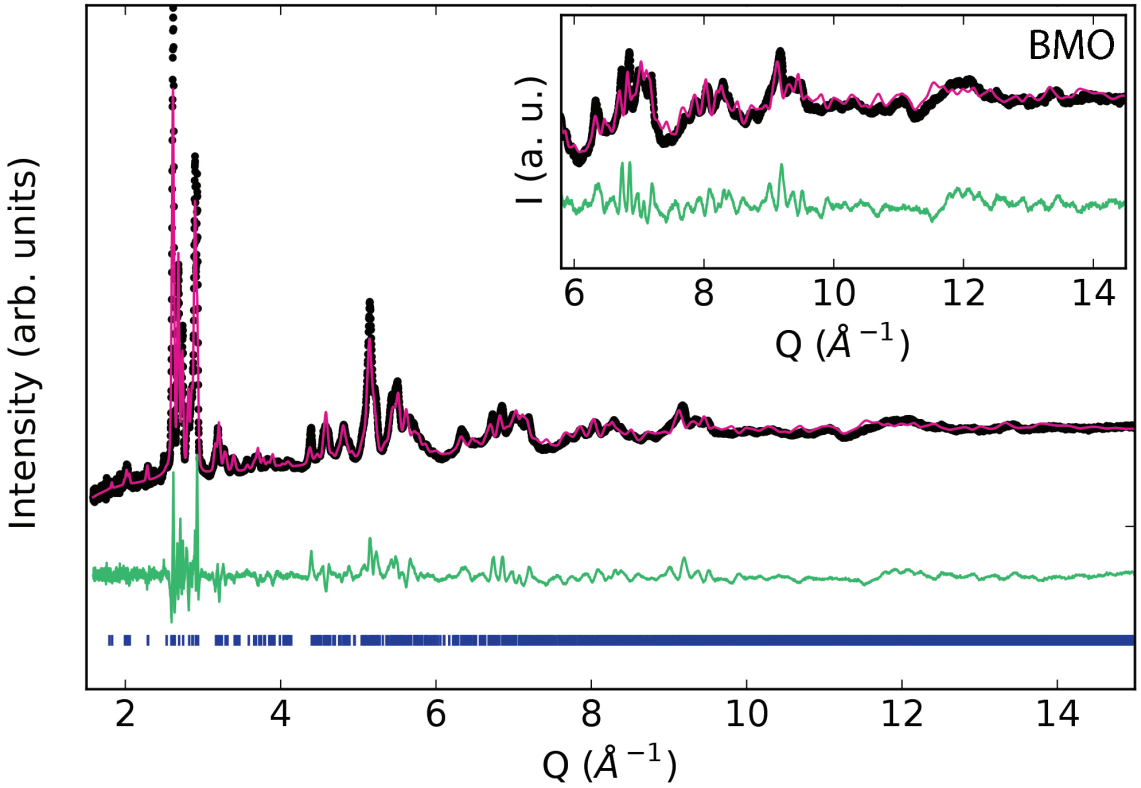

Figure 3.3: Rietveld refinement of the TOF neutron data (HIPD, Los Alamos) for the structure of BMO. The highest resolution is found in the backscattering 153° bank, which also has the highest Q-range. The blue tick marks indicate expected positions of hollandite reflections, the green line indicates the difference between the observed data (black circles) and the calculated model (pink). The inset allows for better visualization of the structural details and refinement that occur at $Q > 6\text{Å}^{-1}$. The BMO fit to the data measured at the 90° and 40° detector banks are available in Appendix B.

To assess the effects of Co-substitution on the crystal structure, the metal-oxide bond distances in BMO must first be analyzed. As observed in a sample of pyrolusite MnO_2,[129] Mn^{4+} has an average Mn–O bond length of ~ 1.89 Å whereas Mn^{3+} has an average Mn–O bond length of 2.04 Å.[130] The average M–O bond lengths obtained from room temperature refinements of BMO are 1.893 Å and 1.956 Å for the $M1$ and $M2$ sites, respectively (Table 3.3). These bond lengths suggest that Mn^{4+} preferentially occupies the $M1$ site, while both Mn^{3+} and Mn^{4+} cations occupy the $M2$ position in an approximately 1:1 ratio. These bond distance values imply an average Mn oxidation state of 3.75+ in BMO, slightly higher than the target of 3.7+. These values can be further quantified using the bond valence method of Brown, Brese, and O'Keeffe[131–133] and the empirical bond valence parameter for Mn^{4+}. These calculations lead to the $M1$ site having a valence of 4.12 and the $M2$ site 3.53.

In BCMO, the average bond lengths are 1.908 Å and 1.942 Å for the $M1$ and $M2$ positions, respectively (Table 3.4). In a high-spin octahedral configuration, Co^{2+} should have a bond length of 2.14 Å.[130] These values suggest that Mn^{4+} still favors the $M1$ site and that Co^{2+} mixes with Mn^{4+} at the $M2$ position in a nearly 1:3 ratio, assuming no Mn^{3+} is found in BCMO. The same bond valence treatment of the bond distances leads to an $M1$ valence of 4.02 and an $M2$ valence of 3.67. From these calculations, it appears that the charge difference between M sites is diminished in BCMO relative to BMO, as would be expected from the oxidation of Mn upon Co^{2+} substitution. Since these results are obtained from the average structure refinement of Bragg peaks, the location of cobalt substitution is not certain based solely

on arguments of average bond length. Thus, further investigations into the local structure are needed to determine possible local ordering in BCMO.

The Mn^{3+} cation, which seems to favor the $M2$ atomic position in BMO, could potentially undergo a Jahn-Teller (JT) distortion, elongating in a direction parallel to the a-axis of the unit cell. An evaluation of the bond distances in BMO (Table 3.3) shows that $M2$–O2 and $M2$–O4 are both over 2.0 Å and longer than the other distances. However, this elongation does not correspond to the expected JT elongation along one axis, but instead indicates a trigonal distortion of the octahera, with one trigonal face further from the metal center than the other. In contrast, the equivalent $M2$–O bond distances in BCMO are shortened, which is further evidence that the JT-active Mn^{3+} cation is no longer present in BCMO due to Co^{2+} substitution. Future TOF neutron experiments at temperatures below the magnetic ordering transitions will be helpful to search for possible orbital ordering from JT distortions.

3.3.2 Elemental analysis

Before presenting the magnetic properties of BMO and BCMO, the elemental analysis of both BMO and BCMO is presented in order to understand the effects of Co-substitution on structure and composition. To this end, XPS measurements were utilized to determine metal oxidation states by studying the $2p$ and $3s$ X-ray core level photoelectron spectra, and ICP-MS was used to verify the elemental composition of the samples.

Table 3.1: Room temperature lattice parameters for $Ba_xMn_8O_{16}$ and $Ba_xCo_yMn_{8-y}O_{16}$ from TOF neutron diffraction refinements. Standard uncertainties are given in parentheses.

Sample	$Ba_{1.14}Mn_8O_{16}$ (BMO)	$Ba_{1.10}Co_yMn_{8-y}O_{16}$ (BCMO)
No. reflections	2545	2560
No. parameters*	29	31
Space group	$I2/m$	$I2/m$
a (Å)	9.683(2)	9.6468(8)
b (Å)	2.8531(5)	2.8589(2)
c (Å)	9.946(2)	9.9954(8)
$\beta(^\circ)$	88.907(3)	88.654(3)
Volume ($Å^3$)	273.9557(3)	275.6637(1)
Calc. density (g/cm^3)	5.161(2)	5.11(8)

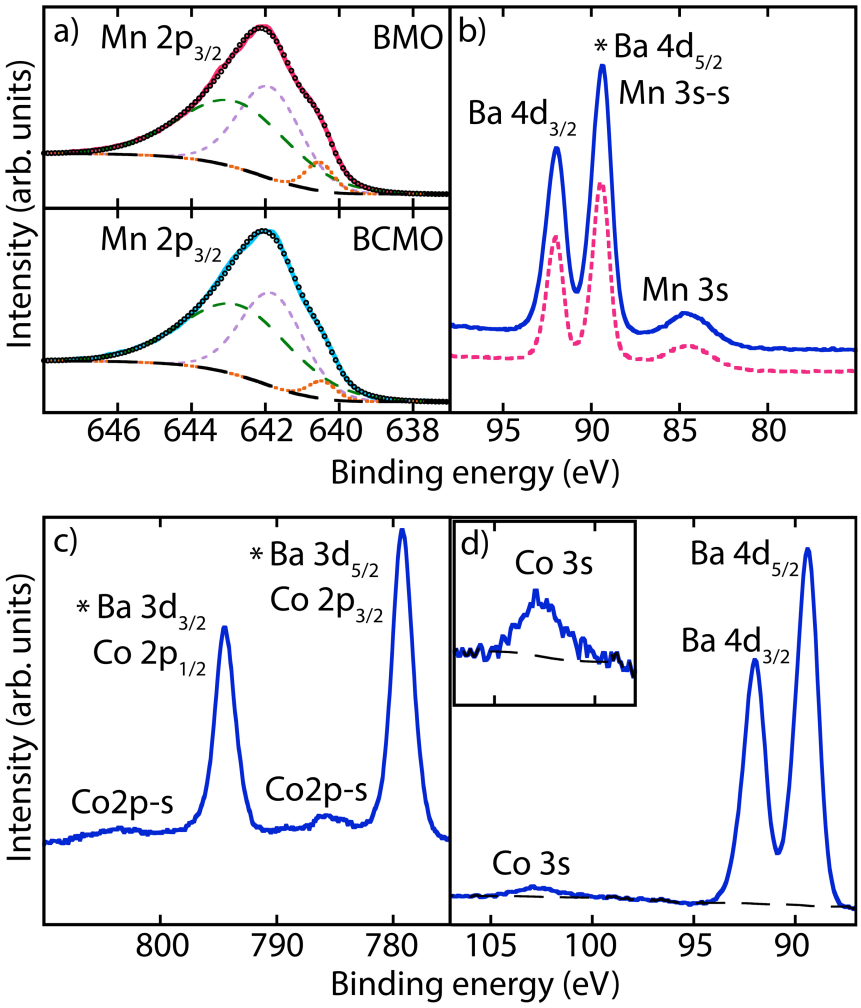

Figure 3.4: XPS spectra of M $2p$ and M $3s$ peaks in BMO (dotted pink) and BCMO (solid blue). M = Mn in panels a and b, and M = Co in c and d. Mn $2p_{1/2}$ was not shown in panel a to better emphasize the subtle difference in fit of the higher resolution Mn $2p_{3/2}$ peak. Asterisks indicate M peaks overlapping with Ba peaks. Dashed black lines show the background used for composition quantification.

Qualitatively, the asymmetry present in the Mn $2p_{3/2}$ peak of BMO and BCMO (Figure 3.4a) matches that reported for mixed-valent Mn by Militello et al in $LiMn_2O_4$,[134] which is consistent with expected mixed valency in hollandites. Unfortunately, the splitting of the Mn $2p$ peaks is not helpful in assigning definitive oxidation states since literature values for the splitting of Mn^{4+}, $Mn^{3.5+}$, Mn^{3+} are 11.7, 11.7, and 11.6 eV, respectively.[134–136] Furthermore, overlap of the Ba $4d_{5/2}$ peak with the higher binding energy Mn $3s$ multiplet (Figure 3.4b) complicated the analysis since the oxidation state of manganese is most reliably determined via splitting between the two Mn $3s$ multiplets.

To extract more information about the Mn state from the XPS data, a careful comparison of the Mn $2p_{3/2}$ peak shape in BMO to that in BCMO was performed. The peak shape for Mn $2p_{3/2}$ shows an asymmetric shoulder at lower binding energy (Figures 3.4a). The Mn $2p_{3/2}$ transition was fit with three peaks constrained to occur at the same binding energies and with the same full width at half maximum between the BMO and BCMO spectra. A change in the intensity of the lowest binding energy peak is observed, increasing from BCMO to BMO. Previously reported XPS measurements of binary Mn oxides show that the Mn $2p_{3/2}$ peak occurred at a slightly lower binding energy (-0.6 eV) in Mn_2O_3 than in MnO_2.[129,130] Thus, if the intensity of the peak fit at lower binding energy is proportional to the amount of Mn^{3+} in the sample, there is more Mn^{3+} present in BMO, leading to a lower average Mn oxidation state than in BCMO.

In the BCMO sample, the Co $2p$ peaks overlapped with Ba $3d$ peaks. The presence of the Co $2p$ satellite peaks, however, is characteristic of cobalt atoms in

the high spin 2+ oxidation state (Figures 3.4c). These satellite peaks give good certainty to the assumption that the cobalt cations within the bulk of the material are also divalent, since the propensity for oxidation is greatest for exposed cations at the surface.[137]

Quantification to obtain surface stoichiometry was carried out using the Ba $3d$ and $4d$ peaks for BMO and BCMO, respectively, as well as the Mn $2p$ and Co $3s$ peaks. Composition analyses of all obtained methods are listed in Table 3.5, with XPS measurements resulting in the surface stoichiometries of $Ba_{1.4}Co_{0.79}Mn_{7.2}$ and $Ba_{1.5}Mn_8$. In both samples, the results revealed more Ba than expected based on initial stoichiometry. The discrepancy in Ba might be due to Ba cations moving to the surface during either the HCl wash or while the system is in the high vacuum XPS environment.

Investigating the sample composition via inductively-coupled plasma mass spectrometry (ICP-MS) gave stoichiometries of $Ba_{1.6}Mn_8O_{16}$ for BMO, which suggests an average manganese oxidation state of 3.6+. The composition of BCMO via ICP-MS gave a stoichiometry of $Ba_{1.5}Co_{0.9}Mn_{7.1}O_{16}$. Assuming Co is 2+ (as seen in the XPS data), this leads to an average manganese oxidation state of 3.83+.

3.3.3 Magnetic properties

Field-cooled (FC) and zero-field-cooled (ZFC) measurements were taken of both samples with and without acid washing (Figures 3.5 and 3.6). Preliminary analysis of the magnetic susceptibility of BCMO compared to BMO revealed a dra-

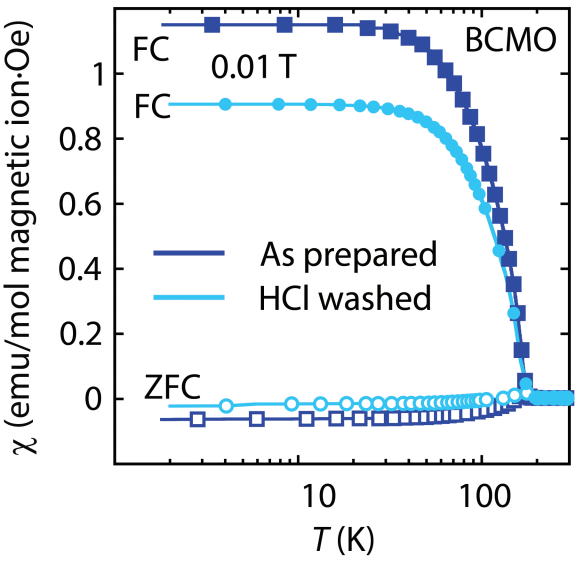

Figure 3.5: Magnetic susceptibility as a function of temperature for as-prepared and acid-washed samples of BCMO.

matic change in the magnetic response of the oxide. FC/ZFC curves of BMO show the susceptibility to be virtually identical above 25 K irrespective of the applied magnetic field, with the magnetic responses diverging at low temperature. This is different than the T_N reported for bulk $Ba_{1.2}Mn_8O_{16}$ by Ishiwata et al, but agrees with the magnetic behavior observed by Yu et al in their single crystal investigation of $Ba_{1+\delta}Mn_8O_{16}$ nanoribbon crystals.[104,106] The low-temperature divergence of the FC/ZFC curves in the manganese sample supports the observations of Suib and Iton, who classified manganese oxide hollandite materials as spin-glass systems.[12,41]

An increase in magnetic susceptibility (χ) of BCMO was observed with an onset near 180 K and saturation near 22 K, indicative of long-range ferri- or ferromagnetic ordering. The temperature and the magnitude of FC/ZFC divergence of

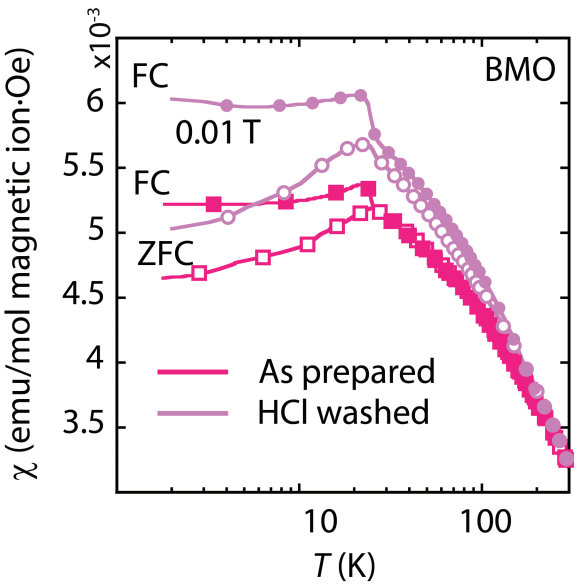

Figure 3.6: Magnetic susceptibility as a function of temperature for as-prepared and acid-washed sampels of BMO.

BCMO at 180 K contrast significantly with those observed in the pure manganese sample. At 2 K the $\Delta\chi$ is approximately 1×10^{-3} between the FC and ZFC curve for BMO, whereas in BCMO the $\Delta\chi$ at 2 K is ~1, a difference of three orders of magnitude.

The effective paramagnetic moment (μ_{eff}), the Curie constant C, and the Curie-Weiss intercept θ_{CW} values for BMO and BCMO were obtained by fitting the linear high temperature region (T > 225 K) of the χ^{-1} plots to the Curie-Weiss equation, $\chi = C/(T - \theta_{CW})$. The obtained values are recorded in Table 3.6. Based on the compositions observed via ICP-MS where the average Mn oxidation state is 3.6+, an effective magnetic moment of 4.28 μ_B is expected for BMO. The calculated μ_{eff} value of 4.34 μ_B for the as-prepared BMO sample agrees relatively well with the expected value.

On the basis of the average Mn oxidation state of 3.83+ in BCMO, the spin-only contribution from the manganese cations to the effective magnetic moment should be 4.05 μ_B. A μ_{eff} of ~ 4.3μ_B to 5.2 μ_B is the reported value for Co^{2+} cations in the high-spin configuration, a result of both spin and orbital contributions.[9,120] Thus, in BCMO the combination of $Mn^{3.83+}$ and Co^{2+} would be expected to result in a μ_{eff} of ~ 4.14μ_B. The obtained value for μ_{eff} in BCMO is instead 4.64 μ_B, which is significantly higher than expected. Since the transition temperature observed in BCMO is 180 K, the linear region used to fit for the Curie-Weiss law (T > 225 K) in the measured data may be too close to the transition temperature to allow for accurate determination of magnetic constants. The Curie constant from the fits for both BMO and BCMO are therefore both included, as this may allow a more straightforward assessment of the consequences of substituting Co^{2+} on the bulk magnetic properties.

The decrease in μ_{eff} observed in both samples upon acid washing supports the conclusion that Ba^{2+} cations are deintercalating from the tunnels during the acid wash process, causing the framework transition metal cations to further oxidize. Although the Néel temperature in BMO is 25 K, the absolute value of θ_{CW} for BMO is quite large, indicating strong antiferromagnetic exchange. Ramirez defined a frustration index f as the ratio of the Weiss field to the ordering temperature, where $f = |\theta_{CW}|/T_N$.[12,24] A highly frustrated system is classified as one where $f > 10$, and in BMO, $f \sim 17$. Such significant spin frustration within the framework is often seen in triangular lattices of edge-sharing MO_6 octahedra (Fig. 3.1). In BCMO, $f \sim$ 3.5, indicating that the Co^{2+} substitution effectively relieved the highly frustrated

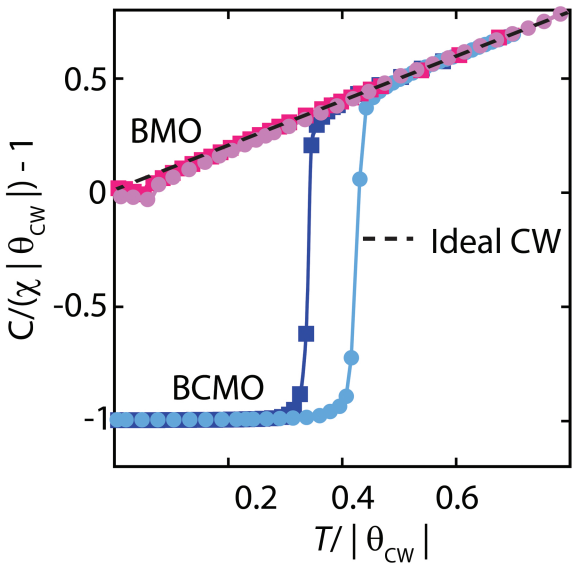

Figure 3.7: Standardized inverse magnetic susceptibility, with the dotted line representing the ideal antiferromagnetic Curie-Weiss fit.

state of the hollandite.

The standardized χ^{-1} plot shown in Figure 3.7 allows for the direct comparison of BMO and BCMO. The dashed line passing through the origin corresponds to ideal Curie-Weiss behavior and can be used to measure the fit quality in the high temperature paramagnetic regime. The observed negative deviations from the ideal Curie-Weiss line indicate uncompensated antiferromagnetism (ferrimagnetism) present in the sample.[138] Overall, the magnetization data support a partially saturated ferrimagnetic ground state in BCMO.

The ferrimagnetic behavior of the BCMO sample contrasts with the Co-doped analogue of a titanium hollandite, $Ba_{1.3}Co_{1.3}Ti_{6.7}O_{16}$, studied by Shlyk et al, which did not demonstrate any long-range magnetic order down to 2 K. Extrapolation of the high-temperature paramagnetic fit for the titanate hollandite produced a

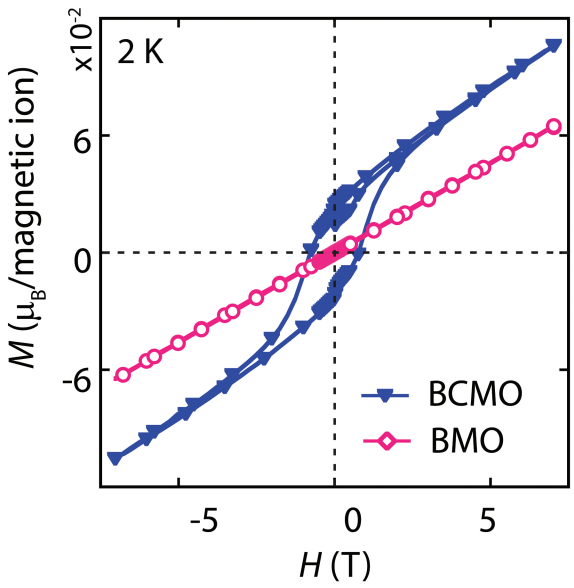

Figure 3.8: Comparison between the experimental measurements of magnetization as a function of applied field for BCMO (blue), and BMO (pink).

Curie-Weiss constant of θ = 6.4 K, indicative of very weak ferromagnetic coupling between the Co ions.[81] Likewise, the study by Moetakef et al revealed no long-range magnetic ordering in the hollandite $K_{1.4}Co_{0.75}Ti_{7.25}O_{16}$.[75]

Magnetization versus magnetic field measurements of BMO and BCMO show that the presence of cobalt within the hollandite structure opens up a hysteresis loop with a coercivity of ~1 T (Figure 3.8). Magnetic saturation of BCMO was not observed within the field range of the MPMS instrument. To further elucidate the magnetic ordering, neutron powder diffraction patterns were taken of the as-synthesized BCMO sample at 10, 40, 80, 120, 160, 180, 250, and 300 K. One magnetic peak was observed below 180 K, at $2\theta \sim 25°$, which was indexed as the (200) reflection. The observed magnetic peak intensity was normalized and plotted

with good agreement to the normalized field-cooled susceptibility of BCMO (Figure 3.10). The agreement of these data and successful refinement of the magnetic structure accounting for the magnetic neutron peaks (discussed in Section 3.3.4) confirm that the observed magnetization is a property of the bulk sample and is not due to the presence of minute impurities.

3.3.4 Magnetic structure from neutrons

As indicated by the magnetization measurements, remarkably different long-rage magnetic ordering is observed between BMO and BCMO. To solve the magnetic structures from the base temperature NPD data, the representational analysis method was used.

For BMO, the magnetic Bragg peaks were indexed according to the propagation vector of $\mathbf{k} = (\frac{1}{4}, \frac{1}{8}, \frac{1}{4})$, which corresponds to a large magnetic unit cell with respect to the chemical unit cell ($4a \times 8b \times 4c$). The BASIREPS routine in FullProf produced the irreducible representation associated with this $\mathbf{k}$ vector for space group $I2/m$ (Table 3.7). The representation indicates that Mn sites ($M1$ and $M2$) are each split into two orbits (e.g. $M1_a$ and $M1_b$ in Table 3.7) so that in total there are four independent basis functions. The different orbits are due to each Mn-site having an independent set of basis functions generated by the $2/m$ symmetry of the space group. The refinement was only stable, however, if the two orbits corresponding to the same site were ferromagnetically coupled. This constraint is also due to the paucity of well-defined magnetic reflections in the BMO powder sample.

The best fit to the powder data (Figure 3.9b) led to an antiferromagnetic coupling between $M1$ and $M2$ so that BMO exhibited no net magnetization, as anticipated from the SQUID measurements. The magnetic R-factor from this fit was 46%, while the next model with antiferromagnetic ordering along the b-direction led to a magnetic R-factor of 55%. The next models lead consistently to even higher magnetic R-factors of $\geq 87\%$. Thus, the best fit given the quality of the powder data favors a magnetic moment mostly in the ac-plane.

The complex structure of BMO is depicted in Figure 3.9c, showing antiferromagnetic moments aligned along the [1 0 1]-direction. The direction and size of the moment in the ac-plane is modulated by the propagation vector, indicating that the structure may be that of a complex helical ordering. This is consistent with the helical ordering proposed by Sato et al for $K_{1.5}Mn_8O_{16}$, where they expected the period of the charge ordering (λ_C) to be an integral multiple of the helical magnetic structure. Further, they expected the λ_C to be eight times as large as the unit cell parameter parallel to the tunnel direction (similar to the $8b$ component of our magnetic propagation vector in BMO).[64,139] The maximum moment size in the ac-plane from fitting the Bragg intensities was $2.3(2)\mu_B$, which is lower than the expected $3.2\mu_B$ for $Mn^{3.8+}$ cations. Figure 3.9a shows a large diffuse background, however, around the most intense satellite peak of (-1 0 1). Therefore, a large amount of the magnetic moment may be disordered leading to the background instead of contributing to the Bragg reflections.

Remarkably, for BCMO only one magnetic peak was observed at low temperatures, indicating a dramatic change in the magnetic ordering compared to BMO.

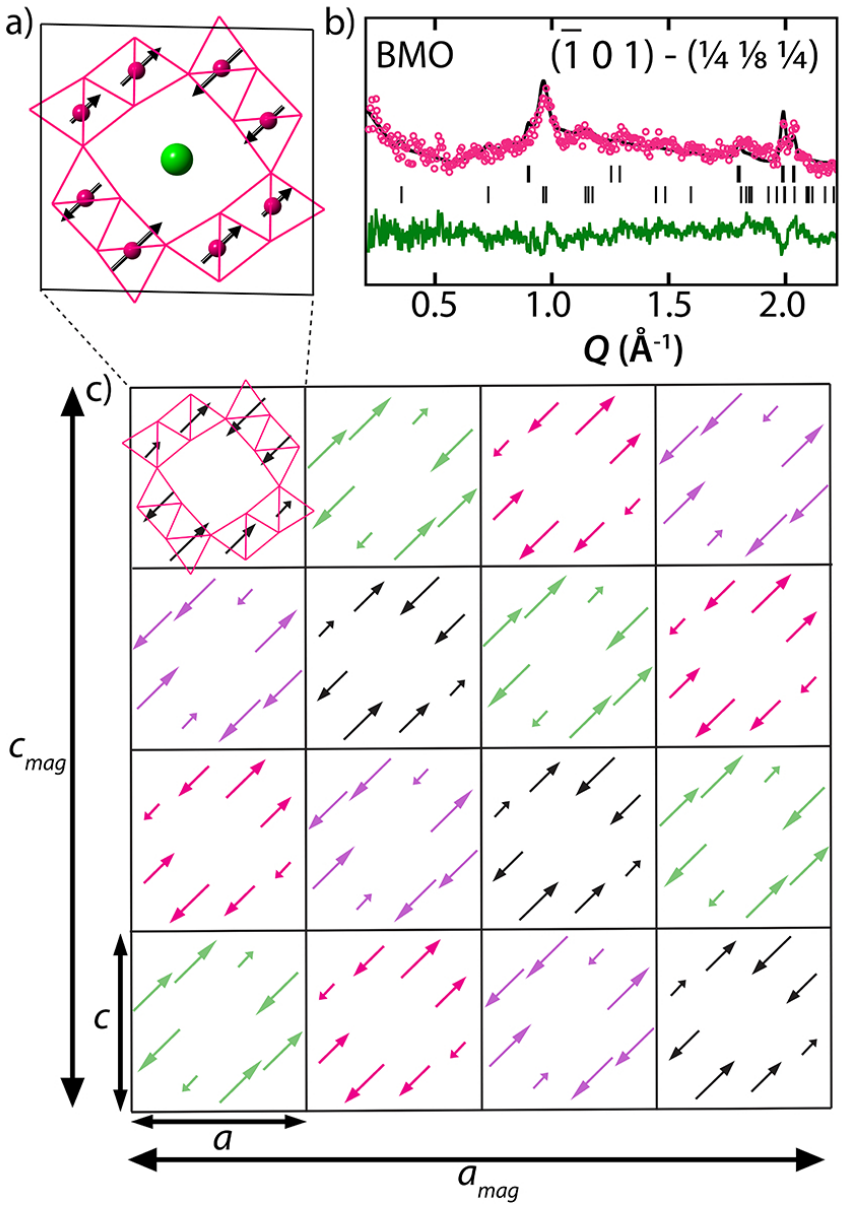

Figure 3.9: (a) One structural unit cell, with magnetic moments oriented across the cell diagonal in the ac plane. (b) Magnetic fit of constant wavelength data ($\lambda = 2.078$) for BMO, with (c) depicting the resulting complex magnetic structure. Four unique magnetic orderings occur within the structural unit cells, depicted by black, green, magenta, and purple arrows. These cells tile in a pattern such that cells along the (101) plane are identical, leading to a long-range modulated magnetic helix.

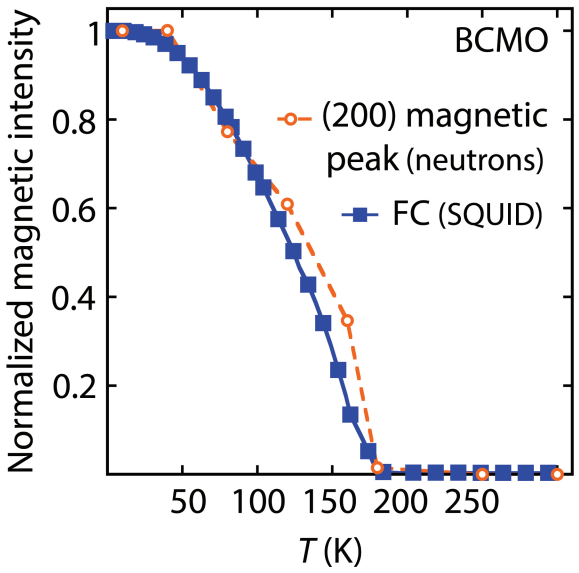

Figure 3.10: Normalized magnetic neutron peaks (orange) tracing the field-cooled susceptibility curve of BCMO (blue).

Moreover, the peak is commensurate with the chemical unit cell and indexes to the (200) peak, which is not symmetry-forbidden in space group $I2/m$ but has no contribution from the nuclear structure. The intensity of the peak decreased as the temperature approached 180 K and completely disappeared by 200 K, consistent with the magnetic transition temperature observed in the susceptibility data (Figure 3.7).

Despite resulting in only one major magnetic peak, the magnetic structure of BCMO is not trivial. For propagation vector of $\mathbf{k}$ = (0 0 0), the irreducible representations presented in Table 3.7 were obtained. Using the Reverse Monte Carlo routine in SARAh, Γ_3 gave the lowest residual.[123] Combinations of Γ_3 with other representations did not result in a lower residual. This representation leads to the moment being only in the ac-plane, as in BMO, but with antiferromagnetic coupling

between the Mn sites related by the 2-fold rotational symmetry.

Although several combinations of coefficients for the representations could be chosen to model the magnetic Bragg peaks, three models illustrate the method used for finding the most plausible magnetic structure. In Model 1, the representation Γ_3 is used to produce an antiferromagnetic ordering with the moments along the c-direction. Model 1 was ruled out since it leads to extra intensity for the (101)/(-101) doublet. Model 2 uses Γ_3 to antialign the moments along the ac-plane in order to remove intensity along the (101)/(-101) reflections but still retain some moment direction along the (200) planes. Model 2 was disqualified, however, since it leads to a large intensity for the (002) reflection. Finally, Model 3, which best fit the neutron data, uses Γ_3 but breaks the 2-fold symmetry between the Mn sites. This leads to an antiferromagnetic model, intermediate between Models 1 and 2.

The final antiferromagnetic model in Figure 3.11 illustrates several points observed in the magnetization data. The source of the uncompensated magnetization at zero-field arises from the moments on one set of (200) planes having a larger component along the c-direction than the anti-aligned moments. Since the underlying structure is antiferromagnetic, the hysteresis curve never fully saturates even at an applied field of 7 T. Most notably, the moments are ferromagnetically aligned along the tunnel direction in BCMO, whereas in BMO, the moments were antiferromagnetically aligned with the magnetic cell along the tunnel direction being eight unit cells long.

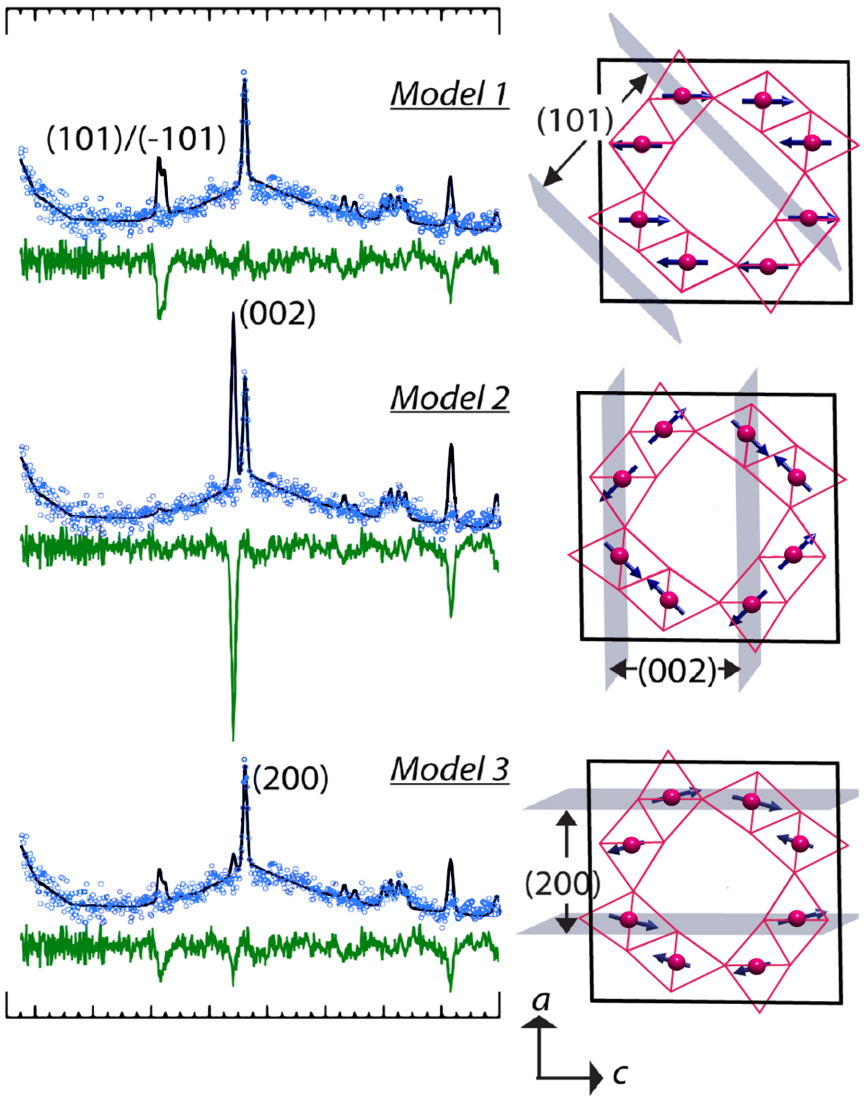

Figure 3.11: Three different models of the magnetic structure of $Ba_{1.5}Co_{0.9}Mn_{7.1}O_{16}$ and their corresponding fits to the neutron powder patterns. The neutron data were taken at the BT-1 powder diffractometer at NIST with a λ = 1.54 Å. The best refinement was achieved in Model 3, where the moments are mostly in the (200) plane with some ferrimagnetism arising from uncompensated moments for half of the metal sites.

3.3.5 Electrical properties

The resistivity of BMO was previously measured by Ishiwata et al, where they observed insulating behavior with room temperature resistivity of $\sim 3\times10^2$ Ω·cm.[104] Figure 3.12 shows the electrical resistivity measurements of pressed pellets of BCMO. An increase in resistivity upon decreasing temperature indicates insulating behavior, which is likely dominated by grain boundary effects.[125] Resistivity values obtained from pressed pellets can be two or three orders of magnitude greater than their single crystal counterparts, and as such, quantitative conclusions may be inaccurate.[140] This is especially true in materials which could exhibit anisotropic conduction as the resistivity values obtained for a pressed pellet are averaged over all crystallographic orientations.

The fit of the linear plot in the inset is consistent with variable range hopping (VRH) as the mechanism of charge mobility in the cobalt-doped sample. Efros-Shklovskii (ES) variable range hopping is expressed through the formula:

$$\rho(T) = \rho(T_0)\exp^{(T_0/T)^{\frac{1}{2}}} \tag{3.1}$$

where T_0 is a characteristic temperature. In Mott VRH, the exponent in Eq. 1 changes to $1/(1+d)$, where d is the dimensionality of the electron hopping within the system. Very little difference is seen between the one-, two-, and three-dimensional linear fits of Mott VRH, with the best fit observed for one dimension. The fit to Eq. 1 is consistent with the observations of 1D Mott VRH made by Ishiwata et al. in the pure manganese $Ba_{1.2}Mn_8O_{16}$ system.[104] However, due to the doped

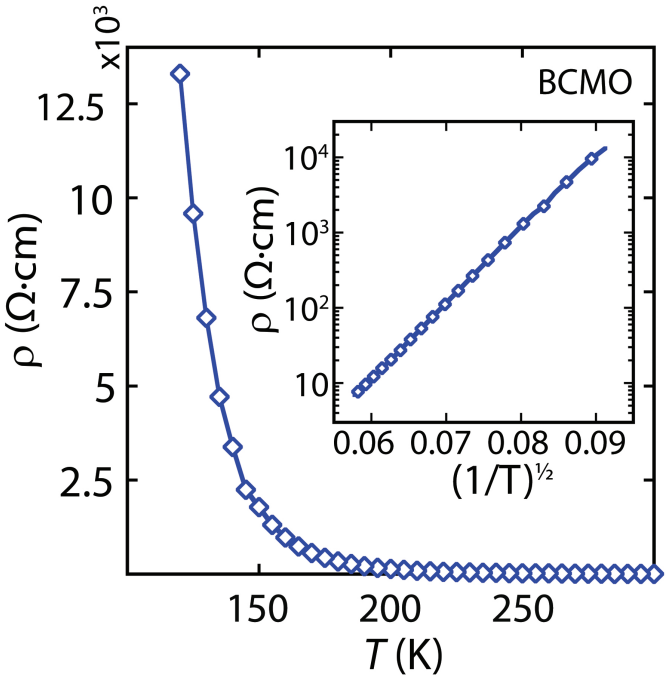

Figure 3.12: Resistivity of BCMO as a function of temperature. The insert shows linear fitting of resistance versus $T^{-1/2}$ consistent with either one-dimensional Mott or Efros-Shklovskii variable range hopping.

nature of BCMO, the ES mechanism seems more likely as Coulomb interactions of dopant atoms would create a gap in the density of states near the Fermi level at low temperatures.

3.3.6 Magnetic exchange interactions in hollandites

Predicting the magnetic ordering models in hollandites requires an understanding of the various exchange interactions between the cation centers. The recent first-principles and modeling work by Seriani et al. has examined the rich magnetic phase diagrams in hollandite-type α-MnO_2,[56,141] providing a framework from which to understand BMO and BCMO. Depending on whether the spin Hamiltonian is defined as purely Ising or Heisenberg in nature, Seriani et al. have found various helical, ferromagnetic, collinear antiferromagnetic, and glassy spin states in the phase diagram of α-MnO_2 (Figure 3.13).[56,141] The theoretical framework by Seriani et al. therefore points to the possible magnetic functional behavior of Mn-based hollandites that is just beginning to be explored experimentally.

Table 3.2: Structural parameters for $Ba_xMn_8O_{16}$ and $Ba_xCo_yMn_{8-y}O_{16}$ from TOF neutron diffraction refinements at 300 K. Standard uncertainties are given in parentheses.

			$Ba_{1.14}Mn_8O_{16}$ (BMO)	$Ba_{1.10}Co_yMn_{8-y}O_{16}$ (BCMO)
4g	Ba	y	0.34(2)	0.47(6)
		Occ	0.34(2)	0.47(6)
		B (Å^2)	8(1)	9(2)
4i	$M1$	x	0.170(4)	0.1663(5)
		z	0.353(3)	0.3517(5)
		**Occ	1	0.94(1)
		***B (Å^2)	0.56(6)	0.32(4)
4i	$M2$	x	0.338(1)	0.3442(5)
		z	0.843(1)	0.8410(6)
		**Occ	1	0.961(9)
4i	O1	x	0.1936(7)	0.1910(4)
		z	0.165(3)	0.1618(5)
		***B (Å^2)	0.221(9)	0.034(6)
4i	O2	x	0.1408(8)	0.1401(4)
		z	0.7998(6)	0.7924(4)
4i	O3	x	0.1822(9)	0.1839(5)
		z	0.5374(7)	0.5437(5)
4i	O4	x	0.5445(7)	0.5500(4)
		z	0.8515(7)	0.8507(5)

Table 3.3: Select interatomic distances (Å) and angles (°) in $Ba_xMn_8O_{16}$ at 300 K. Standard uncertainties are given in parentheses.

Bond length (Å)			Bond angle (°)
M1–O1	1.948(9) x2	M1–O1–M1	99.144
	1.87(1)		94.205
M1–O3	1.84(1)	M1–O4–M1	98.950
M1–O4	1.88(2)	M2–O3–M2	100.082
M2–O2	2.02(3) x2	M2–O2–M2	93.881
	1.97(2)		89.859
M2–O3	1.86(2) x2	M1–O3–M2	128.751
M2–O4	2.01(3)	M1–O4–M2	130.502

Table 3.4: Select interatomic distances (Å) and angles (°) in $Ba_xCo_yMn_{8-y}O_{16}$ at 300 K. Standard uncertainties are given in parentheses.

Bond length (Å)			Bond angle (°)
*M*1–O1	1.987(8) x2	*M*1–O1–*M*1	97.915
	1.908(7)		92.028
*M*1–O3	1.93(1)	*M*1–O4–*M*1	103.751
*M*1–O4	1.817(7)	*M*2–O3–*M*2	101.044
*M*2–O2	1.958(8) x2	*M*2–O2–*M*2	93.775
	2.04(1)		95.875
*M*2–O3	1.852(9) x2	*M*1–O3–*M*2	127.132
*M*2–O4	1.99(1)	*M*1–O4–*M*2	128.088

Table 3.5: Composition Analyses of BMO and BCMO.* Standard uncertainties are given in parentheses.

Sample	BMO		BCMO		
	Ba	Mn	Ba	Co	Mn
neutron	1.14(6)	8	1.09(9)	0.40(9)	7.60(9)
XRD	1.22(1)	8	1.27(2)		
ICP-MS	1.6(3)	8	1.47(5)	0.91(4)	7.09(4)
XPS	1.5(1)	8.0(4)	1.4(1)	0.79(5)	7.2(5)

*Values indicate the molar ratios determined by the given method

Table 3.6: Curie-Weiss parameters extracted from the high temperature paramagnetic regions of $1/\chi$ plots (Figure 3.7).

Sample	T_N (K)	θ_{CW} (K)	C (cm^3 K mol^{-1}	$\mu_{eff}(\mu_B)$
BMO (as prepared)	~25	-430	2.34	4.34
BMO (HCl washed)	~25	-335	2.03	4.05
BCMO (as prepared)	~180	-630	2.67	4.64
BCMO (HCl washed)	~180	-499	2.46	4.45

Table 3.7: Basis functions allowed for the given propagation vector **k** for compounds $Ba_{1.2}Mn_8O_{16}$ and $Ba_{1.2}Co_xMn_{8-x}O_{16}$*

	Irreducible representation	Basis functions
BMO	Γ_1	$M1_a$:(1,0,0);(0,1,0);(0,0,1)
		$M1_b$:(1,0,0);(0,1,0);(0,0,1)
		$M2_a$:(1,0,0);(0,1,0);(0,0,1)
		$M2_b$:(1,0,0);(0,1,0);(0,0,1)
BCMO	Γ_1	$M1,2$:(0,1,0)
		$M1,2+-x,y,-z$: (0,1,0)
	Γ_2	$M1,2$:(1,0,0);(0,0,1)
		$M1,2+-x,y,-z$:(1,0,0);(0,0,1)
	Γ_3	$M1,2$:(1,0,0);(0,0,1)
		$M1,2+-x,y,-z$:(-1,0,0);(0,0,-1)
	Γ_4	$M1,2$:(0,1,0)
		$M1,2+-x,y,-z$:(0,-1,0)

*The functions for the different M-cation sites correspond to the magnetic moment directions. In both BMO and BCMO, we conducted the magnetic structure refinements with space group $I-1$.

[a,b]Differentiates the two orbits of the $M1$ and $M2$ sites, which are related by the $2/m$ operation.

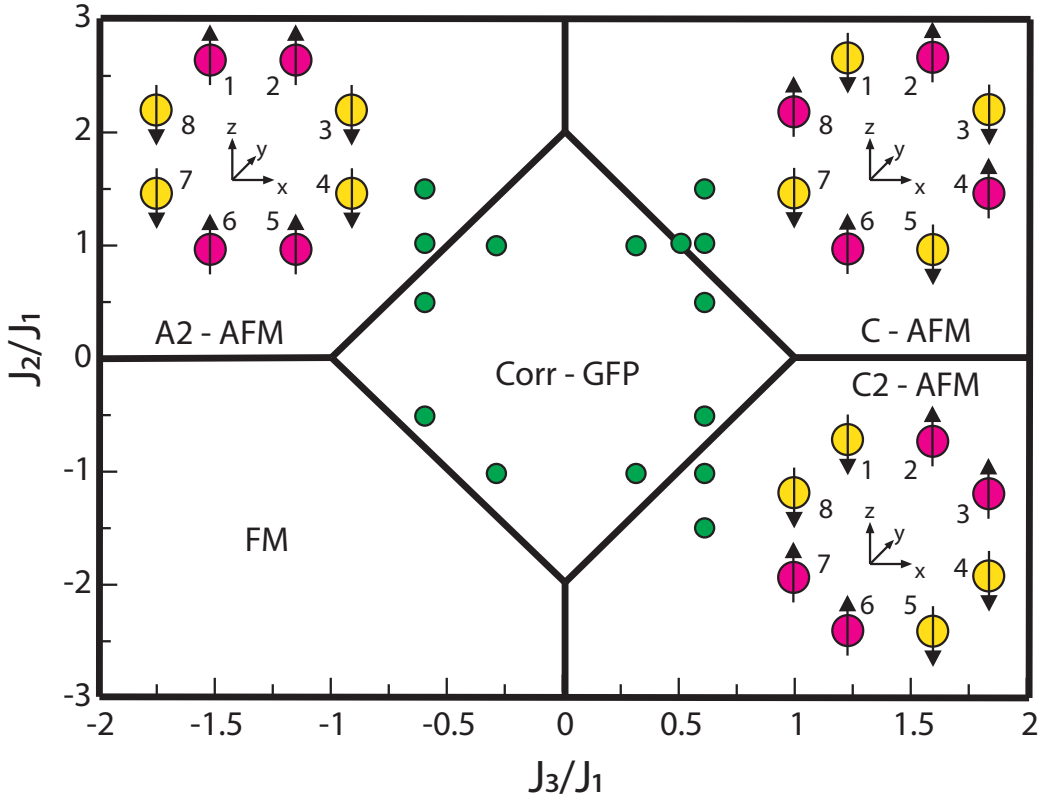

Figure 3.13: Phase diagram of the Hamiltonian for $J_1 > 0$, as outlined in the theoretical studies of Seriani et al.[56,141] Five different phases are observed: three AFM (C-AFM, $A2$-AFM, $C2$-AFM), one FM, and one geometrically frustrated (corr-GFP) with perfect anticorrelation along the y axes. Also geometrically frustrated phases with zero area are found at every boundary between any of the five phases. Green circles represent the points in the phase diagram probed via the Monte Carlo simulations.

Given the localized and insulating electronic behavior in BMO and BCMO, we expect superexchange interactions between the cations to dominate the magnetic behavior. Using the J_i notation and models of α-MnO_2 by Seriani et al, the possible exchange parameters in the BMO and BCMO structures, can be described.[56,141] Figure 3.14 shows the three nearest neighbor exchange interactions arising from the triangular topology of the Mn-sublattice. Along the tunnel direction is J_1, while J_2 and J_3 act around the tunnel walls. Crystallographic data shows that J_1 occurs for the shortest M–M distance in BMO and through the smallest M–O–M bond angle (89.9° to 99.1°). The M–M distances and M–O–M bond angles are subsequently larger for J_2 and J_3. Notably, J_3 couples the two different $M1$ and $M2$ sites in BMO, whereas J_1 and J_2 link the same site within the octahedral dimer chain.

According to the Goodenough–Kanamori rules,[116–118] the superexchange mechanism favors strong, antiferromagnetic interactions when the M–O–M bond angle is 180°. The covalent nature of the orbital overlap between the d-orbitals directed toward the same oxygen p-orbital leads to antiferromagnetic coupling between nearest neighbor cations. When the M–O–M bond angle is 90°, the same d-orbitals in the metal cations interact with orthogonal oxygen p-orbitals, which causes the interaction to be dominated by a Coulombic term that favors a weak, ferromagnetic coupling. In the hollandites presented here, the M–O–M bond angles range from ~90° to 130°, which makes the assignment of the exchange constants difficult. Unlike in the perovskite manganites, the O^{2-} anions in hollandites coordinate to three metal centers, where half of the oxygen sites are in a trigonal pyramidal geometry, while the other half in trigonal planar. Crespo and Seriani

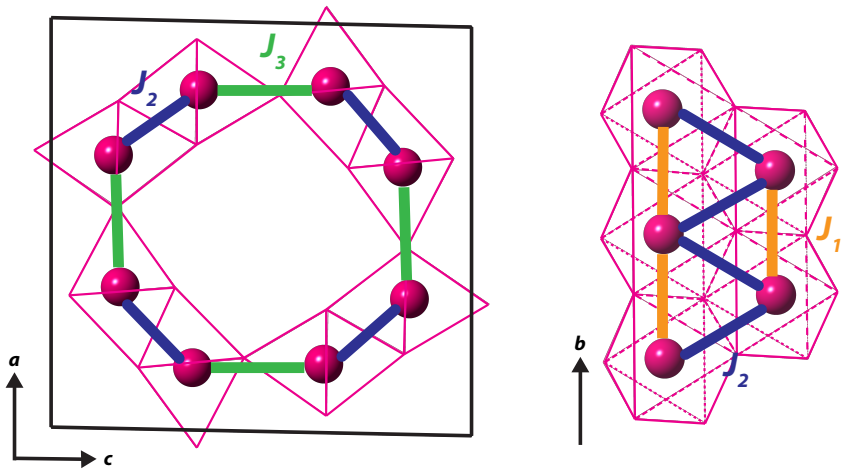

Figure 3.14: Schematic of the three magnetic exchange parameters, J_i, to model the magnetic behavior in BMO and BCMO. This $J_1 - J_2 - J_3$ model is derived from the theoretical work of Seriani et al.[56,141]

therefore formulated the intermediating orbitals controlling the superexchange as the sp^3 hybrid, sp^2 hybrid, and p_z-orbitals.[56] The sp^3 hybrid is thought to favor ferromagnetic interactions, and the sp^2 and p_z-orbitals can change from antiferromagnetic to ferromagnetic depending on the contribution from the p_z-orbital in hybridizing with the Mn d-orbitals.

The subsequent models from applying these exchange constants led Seriani et al. to find four collinear models: three antiferromagnetic and one ferromagnetic,[56,141] and they constructed a phase diagram plotting J_2/J_1 vs J_3/J_1 (Figure 3.13). In an Ising system when J_2 and J_3 are smaller than J_1, a spin glass state is formed. In a Heisenberg system when J_2 and J_3 are smaller than J_1, as is likely for Mn^{4+}, various helical states are found. Unfortunately, none of the collinear antiferromagnetic models proposed by Seriani et al. fit the neutron data for BCMO.

This discrepancy may arise from the chemical composition and structural differences between BCMO and α-MnO_2. Nevertheless, the model proposed in Figure 3.11 is closely related to their antiferromagnetic models with moments along the c-direction as well. However, the $J_1 - J_2 - J_3$ model does explain how Co-substitution could change the ordering in BMO. For BMO, the size of J_2 and J_3 would have to be sufficiently small with respect to J_1 to lead to helical ordering. The addition of the Co^{2+} cation could tune the system from Heisenberg to Ising-like due to its large single-ion magnetic anisotropy,[137] thereby unraveling the helical ordering. In addition, the Co^{2+} cations could increase the strength of either J_2 or J_3 sufficiently to promote a collinear state. The structural details from the neutron data do not reveal any obvious changes between BMO and BCMO, so the tuning of the exchange parameters implies an electronic effect rather than a structural one.

3.4 Conclusions

The combination of ferrimagnetism with insulating properties is rare as ferromagnetic coupling often involves itinerant electrons. Insulating materials, on the other hand, typically feature localized electrons. Several strategies have been pursued to find magnetic insulators in transition metal oxides,[142–144] especially in perovskite materials.[145,146] The hollandites represent a new avenue for ferromagnetic insulators, with the study by Hasegawa et al. representing the first observation of this phenomenon for hollandites. The high-pressure phase $K_2Cr_8O_{16}$ displayed ferromagnetic half-metal behavior with T_C = 180 K and T_{MIT} at 95 K.[54] Computa-

tional studies on the $K_2Cr_8O_{16}$ material suggest two conflicting models to account for the ferromagnetic insulating properties: Mahadevan et al. suggest the properties arise from charge-ordering within the framework, induced by electrons from the donor tunnel cations,[55] whereas Toriyama et al. attribute the metal-insulator transition (T_{MIT}) to a Peierls instability in the quasi-one-dimensional structure along the CrO_6 zigzag chains.[147] Sugiyama et al. lend credence to Toriyama's proposed mechanism in their reports of muon-spin rotation and relaxation data that suggest the absence of charge ordering in $K_2Cr_8O_{16}$ at T_{MIT}.[78] Deintercalation of potassium from the $K_2Cr_8O_{16}$ framework increased the T_C of the material to 250 K, but no report has been given on resulting electronic properties.[77] Similarly, the high-pressure phase $Rb_2Cr_8O_{16}$ was reported to be ferromagnetic with a T_C = 295 K and semiconducting behavior below 290 K, though this material has only been minimally investigated.[67,78]

Mn-based hollandites represent a route towards magnetic insulators without the need for high-pressure synthesis. Comparison of these results for BCMO with those of other hollandites is shown in Table 3.8. In $K_{1.5}Mn_8O_{16}$, Sato et al. reported an increase of susceptibility (χ) upon cooling from 52 K to 20 K, although the susceptibility did not feature any saturation; rather, it peaked at 23 K, then displayed a decrease in susceptibility, characteristic of antiferromagnetic ordering.[64,139] Magnetic hysteresis measurements of $K_{1.5}Mn_8O_{16}$ at 30 K also failed to saturate, similar to the measurement of BCMO (Figure 3.8). The magnetic behavior of $K_{1.5}Mn_8O_{16}$ looks to be closely related to the pure manganese sample, BMO. The hysteresis observed by Sato et al appears to have been measured in the

Table 3.8: Comparison of magnetic properties in reported ferromagnetic insulating hollandites.

Composition	T_C (K)	Coercivity (T = x K)
$K_2Mn_8O_{16}$	180	« 0.25 T (5 K)
$Rb_2Cr_8O_{16}$	295	–
$K_{1.5}(H_3O)_xMn_8O_{16}$	52	0.4 T (30 K)
BCMO	180	1 T (2 K)

small susceptibility hump observed in the transition between paramagnetic and antiferromagnetic behaviors. To date, literature searches have not uncovered any other hollandite materials with this unusual combination of properties.

Complex helical ordering has been proposed as the magnetic structure of pure manganese-based hollandites $K_{1.5}Mn_8O_{16}$, and $Ba_{1.2}Mn_8O_{16}$.[64,104,139] This study has provided the first magnetic structure refinement of this material from neutron diffraction. The expansion and modulation of the magnetic moments relative to the atomic unit cell support the complex helices that have previously been suggested. The complex helix could represent a way to lift the frustration in the triangular lattice, as evidenced by the high frustration index seen in the BMO magnetization measurements.

By simply substituting enough Mn-sites with Co^{2+}, the magnetic ordering of BMO was tuned from a complex helix to a ferrimagnetic material with a much higher ordering temperature of 180 K. This ferrimagnetic response could now rep-

resent another mechanism for relieving the inherently frustrated lattice.

The combination of ferrimagnetic and insulating properties suggests that BCMO and future related hollandite materials may have potential use in multifunctional applications such as spintronics. The potential to tune T_C to higher temperatures (as seen in $K_2Cr_8O_{16}$ and $K_2V_8O_{16}$) is especially promising, as future device applications will require functionality near or above room temperature. Furthermore, $K_2Cr_8O_{16}$ and $RbCr_8O_{16}$ require high-pressure preparation,[67,78] whereas Mn-based hollandites represent a platform for synthesizing magnetic insulators at ambient pressure. A recent study of $BaMn_3Ti_4O_{14.25}$ with the hollandite framework also confirms the possibility of developing these materials for multiferroic applications.[87] Finally, the microporous nature of hollandite materials further provides interesting possibilities in terms of chemical control of physical applications through soft chemical techniques. Mn-based hollandites are good candidates for exploring the possibility of magnetic semiconductors, an important set of materials for spintronic applications.

Chapter 4: $K_{1.6}Mn_8O_{16}$

4.1 Introduction

The Mn-based hollandite with K^+ in the tunnels has been studied by many groups, and is the most-studied manganese hollandite. Synthetic routes to obtain $K_{1.6}Mn_8O_{16}$ include hydrothermal,[64,89,93,99,101,125,139,148–154] redox,[84,92,95,100,155–161] reflux,[41,90,96,162] electrolysis,[166–168] sol-gel,[83,160,163,164] microwave,[91] solid state/flux reactions,[105] and high-pressure reactions.[165] Of these techniques, most of the resulting reported samples display low crystallinity.

Of all the published work regarding $K_xMn_8O_{16}$, only a few reports have investigated the magnetic and transport properties of $K_xMn_8O_{16}$, and discrepancies exist between the properties of samples obtained by wet method and those by dry techniques. One likely contributing factor to the observed differences is the probable addition of guest ions in hydrothermally synthesized microporous materials, as wet methods often leave H_3O^+ or other species inside the tunnels.[167] No reports exist on the magnetic structure of $K_{1.6}Mn_8O_{16}$, and only Sato et al comment on the susceptibility of a polycrystalline sample.[64]

Since manganese has a variety of oxidation states ranging from 0 to +7, solid compounds of manganese have a flexibility for charge transfer without a large

degradation of the crystal structure. From a physical point of view, the redox property of manganese oxides is often related to their high electrical conductivity. In addition, a manganese ion has a magnetic moment dependent on its valence ($S = \frac{5}{2}$, 2, and $\frac{3}{2}$ for Mn^{2+}, Mn^{3+}, and Mn^{4+}, respectively). Therefore, it seems very attractive to investigate the effects of the chemical modifications (ion exchange, oxidation and reduction, etc.) on the physical properties (conductivity and magnetism, etc.).

Literature accounts of the $K_xMn_8O_{16}$ hollandite have reported both monoclinic[99] and tetragonal[167] settings for the crystallographic space group. The $K_{1.5}Mn_8O_{16}$ hollandite had been studied by Sato et al, who used a high temperature synthesis to produce a polycrystalline sample.[64]

Single crystals were reportedly obtained via hydrothermal synthesis using a test-tube autoclave. The referenced synthetic procedure involved 200 mg of γ-MnOOH and 0.15 cc of KOH charged into a gold ampule, which was subsequently sealed by welding and inserted into an autoclave.[99] The autoclave was heated to 650° C at a rate of 400 K/hr, kept at the reaction temperature for a week, then quenched to room temperature, producing monoclinic crystals. Sato et al do not discuss the crystal symmetry of their materials, but mention that crystals were typically sized at $1 \times 0.005 \times 0.005$ mm^3. Electrical conductivities were measured by the dc four-terminal method. Gold wires were attached to a single crystal with carbon paste and the current was applied along the needle axis (the c-axis), which is parallel to the tunnels. Magnetic measurements were done on a bundle of single crystals. Unfortunately, all the batches included some non-crystalline impurity in addition to needle-like KMO crystals.[64]

Mn-based hollandites represent a route towards magnetic insulators without the need for high-pressure synthesis. In $K_{1.5}Mn_8O_{16}$, Sato et al reported an increase of susceptibility (χ) upon cooling from 52 K to 20 K, although the susceptibility did not feature any saturation; rather, it peaked at 23 K, then displayed a decrease in susceptibility, characteristic of antiferromagnetic ordering. Magnetic hysteresis measurements of $K_{1.5}Mn_8O_{16}$ at 30 K also failed to saturate. We believe that the hysteresis observed by Sato et al in $K_{1.5}Mn_8O_{16}$ was measured in the small susceptibility hump observed in the transition between paramagnetic and antiferromagnetic behaviors.

The symmetry of hollandite compounds depends on the ratio of the average ionic radius of the octahedral cations to that of the tunnel cations. Structures in which this ratio is >0.48 distort, reducing the tunnel volume, and thereby lowering the symmetry from tetragonal to monoclinic. The position occupied by a tunnel cation is determined primarily by the size of the cation. Relatively small cations, such as Ba^{2+} in priderite and Pb^{2+} in hollandite, displace from the special position, 2a, to more stable sites that are at the sum of the ionic radii from the nearest O atoms. This study also indicates that the reduced form of Mn in hollandite and cryptomelane is Mn^{3+}; bond lengths calculated from the refinements suggest that Mn^{3+} is more easily accommodated in the structures than the larger Mn^{2+}.[6]

This chapter presents the work undertaken to synthesize polycrystalline $K_{1.6}Mn_8O_{16}$ under ambient pressure, and then to understand the magnetic behavior of this material through several neutron diffraction studies. X-ray diffraction (XRD), neutron powder diffraction (NPD), and magnetic property measurements have been em-

ployed to study the composition, magnetic structure and properties.

4.2 Synthesis & experimental details

$K_xMn_8O_{16}$ was synthesized by grinding Mn_2O_3 (99%, Aldrich) in a mixture of KNO_3 (≥ 99.0%) and KCl (>99%, Sigma-Aldrich) (1:2:0.25 molar ratio of Mn_2O_3 to KCl to KNO_3). The material was heated at 100 K/hr up to 1073 K, soaked for 24 h in ambient atmosphere, then cooled at 100 K/hr. The material was then re-ground and another 0.25 molar equivalent of KNO_3 was added before repeating the same heating procedure. Upon cooling the second time the material was washed thoroughly with deionized H_2O to remove KCl, then dried on a petri dish at 80° C overnight.

Room temperature powder X-ray diffraction (XRD) data was collected on a Bruker D8 X-ray diffractometer with Cu Kα radiation, λ = 1.5418 Å, (step size=0.013°, with 2θ range from 8°-140°). Constant wavelength (CW) neutron diffraction data was collected on the BT-1 high resolution powder neutron diffractometer at the NIST Center for Neutron Research, utilizing the Cu(311) monochromators, with a neutron beam of λ = 1.5403 Å. Scans were taken at 5 K, 30 K, and 100 K for $K_xMn_8O_{16}$.

Further neutron diffraction measurements were acquired with the BT-7 and NG-5 beamlines. At BT-7, measurements were taken at 3, 18, 30, 45, 60, 100, 150, 200, 250, and 300 K, with additional scans measuring the temperature dependence of the magnetic peaks between 22-29° 2θ. The BT-7 measurements utilized a py-

rolytic graphite monochromator, with d = 3.35416 Å. The neutron energy was 14.7 meV, corresponding to λ = 2.359 Å. NG-5 measurements were taken in five degree increments from 5 K up to 55 K, at a 40'40' collimation, with neutron energy of 5 meV (λ = 4.045 Å). Attempts to further separate the magnetic peak(s) at 40-42° 2θ using the 20'20' collimation (3.7 meV) were unsuccessful.

Magnetic susceptibility was measured using a magnetic property measurement system (Quantum Design MPMS). Field-cooled (FC) and zero-field-cooled (ZFC) magnetic susceptibility measurements were taken from 2 K - 300 K in direct current mode with an applied magnetic field of 0.01 T (100 Oe). Hysteresis measurements were carried out at 2 K in magnetic fields between ± 7 T.

4.3 Results

4.3.1 Crystal structure

Rietveld treatment of both the lab XRD and BT-1 NPD data showed phase pure $K_xMn_8O_{16}$. Refinements were carried out for both the $I4/m$ and $I2/m$ space groups. For the XRD refinements, final R_{wp} values of 2.504 and 2.183 were obtained for the tetragonal and monoclinic settings, respectively. The potassium stoichiometry was refined as 0.354(4) in $I4/m$, and 0.344(3) in $I2/m$, with respective crystallite sizes of ~190 nm and ~140 nm. The refined K site occupancy leads to an overall composition of $K_{1.4}Mn_8O_{16}$, with an average oxidation state of 3.83+ per manganese cation, or approximately seven Mn^{4+} cations to every one Mn^{3+} cation. Additional lattice parameters and atomic positions are detailed in Tables 4.1 and 4.2.

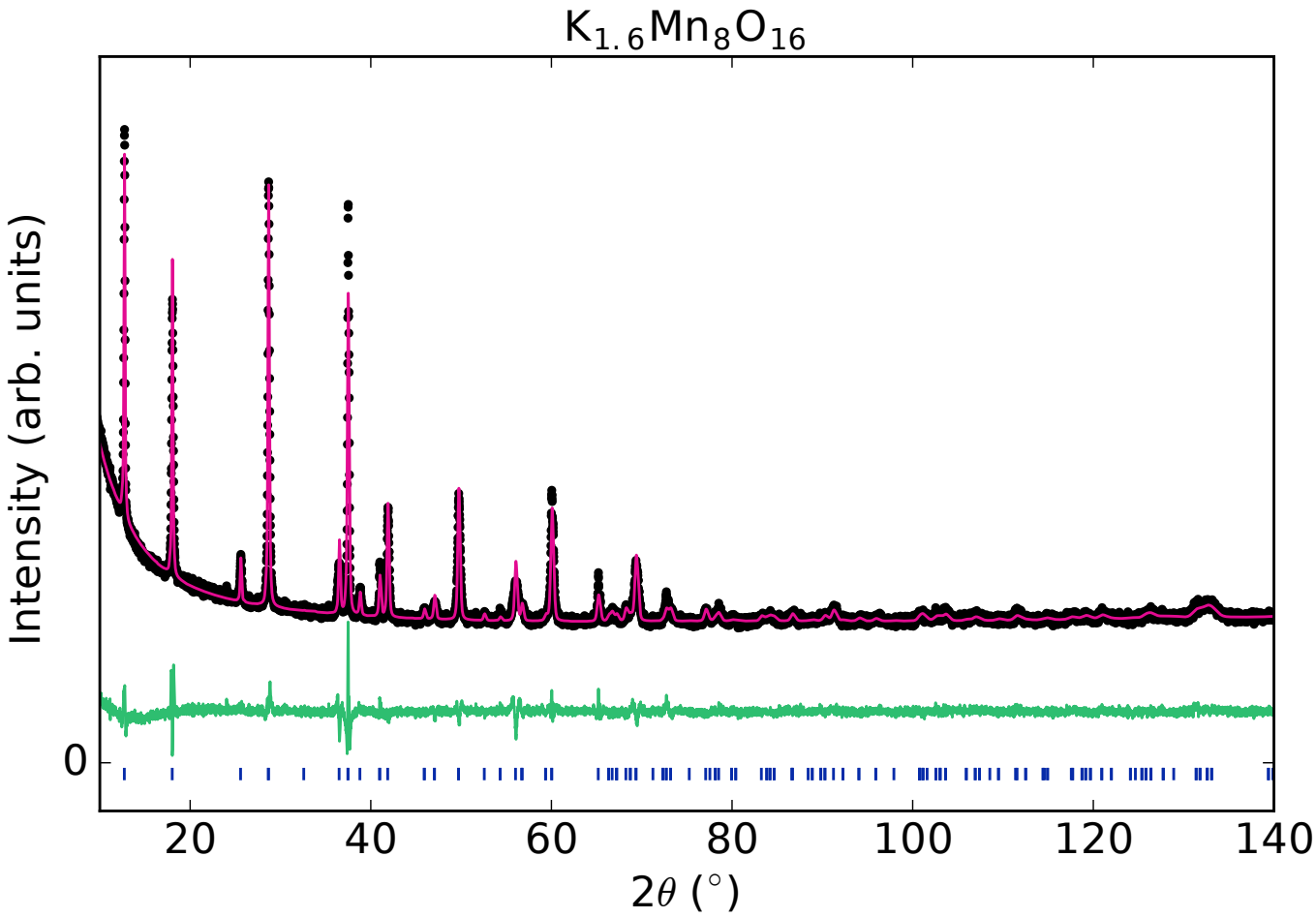

Figure 4.1: X-ray powder diffraction data (UMD) for $K_{1.6}Mn_8O_{16}$ at room temperature, with the $I4/m$ setting.

Table 4.1: $I4/m$ Structural parameters for $K_{1.35}Mn_8O_{16}$ from room temperature XRD data. Standard uncertainties are given in parentheses.

300 K, $I4/m$, R_{wp} = 2.504%, 22 independent parameters						
a = 9.8403(3) Å, c = 2.86001(7) Å, V = 276.94(2) Å^3						
atom	Site	x	y	z	U_{iso}	Occ
K	4e	0	0	0.314(4)	2.7(4)	0.354(4)
Mn	8h	0.3501(2)	0.1660(3)	0	0.92(5)	1
O1	8h	0.1544(0)	0.2030(0)	0	0.63(0)	1
O2	8h	0.5421(0)	0.1650(0)	0	0.63(0)	1

The large values for the K thermal displacement parameters are likely a result of the loose coordination environment of the K cation within the framework, allowing increased tunnel cation mobility. Previous studies of hollandite frameworks have seen incommensurate modulations of the tunnel cation, visible in electron microscopy images as sharp satellite peaks or diffuse intensity normal to the tunnel direction.[86,88,128]

Refined Mn–O bond lengths for the $I4/m$ and $I2/m$ settings are provided in Tables 4.3 and 4.4, respectively. Further evaluation of the metal-oxide bond distances determined from diffraction data allow speculation about charge ordering in $K_{1.4}Mn_8O_{16}$ for the $I2/m$ setting. As there is only one Mn site in the $I4/m$ setting, no charge ordering can be inferred from these refined values.

The average Mn–O bond lengths obtained from room temperature XRD re-

Table 4.2: $I2/m$ Structural parameters for $K_{1.35}Mn_8O_{16}$ from room temperature XRD data. Standard uncertainties are given in parentheses.

300 K, $I2/m$, R_{wp} = 2.183%, 25 independent parameters						
a = 9.8640(3) Å, b = 2.86039(6) Å, c = 9.8130(3) Å, β = 90.200(4) Å, V = 276.87 (1) Å^3						
atom	Site	x	y	z	U_{iso}	Occ
K	4e	0	0.364(4)	0	2.0(4)	0.344(3)
Mn1	4h	0.1656(3)	0	0.3535(3)	0.35(3)	1
Mn2	4h	0.3516(4)	0	0.8346(3)	0.35(3)	1
O1	4h	0.1980(0)	0	0.1520(0)	0.37(0)	1
O2	4h	0.1620(0)	0	0.7950(0)	0.37(0)	1
O3	4h	0.1610(0)	0	0.5420(0)	0.37(0)	1
O4	4h	0.5500(0)	0	0.8140(0)	0.37(0)	1

Table 4.3: Select interatomic distances (Å) and angles (°) in $K_{1.35}Mn_8O_{16}$, obtained from XRD data at 300 K ($I4/m$). Standard uncertainties are given in parentheses.

	Bond length (Å)		Bond angle (°)
M–O1	1.93(4) x2	M–O1–M	95.90
	1.96(2)		98.58
M–O2	1.886(7) x2	M–O2–M	98.60
	1.884(5)		130.35

finements of KMO are 1.920 Å and 1.911 Å for the $M1$ and $M2$ sites, respectively (Table 4.4). In a sample of pyrolusite MnO_2,[129] Mn^{4+} has been reported to have an average Mn–O bond length of ~ 1.89 Å whereas Mn^{3+} has an average Mn–O bond length of 2.04 Å.[130] Though the difference in average bond lengths in the KMO hollandite is slight, looking at the variance in bond length at each metal site supports the inference that Mn^{3+} preferentially occupies the $M1$ site, while Mn^{4+} cations predominantly occupy the $M2$ position. Using the standard bond lengths as reference, the average bond length for a site occupied 75% by Mn^{4+} and 25% by Mn^{3+} would be 1.9275 Å. These values can be further quantified using the bond valence method of Brown, Brese, and O'Keeffe[131–133] and the empirical bond valence parameter for Mn^{4+}. These calculations lead to the $M1$ site having a valence of 3.87 and the $M2$ site 3.92.

Composition analysis via Rietveld refinement of neutron powder diffraction (NPD) data showed a higher K occupancy than that obtained by XRD, correspond-

Table 4.4: Select interatomic distances (Å) and angles (°) in $K_{1.35}Mn_8O_{16}$, obtained from XRD data at 300 K ($I2/m$). Standard uncertainties are given in parentheses.

	Bond length (Å)		Bond angle (°)
$M1$–O1	1.965(9) x2	$M1$–O1–$M1$	93.42
	2.005(4)		98.02
$M1$–O3	1.85(1)	$M1$–O4–$M1$	99.86
$M1$–O4	1.87(2) x2	$M2$–O3–$M2$	99.11
$M2$–O2	1.917(3) x2	$M2$–O2–$M2$	96.49
	1.908(2)		101.57
$M2$–O3	1.88(1) x2	$M1$–O3–$M2$	130.30
$M2$–O4	1.97(3)	$M1$–O4–$M2$	125.79

ing to an overall stoichiometry of $K_{1.72}Mn_8O_{16}$ The neutron scattering lengths of K and Mn have fairly good contrast, 3.67 fm in K vs. -3.75 fm in Mn, and the absolute values of the scattering lengths are very small relative to those of O (5.803 fm).[109]

A joint Rietveld treatment of the three different temperature datasets collected at BT-1 was utilized to obtain further information about the crystal structure of $K_{1.6}Mn_8O_{16}$. Both the $I4/m$ and $I2/m$ settings were analyzed. A total of 80 independent parameters were used in refining the $K_{1.6}Mn_8O_{16}$ structure with the $I4/m$ setting across the three datasets, while 104 independent parameters were used in the $I2/m$ setting. These parameters included the lattice parameters, scale, zero error, atomic locations, peak shape, isotropic thermal displacement (for Mn and O atoms), anisotropic thermal displacement (for K), K occupancy, and a 7-order polynomial for fitting the background. With R_{wp} values of 16.240% for the $I4/m$ setting, compared to an R_{wp} of 9.802% for $I2/m$, Rietveld refinement of the BT-1 neutron data strongly suggests the $I2/m$ setting to be more accurate for $K_{1.6}Mn_8O_{16}$, though a better fit is expected due to the additional parameters of the lower symmetry setting. The refinement results for the 100 K data, as well as the diffraction patterns are given as examples for the $I4/m$ and $I2/m$ analyses in Tables 4.5 and 4.6, and Figures 4.2 and 4.3, respectively.

Table 4.5: Structural parameters for $K_{1.72}Mn_8O_{16}$ from 100 K NPD data in the $I4/m$ setting. Standard uncertainties are given in parentheses.

100 K, $I4/m$, R_{wp} = 16.240%, 80 independent parameters*						
a = 9.832(8) Å, c = 2.8563(3) Å						
atom	Site	x	y	z	U_{iso}	Occ
K	4e	0	0	0.38(2)	**	0.43(3)
Mn	8h	0.3508(6)	0.1650(7)	0	0.08(8)	1
O1	8h	0.1553(6)	0.2022(4)	0	0.38(4)	1
O2	8h	0.5426(5)	0.1669(8)	0	0.38(4)	1
	**K adp	U_{11}=U_{22}	0.03(1)	U_{33}	0.09(7)	
*Datasets collected at 10, 30, and 100 K were refined simultaneously						

Table 4.6: Structural parameters for $K_{1.72}Mn_8O_{16}$ from 100 K NPD data in the $I2/m$ setting. Standard uncertainties are given in parentheses.

100 K, $I2/m$, $R_{wp} = 9.802\%$, 104 independent parameters*						
a = 9.8767(6) Å, b = 2.88558(1) Å, c = 9.7826(6) Å, β = 90.327(4) Å,						
atom	Site	x	y	z	U_{iso}	Occ
K	4e	0	0.5(8)	0	**	0.43(2)
Mn1	4h	0.1681(7)	0	0.3448(7)	0.20(5)	1
Mn2	4h	0.3512(7)	0	0.8351(6)	0.20(5)	1
O1	4h	0.2056(5)	0	0.1524(5)	0.33(2)	1
O2	4h	0.1569(5)	0	0.8012(4)	0.33(2)	1
O3	4h	0.1588(6)	0	0.5435(4)	0.33(2)	1
O4	4h	0.5432(4)	0	0.8313(5)	0.33(2)	1
**K adp	U_{11}	0.04(1)	U_{22}	0.2(6)	U_{33}	0.05(1)
*Datasets collected at 10, 30, and 100 K were refined simultaneously						

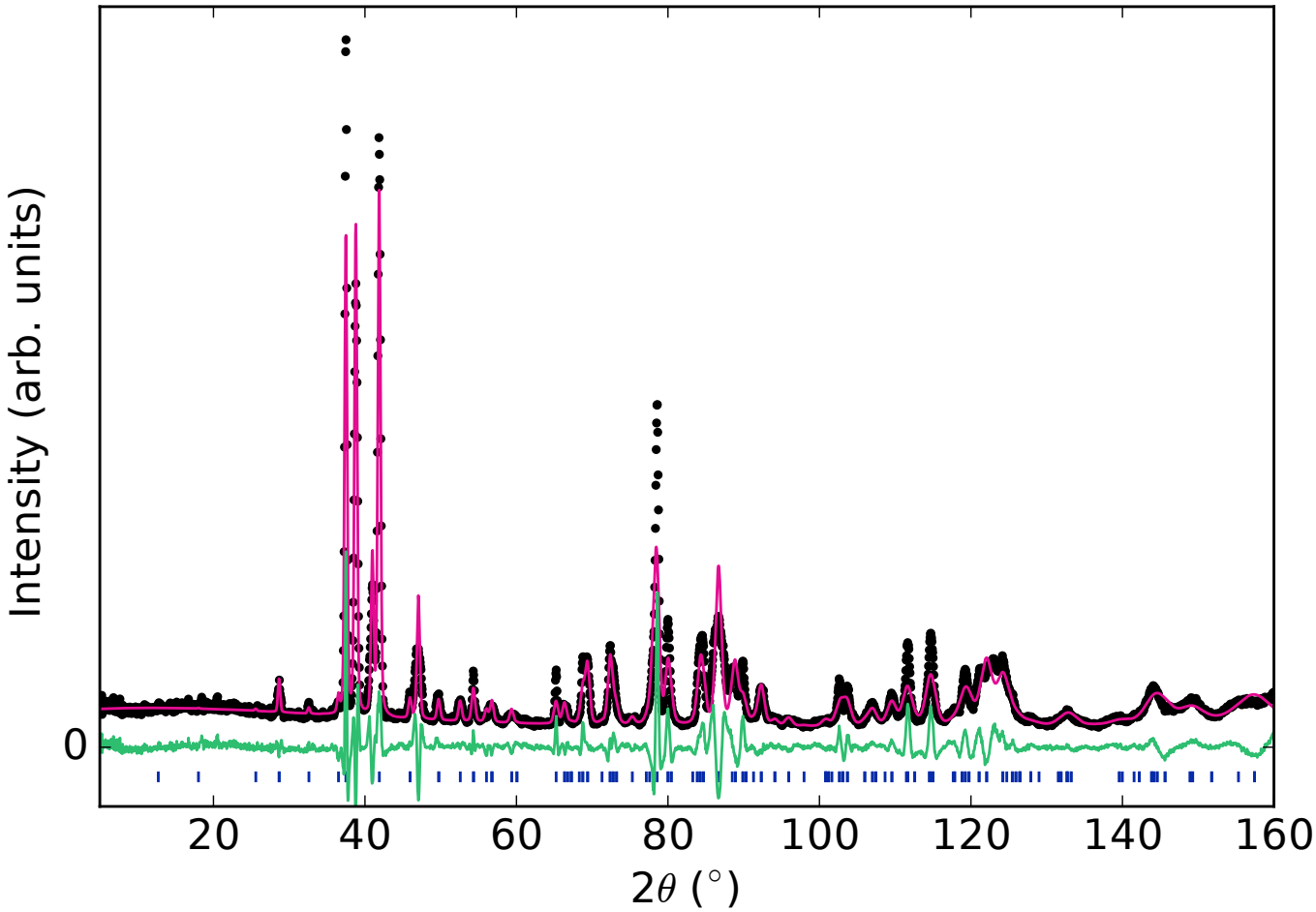

Figure 4.2: Rietveld refinement of $K_{1.7}Mn_8O_{16}$ structure in the $I4/m$ setting. Neutron powder diffraction data (NCNR) taken at 100 K is represented by black circles, the calculated fit in pink, the resulting difference is in green, and expected peak locations are indicated by tick marks below.

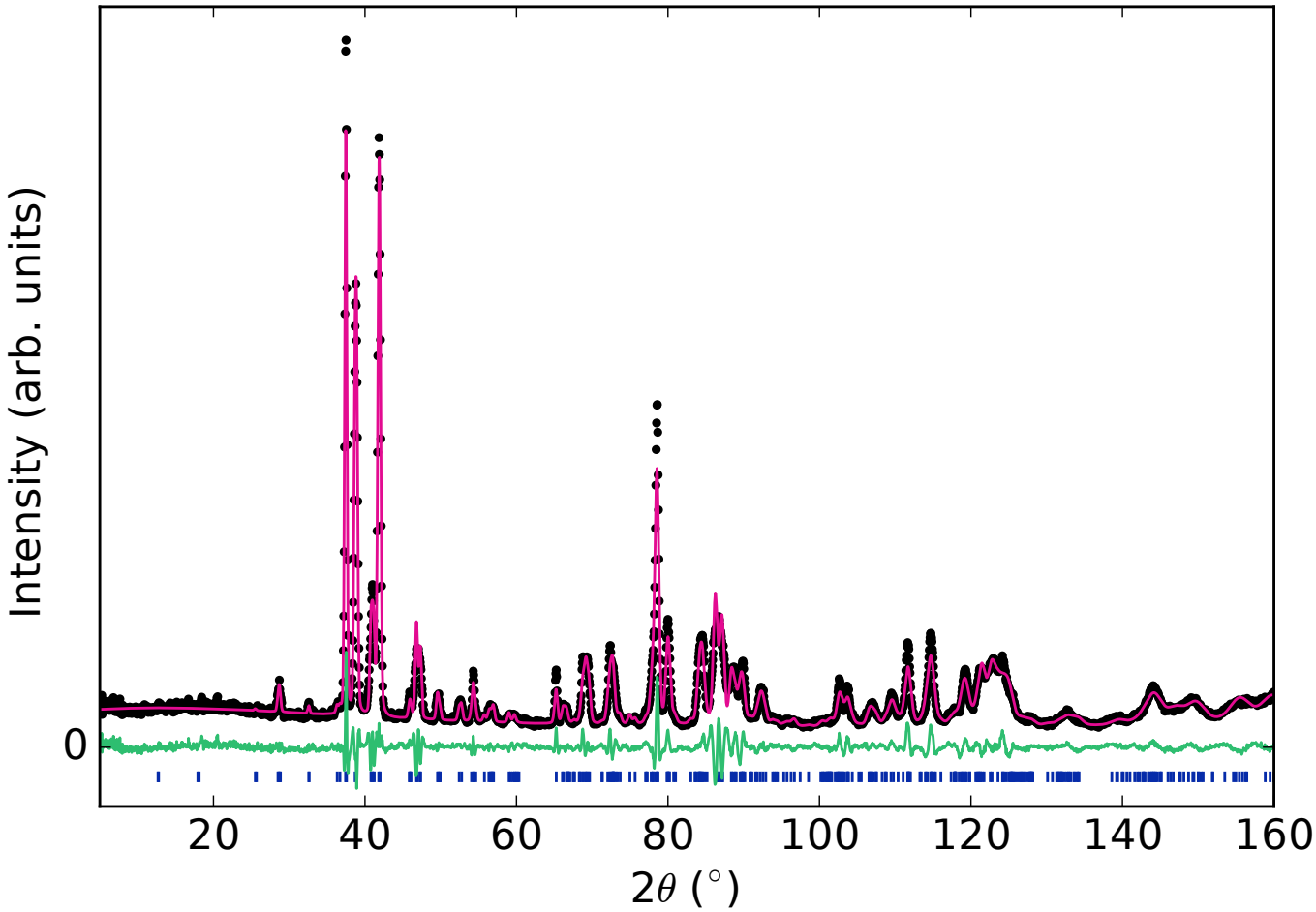

Figure 4.3: Rietveld refinement of $K_{1.7}Mn_8O_{16}$ structure in the $I2/m$ setting. Neutron powder diffraction data (NCNR) taken at 100 K is represented by black circles, the calculated fit in pink, the resulting difference is in green, and expected peak locations are indicated by tick marks below.

4.3.2 Magnetic properties

Figure 4.4 shows the magnetic susceptibility of $K_{1.35}Mn_8O_{16}$, which increases rapidly at 53 K upon cooling, followed by a sharp decrease near 26 K. This susceptibility profile is characteristic of antiferromagnetic ordering. Based off a θ_{CW} value of -425 K, the calculated Curie constant of $K_{1.35}Mn_8O_{16}$ is 2.13, with an effective magnetic moment of 4.12 μ_B. Using the refined composition of $K_{1.35}Mn_8O_{16}$ and the resulting average Mn valency of +3.83, the expected μ_{eff} of the sample is 4.047 μ_B, in fairly good agreement with the observed magnetic data.

Using the transition at 53 K as T_N, the frustration index is 8.01. Using the 26 K transition, the frustration index is 16.

Magnetization versus magnetic field measurements of $K_{1.35}Mn_8O_{16}$ show the opening of a hysteresis loop with a coercivity of ~0.5 T at 30 K. The magnetization versus field measurements taken at 2 K and 100 K appear paramagnetic or antiferromagnetic (Figure 4.5). Magnetic saturation of $K_{1.35}Mn_8O_{16}$ was not observed within the field range of the MPMS instrument.

4.3.3 Magnetic structure from neutrons

No obvious structural changes were observed across the different NPD datasets collected at BT-1. A broad hump in the background, from ~ 10-30° 2θ, suggesting significant correlations in the sample, largely obscured the 2θ range where magnetic Bragg peaks might be expected. A broad magnetic Bragg peak was observed in the diffraction pattern at ~16-18° 2θ (Figure 4.6), though the peak center appeared

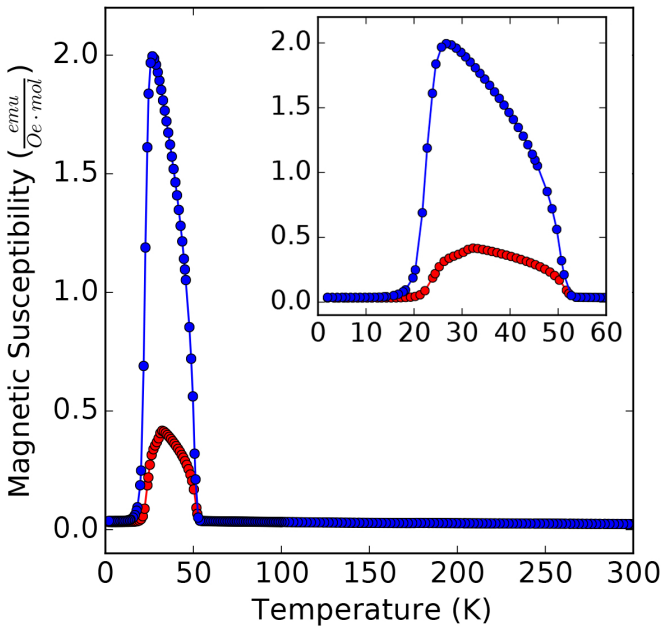

Figure 4.4: Magnetic susceptibility as a function of temperature for $K_{1.35}Mn_8O_{16}$.

to shift to slightly higher 2θ at 30 K relative to its position at base temperature. A second potential magnetic reflection was potentially observed at ~ 13° 2θ, though the low intensity of the reflection made it difficult to definitively identify the magnetic peak from background noise. This second peak sits very close to the location of the (200)/(002) pair of reflections for the $I2/m$ setting, or the (020) reflection in $I4/m$.

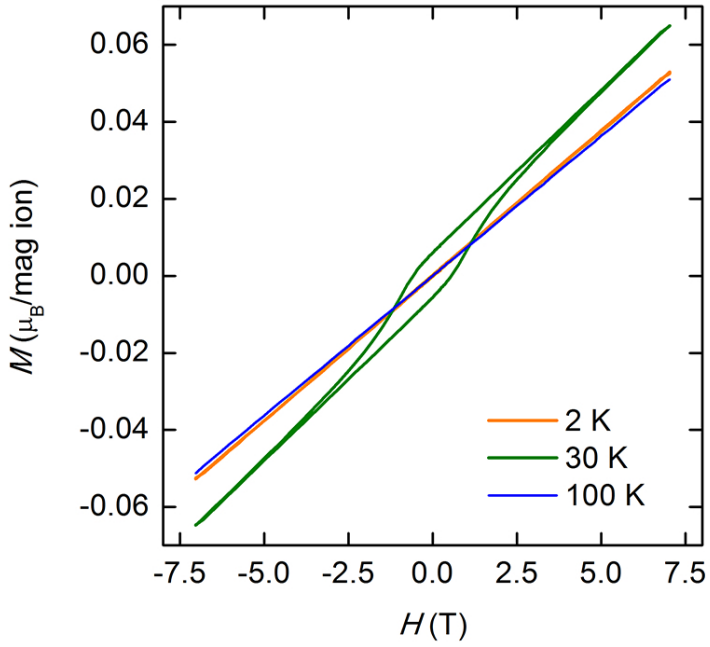

Figure 4.5: Comparison between the experimental measurements of magnetization as a function of applied field for $K_{1.35}Mn_8O_{16}$ at 2 K (orange), 30 K (green), and 100 K (blue).

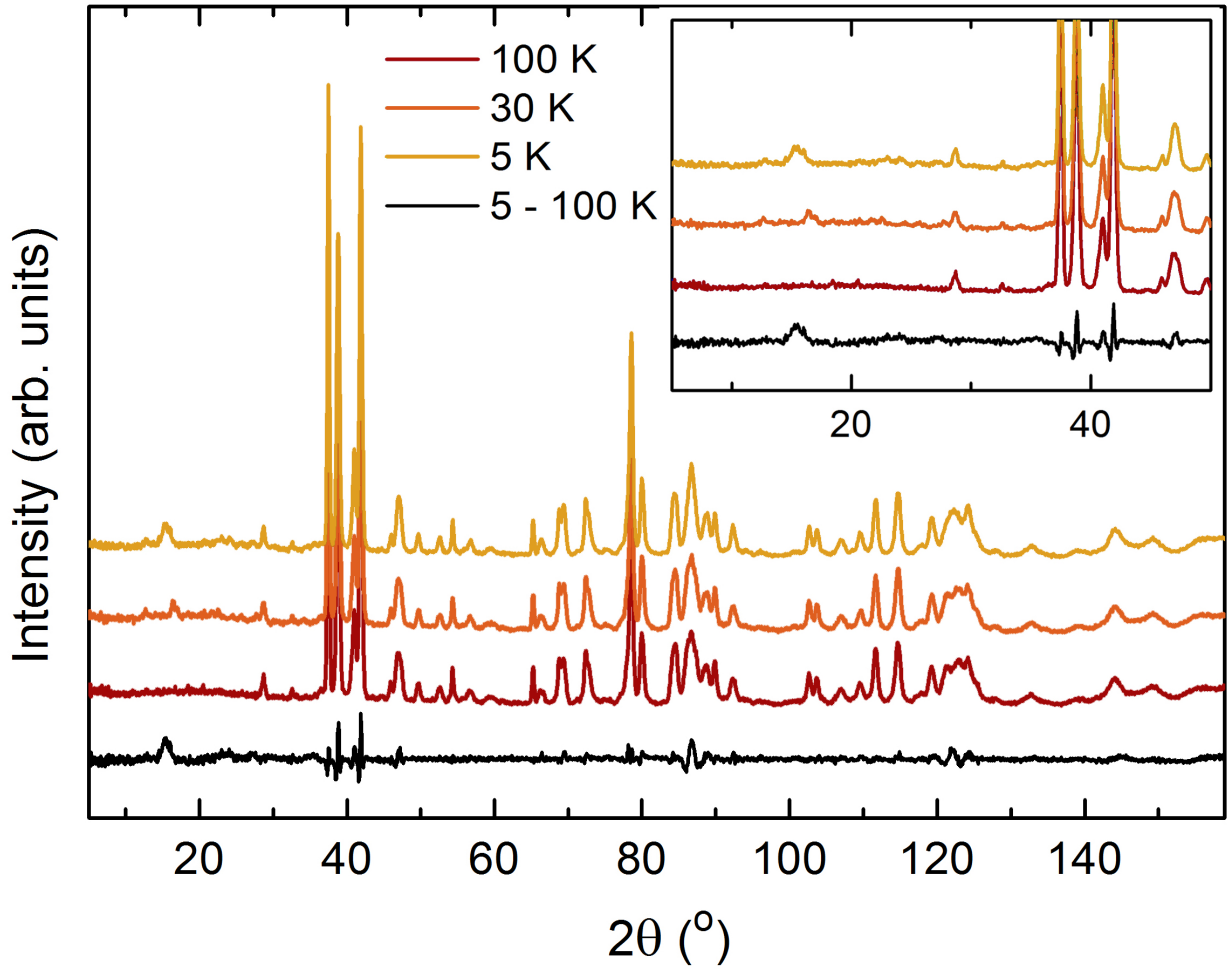

Figure 4.6: Raw neutron powder diffraction data (NCNR) for $K_{1.6}Mn_8O_{16}$ at 5 K (gold), 30 K (orange), and 100 K (maroon). Inset enhances low 2θ region where magnetic reflections can be seen around 16 2θ in the 5 K-100 K line (black).

Measurements were then taken on the BT-7 beamline, which features greater intensity at the expense of lower peak resolution. As shown in Figure 4.7, measuring as a function of temperature, the magnetic peaks with the greatest intensity (~16-18° 2θ in Figure 4.6) were observed between 23-25° 2θ. The lower resolution prevented accurate determination of the number and location of overlapping peaks, but allowed better visualization of where magnetic reflections were occurring. An abrupt shift in the location of the magnetic peaks was observed as the temperature passed through 25 K, with the most intense peaks shifting to higher 2θ as observed in the BT-1 data. A broad hump in the background indicated significant correlations in the sample.

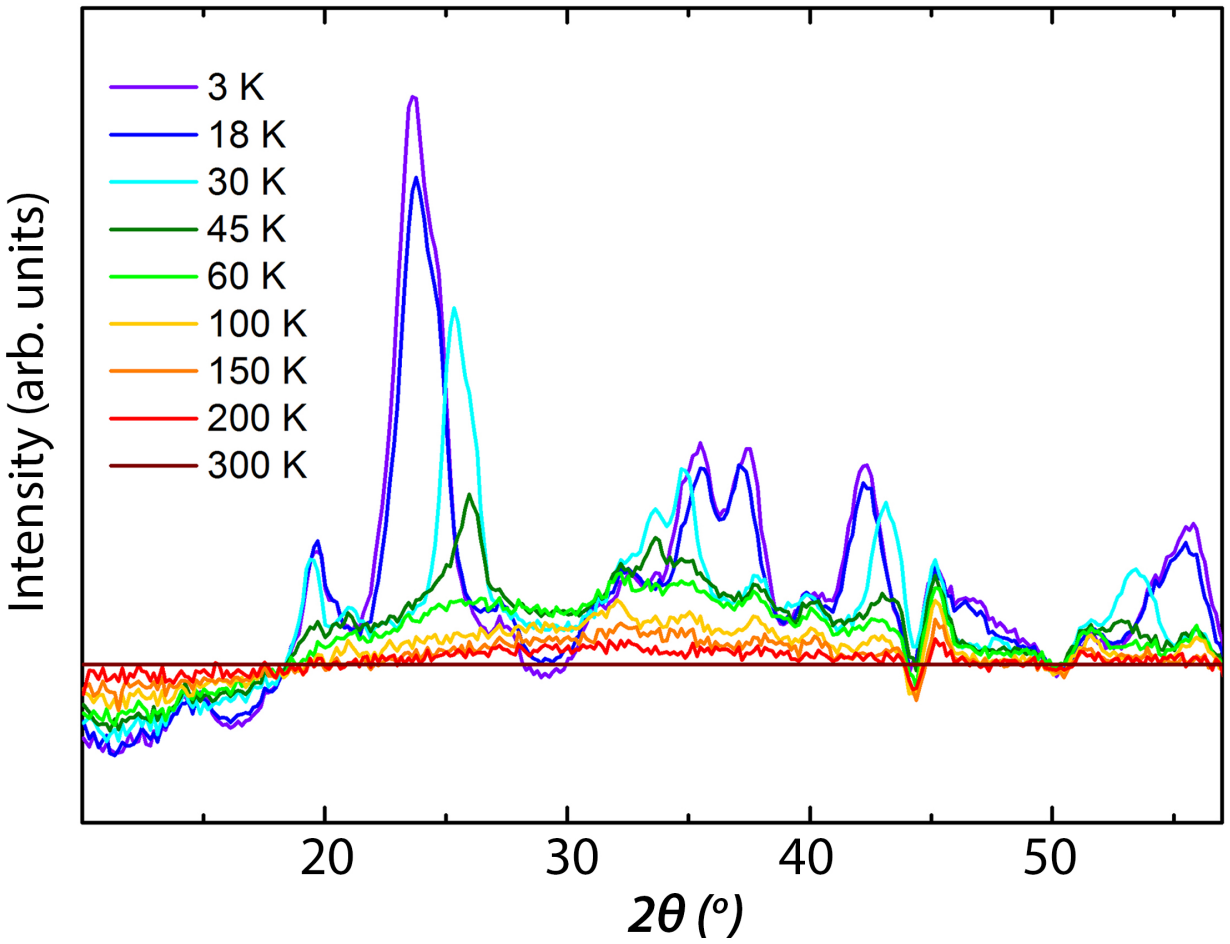

Figure 4.7: Neutron powder diffraction data (BT7, NCNR) for various temperatures of $K_{1.6}Mn_8O_{16}$ as it undergoes a magnetic transition. The data collected at room temperature has been subtracted from the intensities of each of the other datasets to isolate the temperature dependence of the magnetic reflections.

Measuring $K_{1.6}Mn_8O_{16}$ on NG-5 (SPINS), the overlapping, high-intensity magnetic peaks were resolved into a sharper peak on the right, and a broader peak on the left. The left peak is likely a result of two or more overlapping peaks, but changing the collimation settings to 20'20' on the instrument failed to further separate the broad reflection seen at ~40-42° 2θ in Figure 4.8. The shift to higher 2θ is clearly observed in the NG-5 diffraction data, with a significant decrease in intensity observed at the higher temperatures.

The shifting of magnetic peak locations suggest that upon cooling, the magnetic ordering occurs incommensurately with the nuclear structure. As temperature continues to decrease, however, the magnetic ordering suddenly locks in to a commensurate pattern around 25 K. Similar lock-in behavior was noted for the frustrated kagomé staircase in the $Co_3V_2O_8$ material.[169]

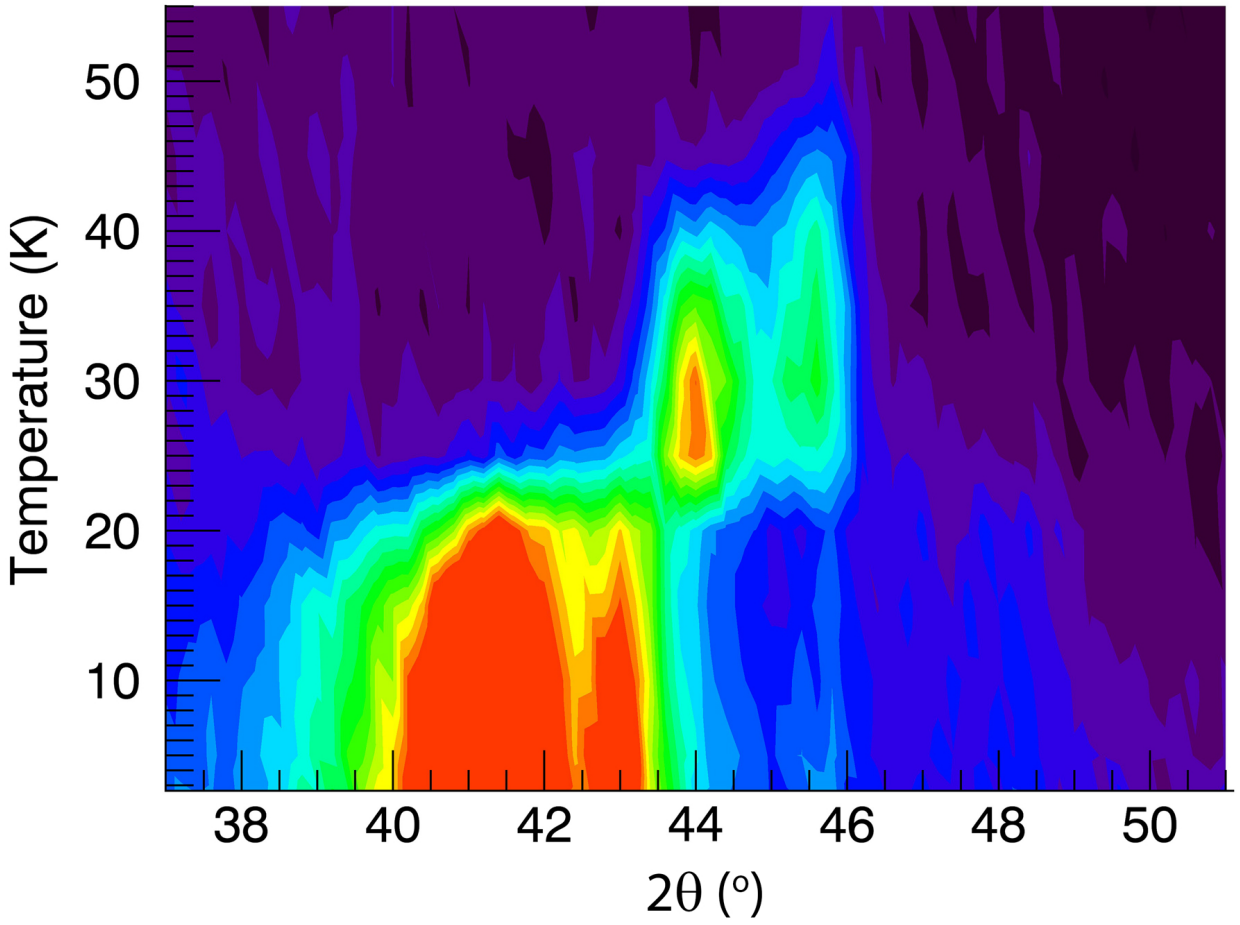

Figure 4.8: Neutron powder diffraction data (NG-5, NCNR) for $K_{1.6}Mn_8O_{16}$.

4.4 Discussion

Literature accounts of the $K_xMn_8O_{16}$ hollandite have reported both monoclinic[99] and tetragonal[167] settings for the crystallographic space group. According to Cheary's radius ratio rule, with r_A = 1.51 Å and r_B = 0.530 Å or 0.645 Å (for Mn^{4+} or Mn^{3+}, respectively), $K_{1.6}Mn_8O_{16}$ should display tetragonal symmetry.[48] The indicator proposed by Zhang et al also predicts a tetragonal setting for $K_{1.6}Mn_8O_{16}$.[49]

Attempts to grow single crystals of $K_{1.35}Mn_8O_{16}$ by flux techniques resulted in decomposition of the tunnel framework, producing denser phases and binary oxides. Strobel et al reported that heating a single crystal of $K_{1.33}Mn_8O_{16}$ above about 550° C resulted in decomposition, which is in agreement with a study on natural crystals by Faulring et al who reported a decomposition temperature of 600° C. These authors found the transformation to be 'topotactic', as the resulting Mn_2O_3 crystallites are highly oriented.[167]

Analysis of the magnetic susceptibility in $K_xMn_8O_{16}$ gave an effective magnetic moment of 4.12 μ_B and a Curie constant of 2.13, which is relatively close to the expected values of 4.05 μ_B and 2.03 calculated from the stoichiometry obtained from the refined X-ray data. The extrapolated Weiss temperature of -425 K is indicative of a high amount of frustration within the material, consistent with other materials with triangular lattice frameworks.

The magnetism of $K_{1.33}Mn_8O_{16}$ was reported to have an antiferromagnetic transition at T_N = 18 K and Curie-Weiss behavior above T_N.[167] α-MnO_2 displayed an antiferromagnetic transition at T_N = 24.5 K.[99] Magnetic susceptibility measure-

ments on $K_{1.5}Mn_8O_{16}$ revealed the existence of two magnetic phase transitions- an increase in magnetization at 52 K and an antiferromagnetic transition at 20 K.[64]

The magnetization measurements described herein showed behavior similar to that observed by Sato et al.[64] In their studies, Sato et al investigated the anisotropy of the magnetic phase transition between 52-20 K by aligning needles in grease, observing clear anisotropic behavior below 52 K. Between 52 and 20 K, their magnetization curve showed hysteresis due to a weak ferromagnetism, with the direction of spontaneous magnetization perpendicular to the *c*-axis (tunnel direction). Again, the magnetization versus magnetic field measurements obtained for $K_{1.6}Mn_8O_{16}$ at 30 K closely match the observations of Sato et al.[64]

Strobel et al observed evidence of antiferromagnetic ordering at 18 K for single crystals in their magnetic susceptibility vs. temperature measurements. This T_N value is lower than that reported in a previous paper where neither the $\chi(T)$ curve nor the sample composition were given. The discontinuity in $\chi(T)$ is much sharper for the single-crystal sample than the powder sample, with a Curie constant = 2, θ_{CW} = 315 K. An effective magnetic moment of 4.00 μ_B per Mn atom was observed for the crystal sample, in excellent agreement with the spin-only value 4.04 μ_B calculated from the formula unit $K_{0.16}MnO_2$.[167] The frustration index for this sample is f = 17.5, similar to that observed in our $K_1.35Mn_8O_{16}$ hollandite.

The spontaneous magnetization in our $K_{1.35}Mn_8O_{16}$ hollandite closely matches that of Sato et al at 30 K, displaying only about 0.3% of the calculated saturation magnetization of $K_{1.5}Mn_8O_{16}$. They proposed several possible explanations for the weak ferromagnetism, first suggesting a mechanism of double exchange. However,

citing evidence of charge order in their material, Sato et al believe the conduction electrons are considered to be rather localized at 30 K, calling in to question whether the double exchange mechanism would still effective at this temperature. Their second possibility is the so-called Dzyaloshinsky-Moriya (DM) mechanism, where the antisymmetric exchange term $D(S_1 \times S_2)$ is added to the symmetric exchange term JS_1S_2. In the tetragonal setting, a mirror plane bisects the nearest neighbor path, and the **D** vector of the DM interaction should be perpendicular to the c-axis, conflicting with the fact that the spontaneous magnetization is perpendicular to the c-axis when the easy plane is perpendicular to the c-axis. However, this discussion ignores the same charge ordering effect that the authors used to discredit their first proposal of double exchange. If charge ordering is taken into account, DM canting remains as a viable mechanism to explain the weak ferromagnetic behavior. Their third and final possibility of 'helical ferrimagnetism' accounts for the weak observed spontaneous magnetization compared to that of an ordinary ferrimagnet, also explaining the anisotropy they observed perpendicular to the c-axis of their crystal needles.[64]

In ordinary helical magnetic structures, no net magnetization appears because the magnetic moments cancel each other. However, in the case of potassium manganese hollandite there are two kinds of spins, $S = \frac{3}{2}$ for Mn^{4+} and $S = 2$ for Mn^{3+}. If the repeat period of the helical magnetic structure is completely separate and unrelated to that of the charge ordering, a cancellation of magnetic moments occurs. Conversely, if the periodicity of charge ordering is an integral multiple of the magnetic helix, complete cancellation may not always occur and weak magneti-

zation can appear. From their composition of $K_{1.5}Mn_8O_{16}$, Sato et al predicted that the period of charge ordering to be eight times as large as the unit-cell parameter along the c-axis.[64]

4.5 Conclusions

What progress have we made in understanding the crystal and magnetic structures of $K_{1.35}Mn_8O_{16}$ at low temperatures?

Our diffraction studies of $K_{1.35}Mn_8O_{16}$ do not definitively prove the structure exhibits tetragonal symmetry as seen by the poor fits obtained by Rietveld refinement of both neutron and X-ray data. Structural characterization has been undertaken using both plausible settings, though the quality of the data collected did not allow for a full solution of the magnetic structure. Temperature dependent measurements at a synchrotron would provide greater resolution of the Bragg reflections, thus resolving the symmetry debate.

Efforts to index the magnetic peaks using the K-search routine in FullProf were ultimately unsuccessful. Despite multiple attempts, using both the $I2/m$ and $I4/m$ settings and magnetic peak locations from either 30 K or 10 K, no satisfactory individual propagation vectors aligned well with all, or even several, of the magnetic peak locations. It does not seem improbable that multiple propagation vectors will be needed in solving the magnetic structure of $K_{1.35}Mn_8O_{16}$.

The broadness of the observed magnetic Bragg peaks relative to the nuclear Bragg reflections in the BT-1 data may be a result of the ordered magnetic domain

size being much smaller than the crystalline size of the nuclear structure, or may be due to the significant frustration present.[104] The 'helical ferrimagnetism' described by Sato et al is still a viable model for the magnetic ordering of $K_{1.5}Mn_8O_{16}$, similar to the ordering observed for $Ba_{1.2}Mn_8O_{16}$ in Chapter 3. Of course, one of the surest ways to expand our studies and learn significantly more about the magnetic behavior of this material would be to grow single crystals of the material, so synthetic efforts in this regard are ongoing.

Chapter 5: $Bi_{1.7}V_8O_{16}$

The research described within this chapter has been submitted for publication. Brandon Wilfong, Dr. Pouya Moetakef, Dr. Craig M. Brown, Dr. Peter Zavalij, and Dr. Efrain Rodriguez were contributing authors on the manuscript.

5.1 Introduction

Vanadium oxides are well-known to exhibit metal-to-insulator transitions (MIT) and the underlying mechanisms can involve the ordering of charge, orbital, and/or spin degrees of freedom.[170–178] A lingering question in these materials is whether Mott-type physics (*i.e.* electron-electron correlations) drive the MIT or whether Peierls-type interactions (*i.e.* electron-phonon interactions) are instead responsible.[179–182] Charge ordering also seems to be a key ingredient in observing MITs, such as in various β-vanadium bronzes and in NaV_2O_5, which undergoes charge ordering at 34 K.[171,172,174–176] The study of vanadates with various geometries affords the opportunity to better separate the parameters responsible for MITs.

V-based hollandites have been studied through both experimental and theoretical investigations, particularly because of their observed MITs combined with their quasi-one dimensional (1D) geometry. A MIT is observed at ~ 170 K for

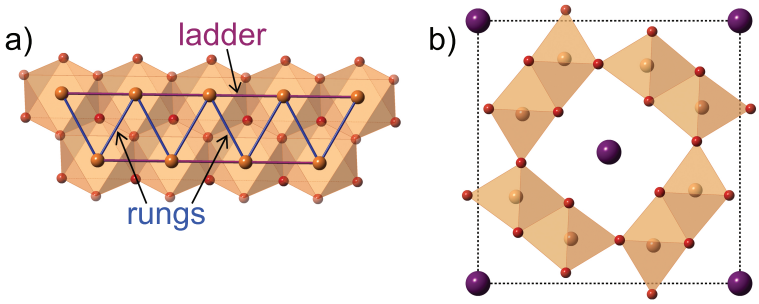

Figure 5.1: (a) Side view of the hollandite double chain showing M–M triangular connectivity of neighboring MO_6 octahedra. (b) Hollandite structure viewed down [001], showing the square channels where the A cations reside.

$K_2V_8O_{16}$. A superlattice observed in the low-temperature phase suggested the presence of charge ordering, and the authors proposed a model where half of the zigzag VO_6 chains are V^{4+}, while the other chains are a mixture of V^{3+}/V^{4+}.[69] Computational studies suggested orbital ordering pattern.[68]

Calculations predicted that changing the A cation from K^+ to Rb^+ raised the MIT up to 220 K.[70]

The higher charge of Bi^{3+} cations, as opposed to the more typical K^+ tunnel cation, lowers the V oxidation state in the hollandite framework, resulting in a unique composition of $S = 1$ and $S = \frac{1}{2}$ cations that allow such parameters to be better separated in order to shed light on similar systems.

$Bi_{1.7}V_8O_{16}$ belongs to the structural class of materials known as hollandites, where the structure can be described as a square channel occupied by Bi^{3+} cations, with walls composed of edge-sharing VO_6 octahedra (Figure 5.1b). The V cations are arranged in triangular ladders (Figure 5.1a). This topology, coupled with mixed va-

lency, can lead to interesting properties including insulating ferromagnetism,[54,55,77] frustrated magnetism,[56–58] and MITs.[59–61] The triangular ladder is known to lead to magnetic frustration such as in the hollandite $Ba_{1.2}Mn_8O_{16}$.[57]

$Bi_{1.7}V_8O_{16}$ exhibits a MIT close to 70 K, but unlike all other known vanadates that undergo MITs, the magnetic susceptibility of $Bi_{1.7}V_8O_{16}$ diverges upon entering the insulating phase.[170,173] Kato et al. first demonstrated that the divergence in the magnetization of $Bi_{1.7}V_8O_{16}$ is concomitant with the MIT near 70 K.[102] The uniqueness of this transition, however, was never investigated by structural or magnetotransport studies to explore whether the system was undergoing long-range magnetic ordering at the MIT, which would imply that Mott-type physics was playing a dominant role. Furthermore, whether or not the vanadium cations dimerize upon entering the insulating phase has been unresolved up to this point.

The studies described in this chapter aim to resolve whether the orbitally active V^{4+} and V^{3+} cations and their mixed spin states are responsible for the divergence in magnetization at the MIT and to understand how crystal structure and external magnetic field affect the transport properties. Understanding these questions would have implications on other vanadates with MITs. The combined X-ray and neutron diffraction studies along with magnetotransport and magnetization measurements reveal important details regarding the nature of the charge, orbital, and spin states in $Bi_{1.7}V_8O_{16}$.

5.2 Synthesis & experimental details

Polycrystalline samples of $Bi_{1.7}V_8O_{16}$ hollandite were produced by grinding together stoichiometric ratios of V_2O_3 (99.7%, Alfa Aesar), V_2O_5 (98+%, Sigma Aldrich), and Bi_2O_3 (99%, Fisher). Reagents were used without further purification. After grinding together, the powdered mixture was pressed into a pellet and heated to 1173 K at a rate of three degrees per minute, in an evacuated flame-sealed quartz glass ampule. Once the target temperature was reached the sample soaked for 72 hours, followed by furnace cooling.[183]

Needle-like single crystals of $Bi_{1.7}V_8O_{16}$ were grown by two different methods. One route includes using an excess of Bi_2O_3 during the solid state reaction followed by physical removal of crystals from the excess Bi_2O_3 flux. The other route includes mixing a KCl/NaCl salt mixture (1:1 molar ratio) with a pre-reacted powder mixture in an alumina crucible sealed in an evacuated quartz ampule. The product:flux molar ratio was 1:10, and the mixture was heated to 1273 K for 10 hours, followed by slow cooling at 5° /hr. Flux was removed by washing with deionized H_2O.

Synchrotron XRD was collected at the 11-BM instrument at the Advanced Photon Source with λ = 0.41397 Å from 100 K to 300 K. Constant wavelength neutron powder diffraction data was collected on the high resolution BT-1 instrument at the National Institute of Standards and Technology (NIST) Center for Neutron Research (NCNR) with a λ = 2.078 Å (Ge311 monochromator) for various temperatures between 10 K and 300 K. All powder diffraction data was analyzed using the TOPAS software.[115]

A black needle-like specimen of $Bi_{1.7}V_8O_{16}$ with approximate dimensions of 0.03 mm × 0.03 mm × 0.26 mm was used for single crystal X-ray diffraction (XRD) analysis. The X-ray intensity data were measured on a Bruker APEX-II CCD system equipped with a graphite monochromator and a Mo Kα sealed tube (λ = 0.71073 Å). Full structures were taken at 90 K, 200K, and 300K, and partial measurements for lattice constant determination were taken between 90 K and 290 K in 20 K steps. At 200 K, integration of the data using a tetragonal unit cell yielded a total of 2244 reflections to a maximum θ angle of 32.42° (0.66 Å resolution), of which 299 were independent. The structure was solved and refined using the Bruker SHELXTL Software Package.[184,185] The final anisotropic full-matrix least-squares refinement on F^2 with 27 variables converged at R_1 = 1.44% for the observed data and wR^2 = 3.70% for all data.

Field-cooled (FC) and zero-field-cooled (ZFC) magnetization measurements were taken from 2 K - 300 K with a Quantum Design magnetic property measurement system (MPMS) on a polycrystalline sample. Measurements were in direct current mode, with an applied magnetic field of 0.01 T (100 Oe). Magnetization versus field up to 7 T were also taken on the MPMS with a polycrystalline sample at 5 K. Transport measurements were taken in a Quantum Design physical property measurement system (PPMS). A four-probe geometry was used on both a sintered pellet and later on single crystals, to measure electrical resistance first upon cooling, then upon heating. For the single crystal measurements, magnetic fields were measured up to 8 T, with ramp rates of 1° /min in the temperature region of the MIT, and 5°/min above 100 K. Field was applied either along the needle direction,

$H_{\parallel}$, or normal to it, $H_{\perp}$.

5.3 Results

5.3.1 Powder diffraction

To investigate the effects of the temperature-induced MIT on the structure of $Bi_{1.72}V_8O_{16}$, we performed temperature-dependent X-ray and neutron powder diffraction (NPD). Rietveld refinements were carried out to extract structural and lattice parameters from the data. Structural and lattice parameters for representative temperatures of the NPD data are gathered in Table 5.1.

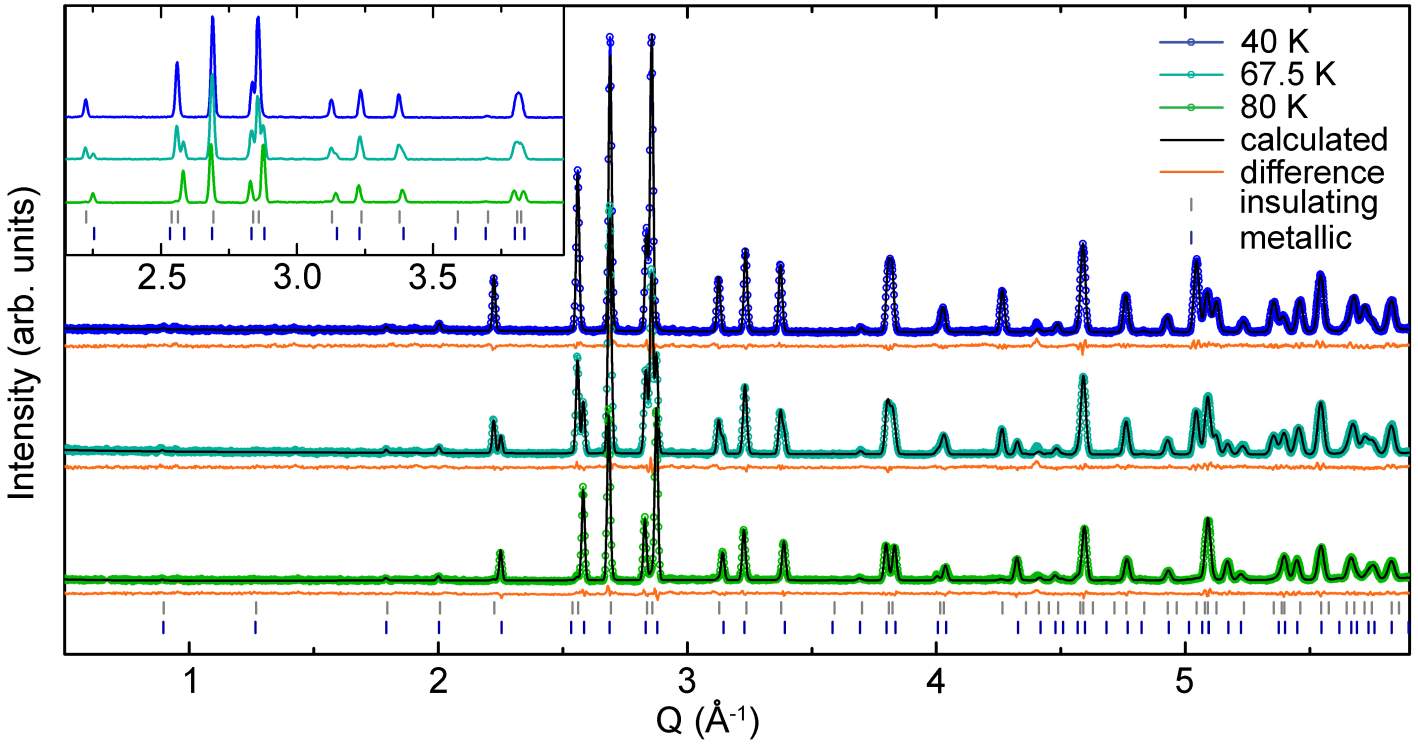

Figure 5.2: Neutron powder diffraction data (BT1, NCNR) for various temperatures of $Bi_{1.7}V_8O_{16}$ as it undergoes a tetragonal-tetragonal structural distortion during the MIT.

Temperature dependent NPD data reveals $Bi_{1.7}V_8O_{16}$ undergoing a first-order tetragonal-to-tetragonal structural phase transition. While at 10 K and 300 K, far from the MIT, the crystal structure could be fit with a single tetragonal phase, significant peak splitting was observed close to the transition. Figure 5.2 shows three NPD patterns of polycrystalline $Bi_{1.7}V_8O_{16}$ for the 40 K, 67.5 K, and 80 K temperature steps upon warming. As seen in the 67.5 K data, the NPD pattern is fit well to two tetragonal phases, with phase fractions tracking the transition from insulating to metallic behavior (Figure 5.3). A similar tetragonal-to-tetragonal transition has been observed in $Rb_2V_8O_{16}$ at its MIT of 240 K,[186] whereas the MIT in $K_2V_8O_{16}$ (155-170 K) is accompanied by a structural distortion from tetragonal to monoclinic.

The most notable structural difference between the low-T (insulating) and high-T (metallic) phases is the significant expansion in the c-direction, which runs along the triangular ladders, upon entering the insulating phase. Temperature dependence of the lattice parameters from all three different probes, neutrons, powder X-ray, and single crystal X-ray, are included in Figure 5.4. This suggests that dimerization must occur along the c-direction rather than the ab-direction, and therefore that the V–V pair formation occurs along the triangular ladder sides rather than the ladder rungs (Figure 5.1a).

Another notable result from the NPD data, is the lack of either magnetic or nuclear satellite reflections in the low-T phase. This result leads to the conclusion that no long-range magnetic order sets in during the MIT, and therefore electron-electron correlations leading to a Mott-type transition is unlikely. One must note, however, that the structure of the low-T phase may indeed be lower in symmetry

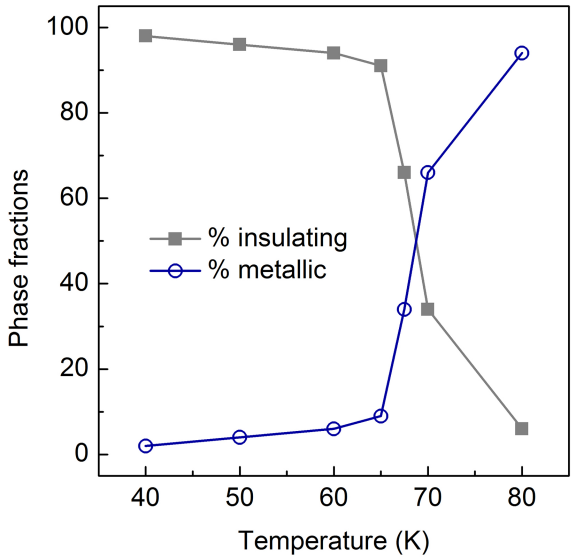

Figure 5.3: Temperature evolution of phase fractions as $Bi_{1.7}V_8O_{16}$ transitions from a metallic to an insulating phase upon cooling. Phase fractions were calculated during Rietveld refinement of neutron powder diffraction (NPD) data obtained on the BT-1 beamline at the NCNR. Error bars are smaller than plot symbols used.

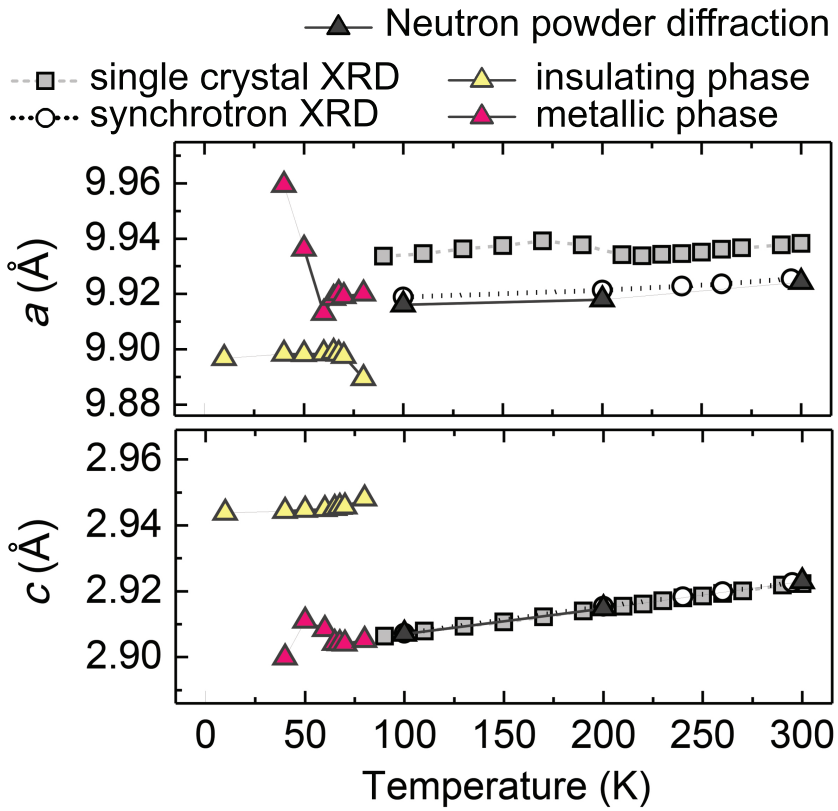

Figure 5.4: Temperature evolution of the lattice parameters for the tetragonal cell of $Bi_{1.7}V_8O_{16}$ from single crystal X-ray, synchrotron powder X-ray, and neutron powder diffraction. The low temperature data indicates a first order transition below 70 K, arising from the nucleation of a separate tetragonal phase with a large *c*-parameter. Error bars are smaller than plot symbols used.

than the tetragonal phase reported here since the NPD data cannot definitively prove this. Unfortunately, vanadium atoms do not strongly scatter neutrons, especially relative to the other elements in $Bi_{1.7}V_8O_{16}$, with neutron scattering lengths of -0.443 fm for V, compared to 8.532 fm for Bi and 5.805 fm for O.[109] The ramifications of this reality are that any satellite reflections arising from V cation displacements could be missed by the NPD measurements.

Table 5.1: Structural parameters for $Bi_{1.7}V_8O_{16}$ from NPD data taken at temperatures across the MIT. Standard uncertainties are given in parentheses.

300 K, $I4/m$, $R_{wp} = 5.521\%$						
a = 9.9243(1) Å, c = 2.92301(5) Å, V = 287.764(8) Å^3						
atom	Site	x	y	z	U_{iso}	Occ
Bi	4e	0	0	0.104(2)	1.5(1)	0.411(4)
V	8h	0.348(3)	0.173(3)	0	0.1(1)	1
O1	8h	0.1518(2)	0.1943(1)	0	0.63(3)	1
O2	8h	0.5404(1)	0.1651(3)	0	0.63(3)	1
67.5 K $I4/m$, $R_{wp} = 4.720\%$						
Metallic phase (34%)						
a = 9.9194(2) Å, c = 2.90391(9) Å, V = 285.79(2) Å^3						
atom	Site	x	y	z	U_{iso}	Occ
Bi	4e	0	0	0.110(2)	0.69(8)	0.428(2)
V	8h	0.352(6)	0.168(7)	0	0.1(1)	1
O1	8h	0.1505(4)	0.1939(4)	0	0.37(2)	1
O2	8h	0.5411(4)	0.1664(6)	0	0.37(2)	1
Insulating phase (66%)						
a = 9.8978(1) Å, c = 2.94526(6) Å, V = 288.594(9) Å^3						
atom	Site	x	y	z	U_{iso}	Occ
Bi	4e	0	0	0.102(2)	0.69(8)	0.428(2)
V	8h	0.358(3)	0.170(3)	0	0.1(1)	1
O1	8h	0.1537(2)	0.1930(2)	0	0.37(2)	1
O2	8h	0.5396(2)	0.1646(3)	0	0.37(2)	1
10 K, $I4/m$, $R_{wp} = 5.521\%$						
a = 9.8985(1) Å, c = 2.94441(4) Å, V = 288.385(9) Å^3						
atom	Site	x	y	z	B_{eq}	Occ
Bi	4e	0	0	0.099(1)	0.6(1)	0.44(4)
V	8h	0.351(3)	0.168(4)	0	0.2(2)	1
O1	8h	0.1533(1)	0.1933(2)	0	0.51(3)	1
O2	8h	0.5397(1)	0.1655(3)	0	0.51(3)	1

5.3.2 Magnetization

Unlike the hollandites $K_2V_8O_{16}$ and $Rb_2V_8O_{16}$,[69,186] the magnetic susceptibility of $Bi_{1.7}V_8O_{16}$ increases sharply at the transition temperature (T_{MI}) upon cooling (Figure 5.5a), with two steps of increasing susceptibility observed, indicative of non-spin-singlet formation in the insulating phase. Furthermore, hysteretic behavior is observed in the magnetic susceptibility with the ZFC (measured upon heating) having a slightly higher T_{MI} than the FC curve (measured upon cooling). This is consistent with the NPD data showing a large amount of phase coexistence during the first-order phase transition.

Interestingly, the susceptibility of the high-T metallic phase does not appear to be temperature independent as would be expected for a metallic Pauli paramagnet. Instead, the broad maximum near 275 K is indicative of low-dimensional magnetism associated with local moments in a 1D chain, for example. Earlier studies of $Bi_{1.7}V_8O_{16}$ showed similar broad features in the metallic state,[102,187,188] whereas the T_{MI} and extent of the susceptibility's divergence were dependent on the Bi^{3+} content and thus the charge of the V cations. This result indicates that while most electrons near the Fermi level are delocalized, some localized behavior arises possibly due to significant electron correlations even in the metallic state.

Despite the divergence of the magnetization below the MIT, $Bi_{1.7}V_8O_{16}$ never enters a ferromagnetic state. While it appears it could be diverging much in the same way as an antiferromagnet above the Néel temperature, the magnetization never drops even at the lowest temperature of our SQUID measurement (2 K).

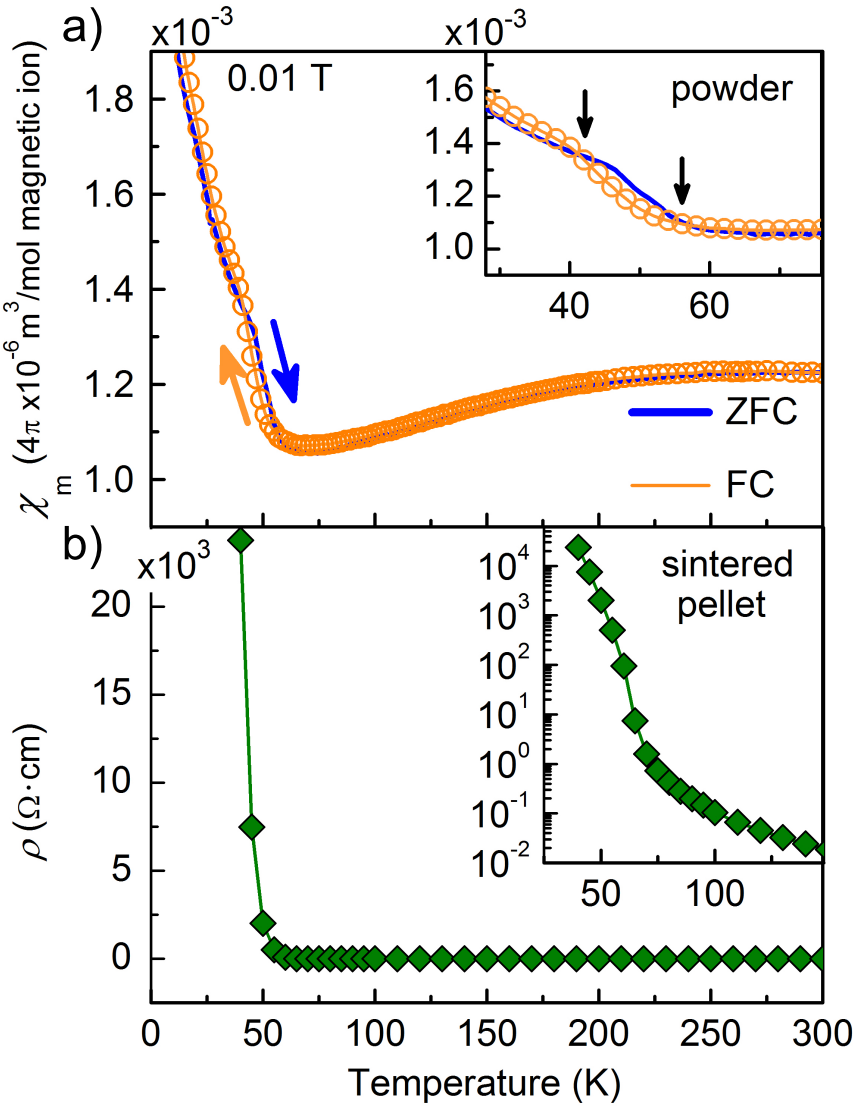

Figure 5.5: The molar magnetic susceptibility of $Bi_{1.7}V_8O_{16}$ vs. temperature for zero-field cooling (ZFC) and field-cooling (FC) measurements with an applied field of 0.01 T. The MI transition occurs near 60 K in this polycrystalline sample. The inset shows the hysteresis and multiple step behavior of the transition. Bottom panel shows resistivity measured of a sintered pellet of polycrystalline $Bi_{1.7}V_8O_{16}$ hollandite.

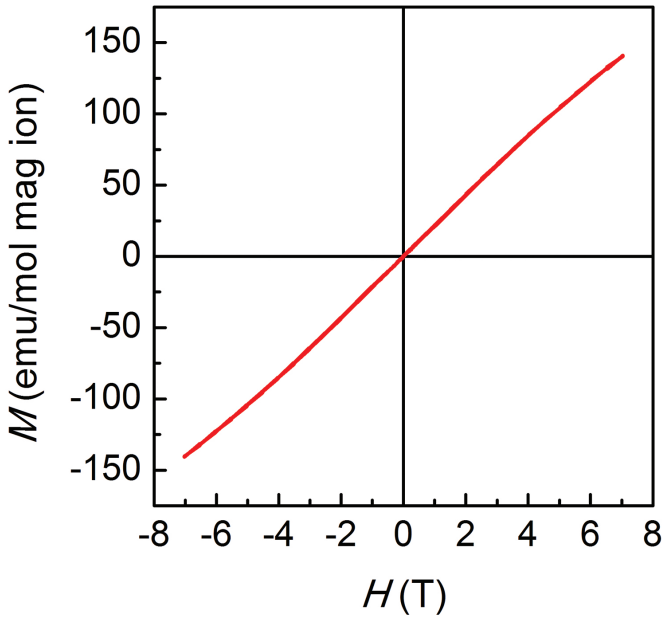

Figure 5.6: Magnetization vs. applied magnetic field for $Bi_{1.7}V_8O_{16}$, measured at 5 K. The linear response is indicative of paramagnetism in light of the neutron data not displaying any evidence for antiferromagnetic ordering. A subtle deviation develops at higher fields, although we are unsure of its underlying cause.

Finally, measuring the magnetization as a function of magnetic field revealed no long range magnetic order (Figure 5.6), as the magnetization varied linearly as a function of H, similar to either paramagnetic or antiferromagnetic behavior. While the M vs. H curve is neither proof for or against long-range antiferromagnetic ordering, in the context of other results such as neutron diffraction, $Bi_{1.7}V_8O_{16}$ does not appear to develop long-range magnetic order below the MIT.

5.3.3 Magnetotransport

First, electrical transport measurements were carried out on polycrystalline material. The resistivity data for a sintered pellet of $Bi_{1.7}V_8O_{16}$ is presented in Figure 5.5b, where a transition from a metallic to an insulating state occurs close to 70 K, concomitant with the observed magnetic transition. The resistivity is 7 orders of magnitude larger near 40 K than at 300 K, confirming the true MIT nature of the transition.

To better understand how crystallographic direction influences the transport properties and the effects of an external magnetic field, single crystals were measured in the PPMS. The transport measurements of a single crystal of $Bi_{1.7}V_8O_{16}$ as a function of temperature, magnetic field strength, and crystallographic direction are all presented in Figure 5.7. The crystals were needle-like in morphology due to the hollandite's quasi-1D structure, and field was applied either parallel or perpendicular to the needle axis, which corresponds to the c-axis.

The electrical resistivity data shown in Figure 5.7 demonstrates that field applied normal to the ladder direction suppresses the MIT. Upon cooling, the zero field data shows an MIT close to 62.5 K, where resistivity increases over six orders of magnitude compared to that of room temperature; upon heating, the crystal re-enters the metallic state but at a higher temperature of 80 K, demonstrating a first-order MIT with large hysteresis. Figure 5.8a shows an overall linear trend for the transition temperature T_{MI} plotted versus $H_{\perp}$, where hysteretic behavior appears to widen as $H_{\perp}$ approaches 8 T.

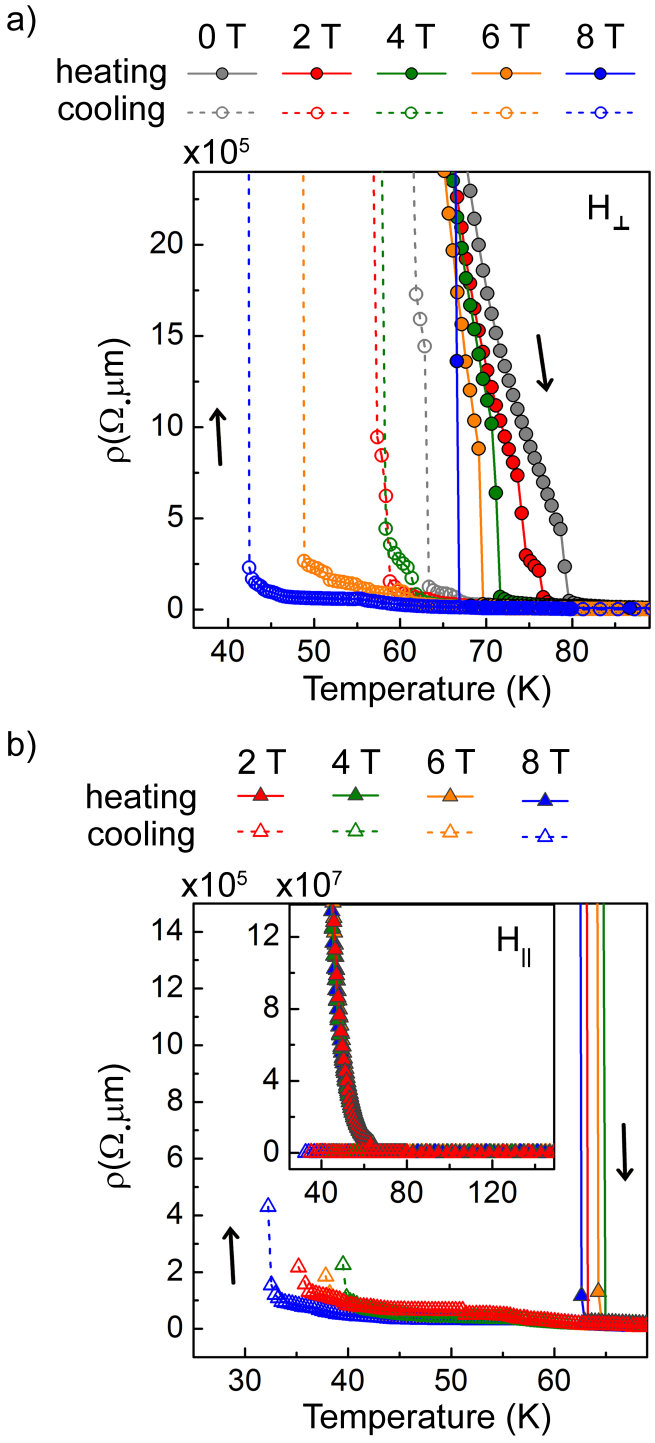

Figure 5.7: Electrical resistivity measurements as a function of applied magnetic field for a) field normal to the ladder, $H_{\perp}$, and b) field parallel to the ladder sides, $H_{||}$. The T_{MI} of $Bi_{1.7}V_8O_{16}$ displays significant field dependence for $H_{\perp}$ compared to the relatively field independent behavior of $H_{||}$.

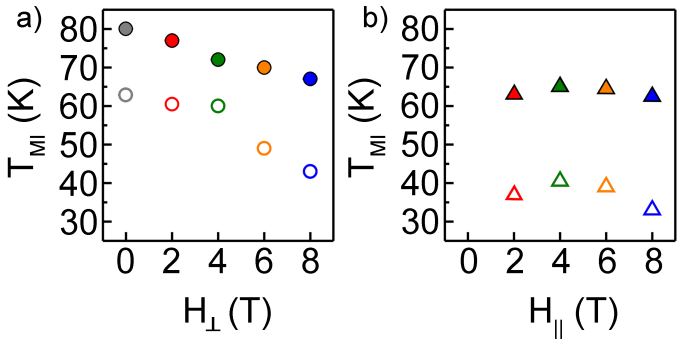

Figure 5.8: The linear dependence of the transition temperature T_{MI} vs. applied magnetic field for (a) $H_\perp$ and (b) $H_\parallel$. Filled symbols indicate T_{MI} as sample was heated, open symbols are for T_{MI} upon cooling.

When field is applied along the needle direction, and therefore along the triangular ladder, T_{MI} appears to be independent of field strength. The MIT is suppressed to approximately 40 K upon cooling and approximately 65 K upon heating regardless of H (Figure 5.8b). This likely indicates that the external field suppress formation of the V–V dimers, and the effect is more extreme when it is directly along the bond-axis.

The metal-insulator transitions have a much more sudden onset for $H_\parallel$ than for $H_\perp$, where the resistivity upon cooling suddenly diverged around 35-40 K, beyond the detection threshold of the instrument, as seen in Figure 5.7b. These directional experiments thus demonstrate that the coupling between the V cations must be anisotropic, with exchange interactions both along the ladder and its rungs driving the MIT.

5.3.4 Single crystal diffraction

To understand the behavior of the insulating phase as observed in the magnetization and magnetotransport data, we performed multiple diffraction studies of single crystal and polycrystalline $Bi_{1.7}V_8O_{16}$ at various temperatures. Full structures were obtained at 90 K, 200 K, and 300 K, while shorter measurements were carried out between 90 K to 300 K in 20 K steps to follow the thermal expansion. The lattice parameters as a function of temperature are presented in Figure 5.4, and no phase transition is observed in this temperature regime. Structural and lattice parameters at 200 K can be found in Table 5.2, and crystallographic information files for the full 200 K and 300 K structures can be found in Supplemental Information.

From the single crystal results, $Bi_{1.7}V_8O_{16}$ adopts a body-centered tetragonal space group $I4/m$ with the a-parameter determined by the size of the hollandite walls and the c-parameter by the V–V distances down the triangular ladder. At 200 K, the V–V distance in the c-direction is 2.913(1) Å and 2.999(1) Å along the ladder rungs (Figure 5.1a).

Remarkably, overlapped frames of the reciprocal lattice map of the $(h0l)$ and $(0kl)$ planes of $Bi_{1.7}V_8O_{16}$ reveal satellite reflections as intense as the main reflections (Figure 5.9a and b), indicating the presence of a charge density wave (CDW). Up to fourth order reflections can be observed for the CDW satellites. Interestingly, the CDW in $Bi_{1.7}V_8O_{16}$ is quasi-commensurate with the VO_6 framework as evidenced by the satellite reflections located close to (0 0 0.846$\mathbf{c}^*$) or similarly (0

$0\ -0.154\mathbf{c}^*$). Since we did not observe a temperature dependence in the location of the satellite reflections, the CDW is not truly incommensurate or independent from the VO_6 framework. Rather, it is commensurate with a very long unit cell of $a \times a \times 13c$. Hence, we refer to this as a quasi-commensurate CDW. Furthermore, no satellite reflections were observed in the $(hk0)$ reflections (Figure 5.9c) indicating that the CDW only occurs in the c-direction. Due to electrostatic repulsion between the cations in the hollandite channels, the Bi^{3+} cations deviate away from their average crystallographic position to form the CDW, a well known phenomenon in Ti-based hollandites.[189,190]

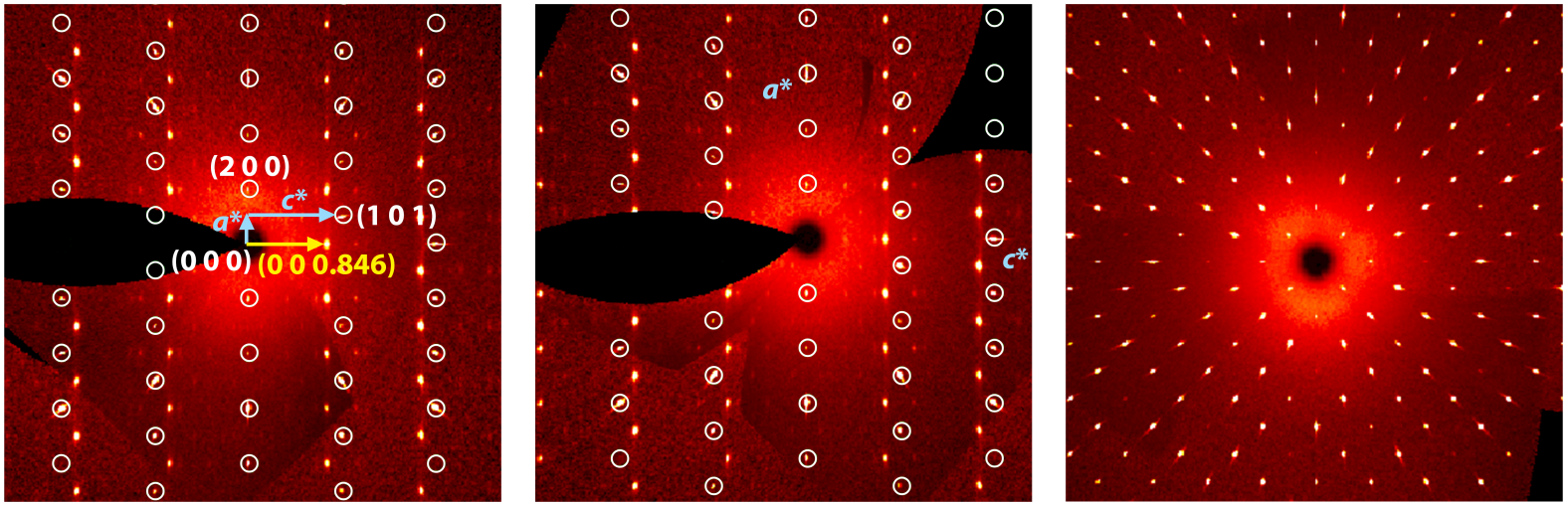

Figure 5.9: (a) Single crystal XRD data showing the main ($h0l$) reflections (white circles) and the satellite reflections corresponding to the Bi charge density wave, which can be indexed with a modulation vector of $0.154\mathbf{c}^*$. (b) The ($0kl$) reflections of the $Bi_{1.7}V_8O_{16}$ single crystal X-ray diffraction measurement, also showing the satellite reflections indicative of long-range modulation of the Bi cations within the hollandite channels. Faint streaking between satellite peaks indicates disorder amongst neighboring channels. No satellite reflections or streaking are observed in (c), showing the ($hk0$) reflections.

5.4 Discussion

In light of the structural and transport data, we would like to discuss the implications for charge, spin, and orbital order in $Bi_{1.7}V_8O_{16}$.

5.4.1 Charge order

Studies of the MITs in hollandites have revealed charge order as one of the prerequisites for such behavior. $K_2V_8O_{16}$ undergoes a two-step MIT between 155-170 K, with an accompanying decrease in magnetization.[69] Through high-resolution diffraction studies Komarek et al observed a structural transition from tetragonal to monoclinic in $K_2V_8O_{16}$ and proposed a complex CDW formation down the triangular ladders of the hollandite.[61] In their model, Komarek et al find that entire ladders are composed of either V^{3+} or V^{4+}. Similarly, the $Pb_{1.6}V_8O_{16}$ hollandite undergoes a MIT at 140 K; however, initial studies have yet to resolve whether charge ordering or significant structural transitions occur in this system.[191]

Previous studies on structurally related hollandites that do not undergo MITs, however, could be revealing in formulating the correct model for CDWs in hollandite oxides.[189,190,192] The work of Carter and Withers on titanium-based hollandites have shown a correlation between the wavelength of the CDW's modulation and the occupancy x in $A_xTi_8O_{16}$ where A is typically a large cation such as Ba^{2+} or K^+.[189,190,192] Carter and Withers connected the modulation of the propagation vector to the occupancy of the A cation through the relationship $x = 2(1-(1/m))$ where m is the ratio between the repeat period of the CDW.[190] For the title compound

Table 5.2: Structural parameters for $Bi_{1.7}V_8O_{16}$ from single crystal X-ray diffraction at 200 K. Standard uncertainties are given in parentheses.

$Bi_{1.72}V_8O_{16}$ (200 K, single crystal XRD), $I4/m$, $wR_2 = 3.70\%$					
a = 9.932(2) Å, c = 2.9133(6) Å, V = 287.4(1) Å^3					
atom	x	y	z	U_{iso} Å^2	Occ.
Bi1	0.0	0.0	0.060 (3)	0.0099(7)	0.24(1)
Bi2	0.0	0.0	0.161 (4)	0.0099(7)	0.19(1)
V	0.35520(4)	0.17036(4)	0	0.0053(2)	1
O1	0.1528(2)	0.1934(2)	0	0.0065(3)	1
O2	0.5408(2)	0.1648(2)	0	0.0065(3)	1

$Bi_{1.7}V_8O_{16}$, since the propagation vector of the CDW is $0.846\mathbf{c}^*$ (Figure 5.9a,b), $m = 0.154$ from the Carter-Withers expression. This 'compositional ruler' from the CDW would lead to $x = 1.69$, consistent with the nominal and refined values of the Bi stoichiometry from NPD and X-ray diffraction data. Since 0.154 is very close to 2/13, this would physically correspond to two Bi vacancies occurring across every 13 unit cells along the channel direction.

Our single crystal diffraction data suggests a charge ordering model for $Bi_{1.7}V_8O_{16}$ different from that of the other vanadium hollandites such as $K_2V_8O_{16}$ and $Rb_2V_8O_{16}$. The average oxidation state of vanadium in $Bi_{1.7}V_8O_{16}$ is $V^{3.363+}$, which would imply five V^{3+} ($S = 1$) for every three V^{4+} ($S = \frac{1}{2}$) cations in the triangular ladder. The absence of a Bi^{3+} cation in the tunnel would require nearby V cations to be in the higher oxidation state of 4+ in order to maintain charge balance. Therefore, the V^{4+} cations would order around the 2/13 Bi vacancies in the CDW to charge compensate the lattice. A schematic of the proposed charge ordering is depicted in Figure 5.10a. Kanke et al propose a similar CDW for the tunnel cations in the $Ba_{1.09}V_8O_16$ hollandite,[193] and Kuwabara et al a similar CDW for the transition metals in the hollandite $K_{1.6}Mn_8O_{16}$.[165] Interestingly, Mentré et al found that having $x < 1.7$ for the Bi site or mixing it with a variety of cations leads to A-site disorder and the compounds become semiconducting at all temperatures.[194] Therefore, the CDW seems to be key for the observation of the MIT.

Careful inspection of the $(h0l)$ and $(0kl)$ maps in Figure 5.9a and b, respectively, reveal another interesting feature with respect to the CDW. Although the satellite reflections at $\pm 0.846c*$ are fairly strong, there is some streaking which

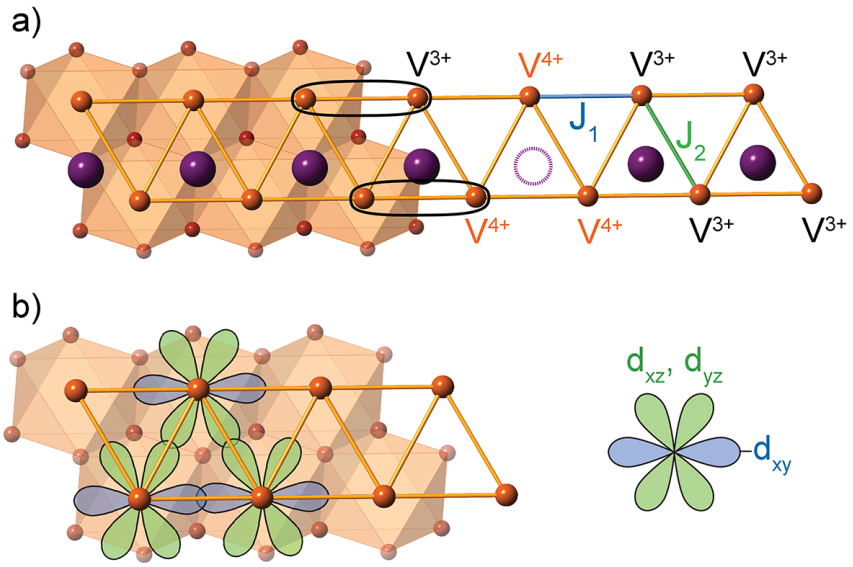

Figure 5.10: a) Proposed charge ordering for the vanadium triangular ladder of mixed spin states. b) Proposed orbital ordering.

occur in the $h-$ and $k-$directions. These arise from a finite amount of disorder between neighboring CDWs in the hollandite's tunnels. Indeed, Carter and Withers found that quenching titanate hollandites can lead to complete disorder of the CDWs and the reflections become lines in the electron diffraction patterns.[190] Their XRD powder patterns nicely demonstrate that the satellite reflections are much stronger when the hollandites are slow cooled. Likewise in our case, we found that the polycrystalline samples of $Bi_xV_8O_{16}$ to display some evidence for the CDW in the synchrotron data, but they are particularly weak due to the disorder of the CDW. Interestingly, the satellite of the (002) reflection seemed the broadest on account of the disorder along the c-direction.

5.4.2 Orbital order

Next, we address orbital ordering. Due to the octahedral coordination of the vanadium cations, we anticipate the normal '3 below 2' crystal field splitting of the d-orbitals. Since the V cations reside on the 8h Wyckoff position in space group $I4/m$ (Table 5.1), the local symmetry is actually lower than O_h and only contains a mirror plane with four unique V–O bond distances ranging from 1.844 Å to 2.021 Å at 200 K. Therefore, the crystal field can only be approximated as octahedral. Within this scheme, the e_g orbitals are aligned along the V–O bonds while the t_{2g} orbitals are involved in coupling the V cations to one another in the triangular ladder. In the charge ordered state, all the V cations should be orbitally active since they are in either the t_{2g}^1 or t_{2g}^2 state.

In the present system, an illustration of the orientation of the t_{2g} orbitals within the hollandite-type structure is displayed in Figure 5.10b. The d_{xy} orbital is oriented such that one pair of lobes is parallel to the tunnel direction. The four-fold crystal symmetry renders the d_{xz} and d_{yz} orbitals equivalent, pointing along the triangular ladder rung directions.

Orbital ordering is supported by the first-order structural distortion observed in the NPD data, where a large phase coexistence was observed between the insulating and metallic phases. Coupling of dimers along the tunnel direction would cause an increase in overlap between paired d_{xy} orbitals, further lifting the three-fold degeneracy of the t_{2g} orbitals. With an approximate ratio of five V^{3+} to three V^{4+} cations, the majority of dimers would then be either V^{3+}–V^{3+} pairs, or V^{3+}–

V^{4+} pairs.

The theoretical work on $Bi_xV_8O_{16}$ of Shibata et al suggests that orbital ordering is required to observe the MIT.[195] By deriving a spin-orbit Hamiltonian by second-order perturbation theory, Shibata et al. find a variety of orbitally ordered phases and suggests that each one contains a different ground spin state. Interestingly, one of these phases contains a majority of spin-singlets interspersed with unpaired $S = \frac{1}{2}$ minority states. This could explain the results from the solid state NMR studies of $Bi_xV_8O_{16}$ by Waki et al, who propose a charge ordered state along with orbital ordering, leading to spin singlet formation and finally to long-range antiferromagnetic ordering near 20 K.[188,196] We partially agree with some of the conclusions of Waki et al in that spin singlet formation comprises the majority of the states in $Bi_{1.7}V_8O_{16}$. Our NPD data, however, conclusively demonstrate no such long-range antiferromagnetic phase sets in below 20 K.

The recent computational studies from Kim et al suggest that spin, orbital, and lattice degrees of freedom are all coupled in the related $K_2V_8O_16$ hollandite.[182] The orbital ordering manifests in a Jahn-Teller type fashion, but Kim et al suggest that Mott-type physics rather than Peierls-type mechanism predominates with the electronic bands from the d_{xy} orbital playing the decisive role.

Orbital physics seems to be quite general in hollandites, and goes beyond the vanadates. In the structurally related system $K_2Cr_8O_{16}$, long-range ferromagnetic ordering sets in below 180 K.[54] For this system, the interaction between the charge and orbitally ordered Cr^{4+} and Cr^{3+} cations seems key to the formation of such an usual ground state–a ferromagnetic insulator. The theoretical work by Mahadevan

et al.[55] showed that ordering of the t_{2g} orbitals, which are the most significant for the M–M interactions in hollandites, would lead to ferromagnetic coupling between the cations.

5.4.3 Spin order

Finally, we address spin ordering in $Bi_{1.7}V_8O_{16}$. As shown in Figure 5.10b, we label the magnetic exchange along the ladder direction as J_1 and that along the rungs as J_2. It appears that the majority of the magnetic exchange interactions are antiferromagnetic in nature as evidenced by the magnetization data in the high-T phase. Above the MIT the magnetization data (Figure 5.5) reveals a broad feature that appears similar to the Bonner-Fisher susceptibility for Heisenberg chains with a negative J.[197] For $Bi_{1.7}V_8O_{16}$, the chains consists of predominately $S = 1$ cations, and therefore the Bonner-Fisher relation becomes $kT_{max}/|J| = 2.70$ where k is the Boltzmann constant and T_{max} is where the susceptibility is at a maximum. For the FC data (Figure 5.5) T_{max} is approximately 275 K. This value is quite high, and for one-dimensional materials this causes the susceptibility to broaden out in temperature.[120] Based on this relation, we can estimate the exchange interaction J_1 to be close to 8.31 meV.

At the MIT, the system appears to go from a quasi-1D chain of antiferromagnetically coupled V cations to a dimerization of V–V pairs. Therefore, the system goes from an extended solid of N centers to one that could be modeled as akin to $N/2$ molecules where N is Avogadro's number. Although the majority of Js remain

negative, it does appear that some of the V–V 'molecules' are ferromagnetically coupled.

Consider the Hamiltonian for a system consisting of dimers with the interatomic axis being the z-axis as given by

$$\mathscr{H} = g\mu_B S'_z H_z - 2J\mathbf{S_1}\cdot\mathbf{S_2} \tag{5.1}$$

where $\mathbf{S_1}$ and $\mathbf{S_2}$ would correspond to the spins of the two nearest neighbors in the V–V dimers, S'_z is the operator for the z-component of the total spin of the dimer, H_z is the external field applied along the z-axis, and g the Landé factor. For two interacting spin-$\frac{1}{2}$ electrons, Eq. 5.1 leads to the so-called Bleaney-Bowers equation for susceptibility given by

$$\chi = \frac{2Ng^2\mu_B^2}{kT(3+e^{\Delta/kT})} \tag{5.2}$$

where Δ is the energy gap between the two quantum numbers that describe the spin states of the dimer.[198] For a positive value for J in Eq. 5.1, the ground state of the system would be $S = 1$ (*i.e.* triplet state) and the excited state $S = 0$ (*i.e.* singlet state), with an energy gap of Δ between the states. While Eq. 5.2 does not necessarily apply to our dimers of V^{3+} and V^4 cations since they are of mixed spin states, the expression is informative in qualitatively describing the magnetization data below the MIT. For ferromagnetic coupling between the vanadium cations, a negative value of Δ (positive J) is found and therefore the susceptibility of Eq. 5.2 is seen to diverge at lower temperatures. For antiferromagnetic coupling, this suscep-

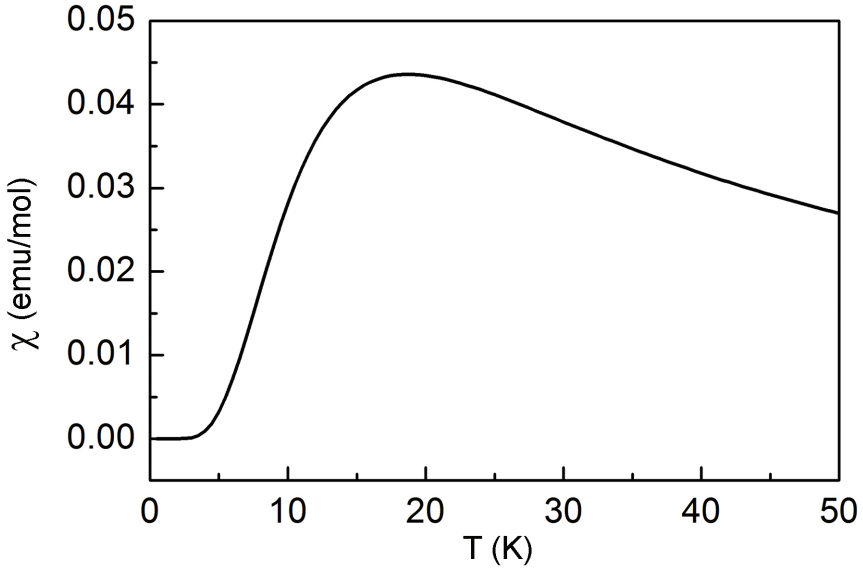

Figure 5.11: a) The Bleaney-Bowers equation for antiferromagnetic exchange between dimers.

tibility decreases to zero as 0 K is approached. Unlike all other vanadates undergoing an MIT, $Bi_{1.7}V_8O_{16}$ clearly shows the former. Figures 5.11 and 5.12 compare the Bleaney-Bowers model for ferromagnetic and antiferromagnetic coupling between two $S = \frac{1}{2}$ cations. While this model cannot be used to fit the magnetic susceptibility data, Figure 5.12 does allow the reader to qualitatively compare the two models against the low temperature susceptibility of $Bi_{1.7}V_8O_{16}$ below the MIT.

In the case of $Bi_{1.7}V_8O_{16}$, multiple steps are clearly seen in the ZFC and FC curves, below the MIT indicating the formation of ferromagnetically coupled dimers (Figure 5.5a). The hysteresis in the ZFC/FC curves should also rule out the possibility that these are just isolated ions producing a Curie tail. Furthermore, the magnetotransport data clearly indicate that the magnetic field controls the extent

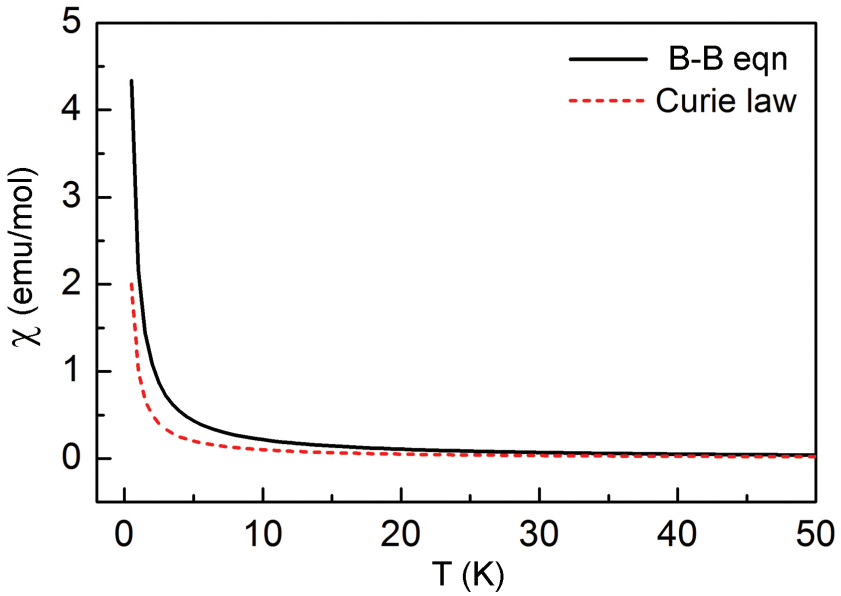

Figure 5.12: a) The Bleaney-Bowers equation for ferromagnetic exchange between dimers.

of the MIT and therefore enters into the coupling energy between the V–V centers (Eq. 5.1).

Even though both antiferromagnetic and ferromagnetic coupling is observed between the V–V dimers, the NPD data clearly indicate that no long-range ferromagnetic or antiferromagnetic ordering occurs. This suggests that the nature of magnetic interactions are either 1D or nearly 1D so that no magnetic Bragg reflections of long-range ordering ever occur. The triangular nature of the ladders likely also contribute to a frustration that disallows long-range ordering.

5.5 Conclusions

We have described a metal-insulator transition for a quasi-one dimensional system containing a mix of $S = 1$ and $S = \frac{1}{2}$ vanadium cations. Unlike all other known vanadates, the magnetic susceptibility of $Bi_{1.7}V_8O_{16}$ diverges below T_{MI}, although no long-range magnetic ordering is observed from neutron diffraction. The magnetotransport measurements reveal that the transition temperature is suppressed upon application of an external magnetic field, and this behavior is both hysteretic and anisotropic. A first-order structural transition is revealed by the coexistence of two tetragonal phases near the MIT indicative of dimerization between the mixed-spin cations. The MIT is thus best understood in terms of the interplay between the charge and orbital ordering of the V cations along the triangular ladder directions.

Chapter 6: Mixed-metal hollandites

6.1 Overview

The pure M hollandites demonstrate a range of properties; $K_2V_8O_{16}$ undergoes a metal-to-insulator transition.[69] $K_2Cr_8O_{16}$ is a ferromagnetic insulator below 95 K.[54] $K_{1.5}Ti_8O_{16}$ is paramagnetic,[75] and consistent with previous reports, we have observed a spin-glassy, antiferromagnetic response in the pure Mn hollandites.[41,139]

Throughout the work presented in this thesis, connections between the composition and the atomic structure of a material have been made in interpreting the physical behavior of hollandite materials. As seen in the differences between the $Ba_{1.2}Mn_8O_{16}$ and $Ba_{1.2}CoMn_7O_{16}$ in Chapter 3, the magnetic and electronic properties of materials can be significantly altered by relatively small changes in composition. We therefore have good reason to believe that investigations of the mixed-metal hollandite family will continue to reveal exciting electronic and magnetic properties for potential use in advanced material applications. By synthesizing the solid solutions of materials in between these compositions, we aim to map out the phase diagram to guide future optimizations for material applications.

Many other groups have studied mixed-metal hollandites,[48,70,74,75,79,81–95,156]

but to date, no comprehensive studies exist where an entire solid solution was described. The study that best attempts a solid solution was performed by Ishige et al on the $K_2V_{8-x}TixO_{16}$ material for x = 0, 0.3, and 4.0.[60] Their study was focused on explaining the mechanism driving the MIT in $K_2V_8O_{16}$, which they attribute to V-V dimerization based on changes observed in the V 2p X-ray absorption spectra.

Developing a systematic understanding of how incremental changes in composition affect the physical properties will allow for future hollandite materials to be tuned and developed for desired properties. Within this chapter, preliminary results in studying mixed-metal solid solutions of different hollandite compositions are detailed. Two solid solutions, $Bi_{1.7}Cr_xV_{8-x}O_{16}$ and $K_{1.7}Mn_xTi_{8-x}O_{16}$, are the focus of this chapter, while additional experimental work on other mixed-metal hollandite materials is detailed in Appendix A.

6.1.1 $K_yMn_xTi_{8-x}O_{16}$

Ti^{4+} is d^0, and therefore non-magnetic. The KTi_8O_{16} hollandite has been well-studied,[75,76] as has the KMn_8O_{16} hollandite (Chapter 4). By incrementally changing the composition between these two end-members, an attempt at understanding of the development of the complex frustrated magnetic behavior of KMn_8O_{16} was undertaken.

Kijima et al studied the effects of extracting K^+ from the tunnels of $K_xMn_2Ti_6O_{16}$ hollandite, but they did not vary the ratio of Mn to Ti, primarily focusing on the electrochemical effects and the possibility of replacing K^+ with Li^+.[92] Using the $I4/m$

space group, they observed the Mn valency transition from trivalent to tetravalent upon removal of K^+.

Our research group has published initial findings on doping the $K_yM_xTi_{8-x}O_{16}$ for M = Sc-Ni and $x = y = \sim 1.5$.[75] Magnetization versus temperature measurements indicated that all phases were Curie paramagnets. The μ_{eff} = 4.99 μ_B and θ_{CW} = -40.04 extracted for the Mn-substituted sample were consistent with the d-electron count given by combined X-ray diffraction and elemental analysis techniques.[75] Using this material as a starting point, we sought to map out the $K_yMn_xTi_{8-x}O_{16}$ solid solution.

6.1.1.1 Synthesis & experimental details

Samples were synthesized through a salt flux method to produce polycrystalline hollandite materials , $K_{1.7}Mn_xTi_{8-x}O_{16}$. Starting reagents included KCl (99.2%, J.T. Baker), Mn_2O_3 (99%, Sigma-Aldrich), Co_3O_4 (74%-gravimetric Co, Sigma-Aldrich), $Ba(NO_3)_2$ (99.999%, Sigma-Aldrich). Reagents were used without further purification.

A powder mixture of TiO_2, Mn_2O_3, and KCl was ground with an agate mortar and pestle. The reagent mixtures were then heated in covered alumina crucibles under ambient atmosphere. Heating was maintained at a rate of 100 K/h up to 1123 K, soaked for 72 h, then cooled to room temperature at 100 K/h. The obtained samples were washed in DI water to dissolve KCl, then dried at 373 K for one hour.

Room temperature powder X-ray diffraction (XRD) data was collected on a

Table 6.1: Room temperature lattice parameters for $K_yMn_xTi_{8-x}O_{16}$ from powder X-ray diffraction refinements. Standard uncertainties are given in parentheses.

Sample	a (Å)	c (Å)	R_{wp} (%)
$K_yMnTi_7O_{16}$	10.161(3)	2.958(7)	8.519
$K_yMn_2Ti_6O_{16}$	10.163(2)	2.956(6)	9.044
$K_yMn_3Ti_5O_{16}$	10.144(3)	2.958(6)	6.474

Bruker D8 X-ray diffractometer with Cu Kα radiation, λ = 1.5418 Å, (step size=0.013°, with 2θ range from 8°-140°). Constant wavelength neutron powder diffraction data was collected on the high resolution BT-1 instrument at the National Institute of Standards and Technology (NIST) Center for Neutron Research (NCNR) with a λ = 2.078 Å (Ge311 monochromator) for various temperatures between 10 K and 300 K. All powder diffraction data was analyzed using the TOPAS software.[115]

Field-cooled (FC) and zero-field-cooled (ZFC) magnetization measurements were taken from 2 K - 300 K with a Quantum Design magnetic property measurement system (MPMS) on a polycrystalline sample. Measurements were in direct current mode, with an applied magnetic field of 0.01 T (100 Oe). Magnetization versus field up to 7 T were also taken on the MPMS with a polycrystalline sample at 5 K.

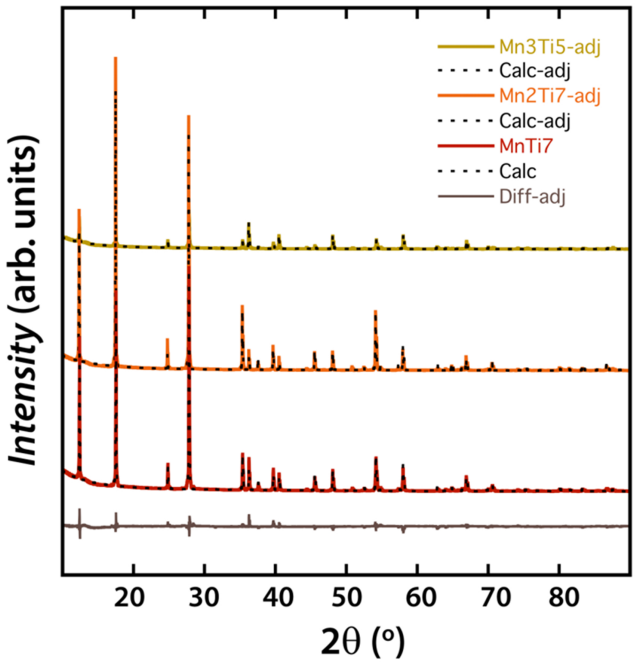

Figure 6.1: X-ray diffraction for $K_yMn_xTi_{8-x}O_{16}$.

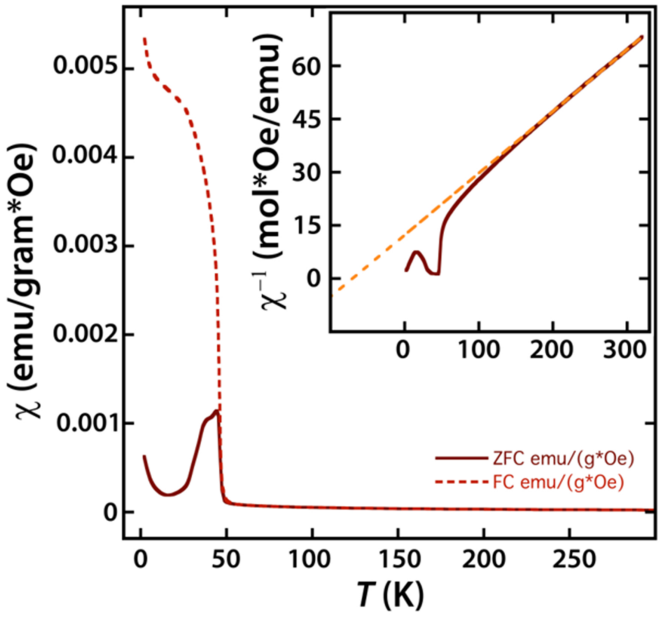

Figure 6.2: Magnetic susceptibility of $K_{1.7}Mn_xTi_{8-x}O_{16}$.

Table 6.2: Curie-Weiss parameters extracted from the high temperature paramagnetic regions of $K_yMn_xTi_{8-x}O_{16}$ $1/\chi$ plots.

Sample	T_N (K)	θ (K)	C (cm^3 K mol^{-1}	$\mu_{eff}(\mu_B)$
$K_yMnTi_7O_{16}$	~45	-40.3	4.53	6.05
$K_yMn_2Ti_6O_{16}$	~47	-41.5	2.27	4.28
$K_yMn_3Ti_5O_{16}$	~48	-66.6	1.89	3.90

6.1.1.2 Results

The observed magnetic susceptibility of $K_{1.7}Mn_xTi_{8-x}O_{16}$ showed a transition occuring at ~ 47 K. A representative susceptibility of the $K_{1.7}Mn_3Ti_5O_{16}$ compound is shown in Figure 6.3. The FC and ZFC measurements, particularly of the $K_{1.7}Mn_3Ti_5O_{16}$ sample, are very similar to the reported magnetization of $BaMn_3Ti_4O_{14.25}$ by Liu et al.[87]

Calculated effective moments and Curie constants for the different compositions are presented in Table 6.2. The observed values for μ_{eff} do not agree well with the values expected for the targeted compositions, assuming that Ti is present in an oxidation state of 4+.

The magnetization versus field measurements of $K_{1.7}Mn_3Ti_5O_{16}$ (shown in Figure 6.3) also closely resemble the reported hysteresis for $BaMn_3Ti_4O_{14.25}$ by Liu et al.[87]

Measuring the $K_{1.7}Mn_3Ti_5O_{16}$ at BT-1 revealed one significant magnetic peak

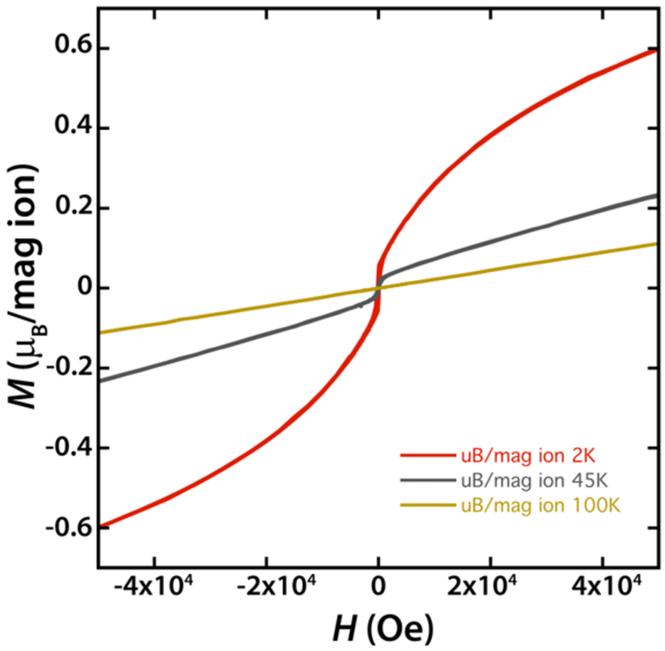

Figure 6.3: Magnetization vs. Field Measurements of $K_{1.7}Mn_3Ti_5O_{16}$.

at low temperature, along with some minor nuclear reflections that were not observed in the XRD data. Rietveld refinement of the BT-1 data revealed the presence of a small amount of hausmannite, Mn_3O_4, which undergoes a magnetic transition at ~ 42 K. We thus concluded that the magnetic behavior we had observed was likely due to the Mn_3O_4 impurity, not the $K_yMn_xTi_{8-x}O_{16}$ samples.

6.1.1.3 Discussion

Mn_3O_4 is a magnetically disruptive impurity, easily formed in the solid state techniques utilized herein. Future efforts to pursue the $K_yMn_xTi_{8-x}O_{16}$ solid solution should include elemental analysis techniques such as ICP-AES to verify the incorporation of both transition metal cations into the material. Microscopy

techniques might also give an indication as to whether or not different phases are present on the surface of the bulk material, as the lab XRD data we utilized did not reveal the existence of the impurity phase.

6.1.2 $Bi_{1.7}Cr_xV_{8-x}O_{16}$

For a long time, researchers have been interested in antiferromagnetic materials with $S = \frac{1}{2}$ ions on a frustrated lattice due to numerous theoretical predictions that such systems should exhibit spin liquid or even more exotic behavior due in part to quantum spin fluctuations. Systems with integer spins, (S = 1, 2, 3) are also of particular interest, as Haldane conjectured the differences in exchange symmetry between half-integer and integer spin systems to have a dramatic effect on the nature of excitations in the material.[12] These so-called 'Haldane chains' are an extension of the one dimensional quantum Heisenberg spin model.

In spite of intensive search efforts, the number of materials featuring the 1D or pseudo-1D nature of combined with purely integer spin states is small. If one wanted to design a 1D (or quasi-1D) system with a magnetically-driven MIT, a system of predominately $S = 1$ species mixed with some nearest neighbor $S = \frac{1}{2}$ units might suffice, assuming that the orbital degrees of freedom allow ferromagnetic coupling between the two species. In the $K_2Cr_8O_{16}$ hollandite, one of the few well-known ferromagnetic insulators, the average charge of chromium is $Cr^{3.75}$. This leads to a mixture of $S = 1$ and $S = \frac{3}{2}$ cations in the chains where $S = 1$ species are the majority. The quasi-1D nature of the transition metal network in hollandites,

and the compositional tunability, allow the researcher to target an S=1 framework. Understanding the magnetic behavior of the $Bi_{1.7}V_8O_{16}$ hollandite, and related variations may thereby provide a potential material for exploring the properties of Haldane chains.

6.1.2.1 Synthesis & experimental details

Polycrystalline samples of $Bi_{1.7}Cr_xV_{8-x}O_{16}$ hollandites were produced by grinding together stoichiometric ratios of V_2O_3 (99.7%, Alfa Aesar), V_2O_5 (98+%, Sigma Aldrich), and Bi_2O_3 (99%, Fisher). Reagents were used without further purification. After grinding together, the powdered mixture was heated to 1173 K at a rate of three degrees per minute, in an evacuated flame-sealed quartz glass ampule. Upon reaching the target temperature the sample soaked for 72 hours, followed by furnace cooling.[183]

Room temperature powder X-ray diffraction (XRD) data was collected on a Bruker D8 X-ray diffractometer with Cu Kα radiation, λ = 1.5418 Å, (step size=0.013°, with 2θ range from 8°-140°). Powder diffraction data was analyzed using the TOPAS software.[115]

Field-cooled (FC) and zero-field-cooled (ZFC) magnetization measurements were taken from 2 K - 300 K with a Quantum Design magnetic property measurement system (MPMS) on a polycrystalline sample. Measurements were in direct current mode, with an applied magnetic field of 0.01 T (100 Oe).

6.1.2.2 Results

Rietveld refinements were carried out to extract structural and lattice parameters from the data (Figure 6.4). These results are presented in Table 6.3.

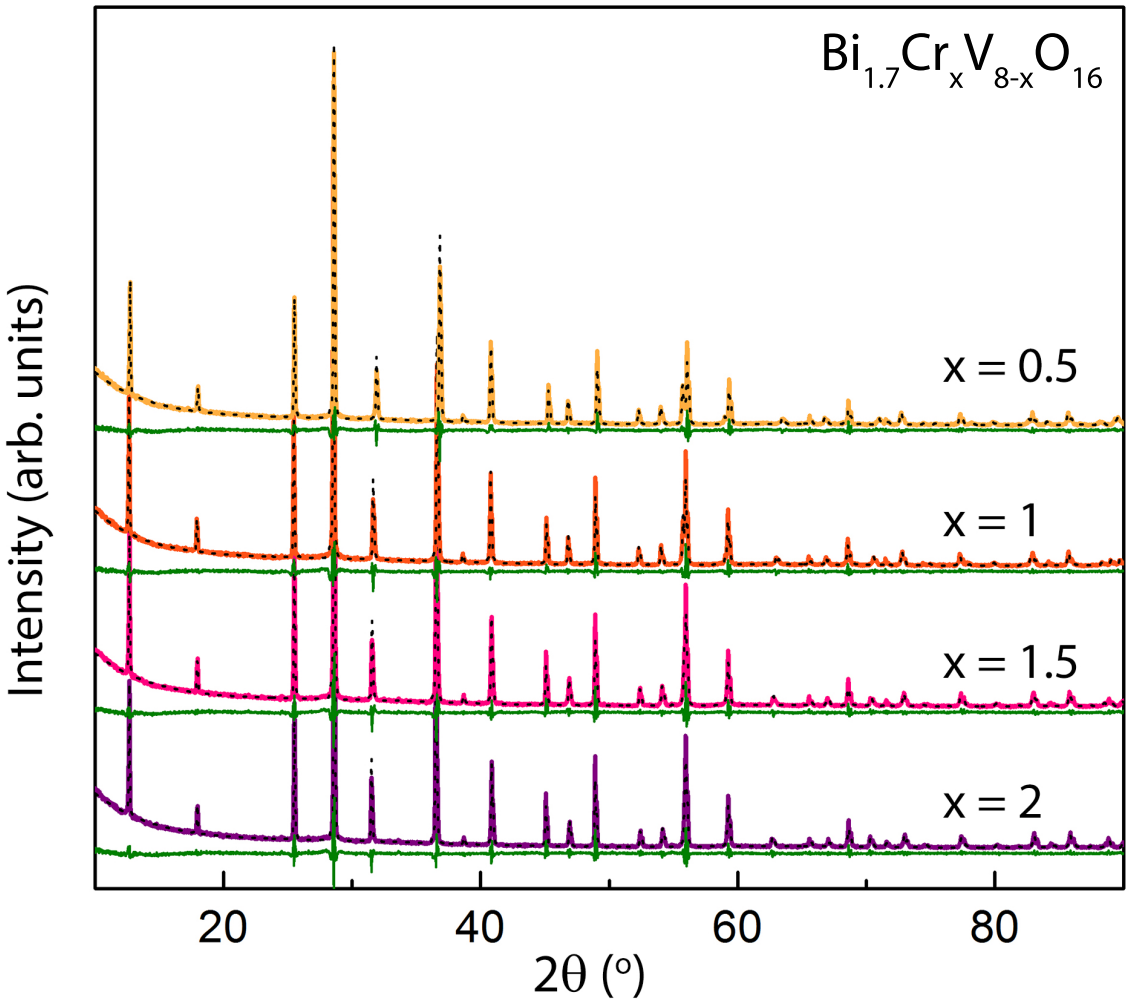

Figure 6.4: Rietveld refinement of room temperature XRD data (UMD) for $Bi_{1.7}Cr_xV_{8-x}O_{16}$. The green line indicates the difference between the observed data (colored lines) and the calculated model (black dashes).

Table 6.3: Room temperature lattice parameters for $Bi_yCr_xV_{8-x}O_{16}$ from powder X-ray diffraction refinements. Standard uncertainties are given in parentheses.

Sample	a (Å)	c (Å)	Bi occupancy	R_{wp} (%)
$Bi_yCr_{0.5}V_{7.5}O_{16}$	10.161(2)	2.958(2)	0.402	8.519
$Bi_yCrV_7O_{16}$	10.163(2)	2.956(2)	0.416	9.044
$Bi_yCr_{1.5}V_{6.5}O_{16}$	10.144(3)	2.958(2)	0.413	6.474
$Bi_yCr_2V_6O_{16}$	10.144(1)	2.958(2)	0.418	6.474

Rietveld treatment of lab XRD data showed phase pure $Bi_yCr_xV_{8-x}O_{16}$, for x = 0.5, 1, 1.5, and 2. Lattice parameters extracted from the Rietveld technique are presented in Table 6.3. The refined Bi^{3+} occupancy leads to an average bismuth stoichiometry of 1.65. A slight decrease in the a parameter is observed upon increasing x, without a noticeable accompanying trend in the c parameter.

Elemental analysis was performed on the samples of $Bi_yCr_xV_{8-x}O_{16}$ utilizing inductively coupled plasma atomic emission spectroscopy (ICP-AES). The resulting compositions confirmed the presence of Cr within the material, though the typical amount was approximately 0.2 molar equivalents lower than the targeted stoichiometry.

The observed magnetic susceptibility of $Bi_yCr_xV_{8-x}O_{16}$, was very consistent across the different compositions. Field-cooled (FC) and zero field cooled measurements (ZFC) trace a traditional Curie-Weiss paramagnetic response until T < ~ 10 K, at which point the magnetization of the ZFC curve decreases sharply, while the

Table 6.4: Curie-Weiss parameters extracted from the high temperature paramagnetic regions of $Bi_yCr_xV_{8-x}O_{16}$ $1/\chi$ plots.

Sample	T_N (K)	θ_{CW} (K)	C (cm^3 K mol^{-1}	$\mu_{eff}(\mu_B)$
$Bi_yCr_{0.5}V_{7.5}O_{16}$	~9	848	4.53	6.05
$Bi_yCrV_7O_{16}$	~9	360	2.27	4.28
$Bi_yCr_{1.5}V_{6.5}O_{16}$	~9	279	1.89	3.90
$Bi_yCr_2V_6O_{16}$	~9	176	1.89	3.90

FC continues to increase. Calculated effective moments and Curie constants are presented in Table 6.4, and trends across the different compositions are shown in Figure 6.5. A decrease in both the θ_{CW} andμ_{eff} values are observed upon increasing the amount of Cr.

6.1.2.3 Discussion

Both the X-ray data and the ICP-AES results confirm the presence of Cr in the samples synthesized herein. The profile of the magnetic responses of the samples did not change substantially across the compositions, though the decrease in θ_{CW} shows that the strength of magnetic interactions is decreasing. Though very preliminary, these materials warrant further investigation.

X-ray photoelectron spectroscopy would determine the oxidation states of the V and Cr cations in the framework, giving an idea of whether or not the materials are approaching a true S = 1 state with the addition of Cr. Neutron diffraction

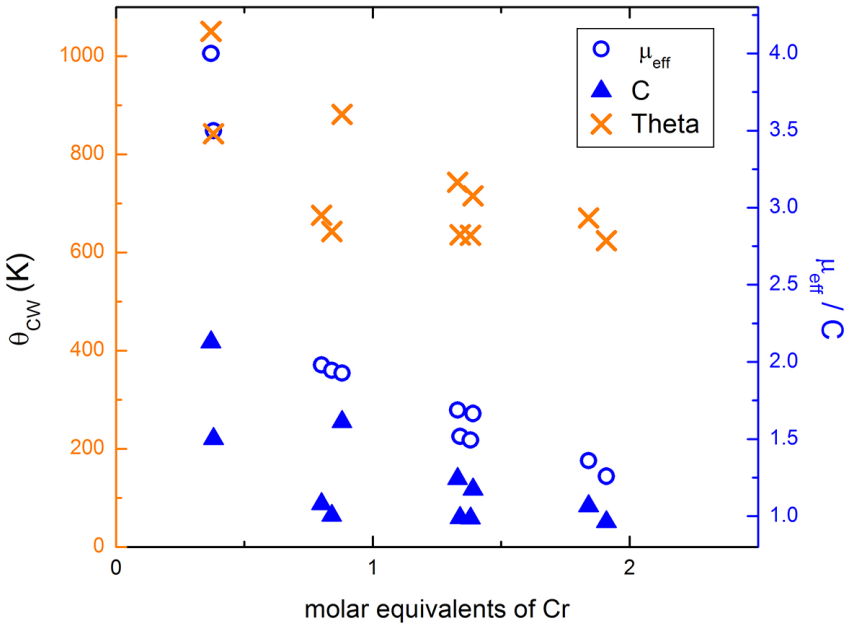

Figure 6.5: Trends in θ_{CW}, C, and μ_{eff} for $Bi_yCr_xV_{8-x}O_{16}$ as a function of molar Cr content. Error bars are smaller than plot symbols used.

measurements will also provide insight, both into the structure of the materials, as well as regarding the magnetic behavior.

Chapter 7: Overall conclusions & future work

7.1 Conclusions

Throughout the work presented in this thesis, connections between the composition and the atomic structure of a material have been made in interpreting the physical behavior of hollandite materials.

Several different hollandite materials have been successfully synthesized and characterized to varying extents. While much of the previous work done on hollandites concentrates on the possibility of using these materials as electrode materials in batteries, significantly less attention has been expended in understanding the bulk magnetic and electronic properties of these materials. This limitation has likely stemmed from the synthetic difficulties in obtaining bulk, highly crystalline samples. While this limitation is still very present, work done in the Rodriguez group, presented herein as well as in titanium-based hollandites, suggests the use of salt flux techniques as a very promising avenue for crystal growth of hollandites in the future.[75]

Crystal structures have been resolved by X-ray and neutron powder diffraction, as well as single crystal X-ray studies when possible. Magnetic behavior has been evaluated using both a SQUID magnetometer and neutron diffraction.

The intense magnetic frustration observed in $Ba_{1.14}Mn_8O_{16}$ was relieved with the inclusion of Co^{2+} cations into the framework of $Ba_{1.10}Co_yMn_{8-y}O_{16}$. Magnetization and resistivity measurements show that the cobalt-substituted hollandite belongs to the rare class of ferrimagnetic insulators. Neutron diffraction measurements made it possible for us to describe the first magnetic structure solution of $Ba_xMn_8O_{16}$, consisting of a complex antiferromagnet with a large magnetic unit cell.

Contrary to reports in the literature, $K_{1.35}Mn_8O_{16}$ does not appear to exhibit tetragonal symmetry as seen by the poor fits obtained by Rietveld refinement of both neutron and X-ray data. While two plausible cells are discussed here, the quality of the data collected did not allow for a full solution of either the atomic or magnetic structures.

$Bi_{1.7}V_8O_{16}$ was observed to undergo a metal-insulator transition upon cooling, but unlike all other known vanadates, the magnetic susceptibility of $Bi_{1.7}V_8O_{16}$ diverges below T_{MI}, though no long-range magnetic ordering is observed from neutron diffraction. We also observed revealed both anisotropic and hysteretic behavior accompanying the field-dependence of the MIT.

Finally, investigations into mixed-metal hollandites are just beginning. The properties of the $Bi_{1.7}Cr_xV_{8-x}O_{16}$ series, where x≤3, were initiated in hopes of driving the material into a purely $S = 1$ state and observing Haldane-like behavior. The effects of systematically changing the composition between two known end members to synthesize $K_{1.7}Mn_xTi_{8-x}O_{16}$ materials was frustrated by the existence of an Mn_3O_4 impurity phase. Future investigations of this material will need to find

synthetic routes that avoid this impurity, or ways of separating the Mn_3O_4 from the desired material post-synthetically.

It can be seen that the observed properties vary significantly with changes in hollandite composition. Magnetic behavior is affected by orbital ordering and charge ordering. These results suggest the possibility of rich electrical and magnetic phase diagrams for OMS materials. This work contributes to a greater understanding of the correlations between structure and properties, particularly in both hollandite materials and geometrically frustrated systems, allowing for the design of materials exhibiting certain physical phenomena.

7.2 Future work

Future TOF neutron experiments of $Ba_{1.2}Mn_8O_{16}$ and its Co-substituted derivative, measured at temperatures below the magnetic ordering transitions, will be helpful to search for possible orbital ordering from Jahn-Teller distortions. We would also like to run the same sample on DCS to obtain an overview of the excitations present in this sample. Based off of theoretical calculations performed by Seriani et al, we predicted that the addition of Co into the $Ba_{1.2}Mn_8O_{16}$ structure forces the moments from a Heisenberg-like system into a more restricted Ising-like configuration. DCS will allow us to focus on low $\mathbf{Q}$ values, while selecting the wavelength with the highest energy resolution. We are interested to see if more interesting dynamics are at play in the hollandites.

Further good quality diffraction data needs to be collected for the $K_{1.6}Mn_8O_{16}$

phase, preferably using facilities such as a synchrotron radiation source. This would allow us to fully elucidate the structure and may further our attempts at resolving the magnetic structure allowing the physical properties of the material to be fully characterized. We would also like to measure $K_{1.4}Mn_8O_{16}$ to determine a) the spin coupling of these systems and b) elucidate the ordering and behavior of any spin waves present in these hollandites.

Measuring $Bi_{1.7}V_8O_{16}$ on BT-1 as a function of magnetic field strength would allow us to investigate our hypothesis that the ferromagnetic coupling drives the MIT. The formation of such dimers is manifest by tetragonal-to-tetragonal structural transition. As the neutron scattering cross section for vanadium is negligible, low-temperature synchrotron X-ray diffraction experiments would be very beneficial in locating the vanadium cations through the structural distortion.

There are numerous routes of inquiry to pursue on our nascent studies of the mixed metal solid solutions. Performing X-ray photoelectron spectroscopy on he $Bi_{1.7}Cr_xV_{8-x}O_{16}$ hollandite materials would determine the oxidation states of the V and Cr cations in the framework, giving an idea of whether or not the materials are approaching a true S = 1 state. Neutron diffraction measurements at will also provide insight, both into the structure of the materials, as well as regarding the magnetic behavior.

Of course, growth of single crystals would allow us to expand our studies for all of the materials described herein. Efforts to merely tune the salt flux and solid state techniques utilized herein may not be sufficient, and floating-zone furnaces or hydrothermal furnaces may broaden the scope of our synthetic capabilities.

Appendix A: Further experiments on mixed metal hollandites

All samples were synthesized by salt flux methods. Stoichiometric amounts of starting materials (see below) were ground using an agate mortar and pestle. They were then transferred to alumina crucibles and placed in a furnace at 850°CC for 72 hours ramping at 100°C/h. Subsequent washing with deionized water was necessary to remove remaining KCl, which was used as a mineralizer. The samples were then dried over a hot plate at 100°C for one hour.

A.1 $Ba_{1.2}FeMn_7O_{16}$

We aimed for an Fe content of 1. The following table summarizes the reagents used in different trials, specific conditions and refined PXRD results.

Table A.1: Experimental details for $Ba_{1.2}FeMn_7O_{16}$ hollandite

Sample No.	Starting materials	Additional	PXRD Results
AML085	$Ba(NO_3)_2$ + Mn_2O_3 + Fe_2O_3 + KCl	under O_2 flow	98% hollandite + 2% Mn_2O_3
NSL035	$Ba(NO_3)_2$ + Mn_2O_3 + $Fe(NO_3)_3 \cdot 9H_2O$ + KCl	pellets calcined at 650 °	96% hollandite + 4% Mn_2O_3 + $BaCO_3$
NSL041	NSL035 + $Ba(NO_3)_2$ + Fe_2O_3 + KCl	-	98% hollandite + 2% Mn_2O_3 + $BaCO_3$
NSL039A	$Ba(NO_3)_2$ + Mn_2O_3 + FeO + KCl	under O_2 flow	97% hollandite + 4% Mn_2O_3 + $BaCO_3$
NSL038	$Ba(NO_3)_2$ + Mn_2O_3 + FeO + KCl	-	92% hollandite + 3% Mn_2O_3 + 5% $BaCO_3$
NSL043B	$Ba(NO_3)_2$ + Mn_2O_3 + Fe_2O_3 + KCl	-	88% hollandite + 9% Mn_2O_3 + 3% $BaCO_3$
NSL047A	$Ba(NO_3)_2$ + Mn_2O_3 + FeO + KCl + KNO_3	-	71% hollandite + 4% $BaMnO_3$ + 16% $Ba_{6.3}Mn_{24}O_{48}$ + 9% KCl
NSL052	$Ba(NO_3)_2$ + $Mn(NO_3)_3 \cdot 4H_2O$ + Fe_2O_3 + KCl	pellets calcined at 650 °	96% hollandite + 3% $BaCO_3$ + 12% $BaFe_{12}O_{19}$
NSL053B	NSL052	stirred in HCl	99% hollandite + 1% $BaFe_{12}O_{19}$

We experimented with the following variables: different sources of iron and manganese, for oxidation states of +2 or +3, the presence of an oxidizing atmosphere (O_2 flow) to favor oxidation, and the addition of a second mineralizer (KNO_3), which also acts as an oxidizing agent. Since the most common impurity was one of the starting materials, Mn_2O_3, we tried refiring the sample with more $Ba(NO_3)_2$, KCl and iron oxide. Although the amount of Mn_2O_3 was reduced, it was not completely removed. The sample NSL 053 B was almost phase pure, although the intensity of the peaks was slightly smaller compared to other samples'. The refined pattern is shown below.

The peak at around $2\theta \sim 24°$C corresponds to the $BaCO_3$ impurity. This phase was usually included in the refinement, however, sometimes the software identified it as a background, in those cases, we left the phase out of the refinement, but acknowledged its presence.

A.2 $Ba_{1.2}Ni_xMn_{8-x}O_{16}$

We aimed for a Ni content between 0.5 and 1. The following table summarizes the reagents used in different trials, specific conditions and refined PXRD results.

Table A.2: Experimental details for $Ba_{1.2}Ni_xMn_{8-x}O_{16}$ hollandite

x	Sample No.	Starting materials	Additional	PXRD Results
1	AML122	$Ba(NO_3)_2$ + Mn_2O_3 + NiO + KCl	under O_2 flow	94% hollandite + 4% Mn_2O_3 + 2% $BaCO_3$
1	AML123	$Ba(NO_3)_2$ + Mn_2O_3 + $Ni(NO_3)_2$ + KCl	calcined, refired in KCl	91% hollandite + 6% NiO + 3% $BaCO_3$
0.5	NSL024A	$Ba(NO_3)_2$ + Mn_2O_3 + NiO + KCl	-	97% hollandite + 2% NiO + 1% $BaCO_3$
0.5	NSL030A	NSL024A + KCl	-	89% hollandite + 7% $NiMn_2O_4$ + 4% $BaCO_3$
0.5	NSL031AA	NSL024A	stirred in HCl	98% hollandite + 2% NiO
0.75	NSL036A	$Ba(NO_3)_2$ + Mn_2O_3 + NiO + KCl	-	94% hollandite + 3% NiO + 3% $BaCO_3$
0.75	NSL045B	NSL036A + $Ba(NO_3)_2$ + Mn_2O_3 + KCl	-	88% hollandite + 9% $NiMn_2O_4$ + 3% $BaCO_3$
1	NSL024B	$Ba(NO_3)_2$ + Mn_2O_3 + NiO + KCl	-	91% hollandite + 6% NiO + 3% $BaCO_3$
1	NSL031BA	NSL024B	stirred in HCl	93% hollandite + 7% NiO

In this case we tried to obtain a phase pure hollandite by: varying the nickel source, (which in this case did not change its oxidation state), introducing an oxidizing atmosphere and refiring the samples to make the leftover starting materials react. In addition, our target stoichiometries varied in Ni / Mn content, we observed that lower amounts of Ni integrated better in the hollandite structure. Although it contained a NiO impurity, the sample NSL 031AA was our best trial. The refined pattern is shown below.

Field cooled and Zero Field cooled magnetic susceptibility measurements were carried out on this sample using a SQUID magnetometer. These are shown below.

A.3 $Ba_{1.2}Cr_xMn_{8-x}O_{16}$

We aimed for a Cr content between 0.25 and 1. Table A.3 summarizes the reagents used in different trials, specific conditions and refined PXRD results.

We did not consider different chromium sources for this set of experiments. Instead, we tried different conditions in the furnace: reducing and oxidizing atmospheres as well as different target temperatures. As seen in the PXRD results column, the percentage of hollandite in our samples was not great. Indeed, when washing these samples with DI water, they liquid often turned green, indicating that the chromium was not being successfully inserted in the hollandite structure. Same as with the Ni samples, we obtained better results at lower Cr content. Though it contained remaining starting materials and barium carbonate, AML127B was our best sample.

Table A.3: Experimental details for $Ba_{1.2}Cr_xMn_{8-x}O_{16}$ hollandite

x	Sample No.	Starting materials	Additional	PXRD Results
	NSL005	$Ba(NO_3)_2$ + Mn_2O_3 + Cr_2O_3 + KCl	-	78% hollandite + 14% Mn_2O_3 + 8% $BaCrO_4$
1	NSL008A	$Ba(NO_3)_2$ + Mn_2O_3 + Cr_2O_3 + KCl	-	78% hollandite + 14% Mn_2O_3 + 8% $BaCrO_4$
1	NSL008B	$Ba(NO_3)_2$ + Mn_2O_3 + MnO_2 + Cr_2O_3 + KCl	-	17% hollandite + 50% Mn_2O_3 + 33% $BaCrO_4$
1	NSL013A	$Ba(NO_3)_2$ + Mn_2O_3 + Cr_2O_3 + KCl	950° instead	49% hollandite + 44% Mn_3O_4 + 6% $BaCrO_4$
1	NSL013B	$Ba(NO_3)_2$ + Mn_2O_3 + Cr_2O_3 + KCl	750° instead	40% hollandite + 50% Mn_2O_3 + 10% $BaCrO_4$
1	NSL015	$Ba(NO_3)_2$ + Mn_2O_3 + Cr_2O_3 + KCl	under N_2 flow	no hollandite – 93% Mn_3O_4 + 7% $BaCrO_4$
0.25	AML127B	$Ba(NO_3)_2$ + Mn_2O_3 + Cr_2O_3 + KCl	-	96% hollandite + 4% Mn_3O_4 + $BaCO_3$
0.5	NSL020	$Ba(NO_3)_2$ + Mn_2O_3 + Cr_2O_3 + KCl	-	78% hollandite + 13% Mn_2O_3 + 9% $BaCrO_4$
0.75	AML127D	$Ba(NO_3)_2$ + Mn_2O_3 + Cr_2O_3 + KCl	-	74% hollandite + 2% Mn_2O_3 + 5% $BaCrO_4$

A.4 $K_yV_xMn_{8-x}O_{16}$

Samples of $K_yV_xMn_{8-x}O_{16}$ were synthesized by grinding Mn_2O_3 with V_2O_3 in a mixture of KNO_3 and KCl (1:1 molar ratio of KCl to KNO_3), with at least an eight-fold molar excess of the salt flux mixture. The material was heated at 180 K/hr up to 973 K, soaked for 24 h in ambient atmosphere, then cooled at 180 K/hr. We attempted several compositions for x = 0 - 4. Figure A.1 displays raw PXRD results for samples with x = 0, 1, and 4.

PXRD measurements appeared reasonably clean for samples up to x = 4. However, XPS measurements did not show any vanadium in the surface composition, suggesting that the V cations volatilize during the heating procedure. We did not consider different vanadium sources for this set of experiments, as our initial XRD data appeared to be phase pure. Future work on these materials may yet yield interesting results.

A.5 Conclusions

Our goal was to synthesize mixed metal hollandites with the formula $A_{1.2}Mn_{8-x}M_xO_{16}$ where M = Fe, Ni, Cr or V and A = Ba or K. We changed our initial conditions and reagents in order to improve the methodology. This included different furnace temperatures, the presence of oxidizing or reducing atmospheres, intermediate calcining steps. As mentioned, remaining starting materials were common impurities, which we tried to remove by refiring the samples. Perhaps some starting materi-

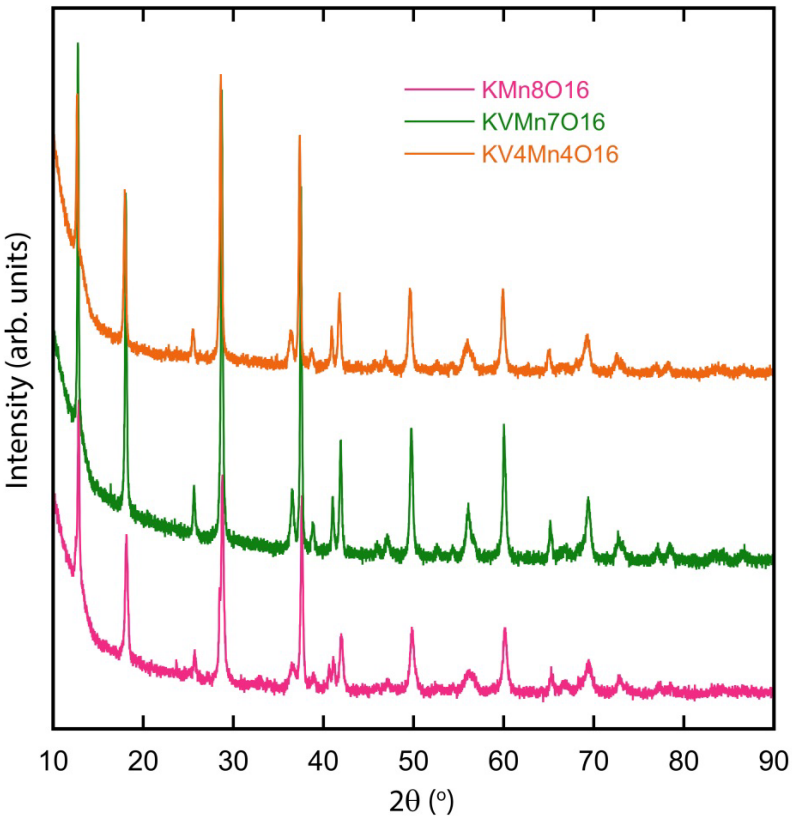

Figure A.1: X-ray powder diffraction data (UMD) for $K_{1.6}V_xMn_{8-x}O_{16}$ at room temperature, for x = 0 (pink), 1 (green), and 4 (orange).

als were not fully reacting because we targeted a stoichiometry that was too optimistic. No phase pure hollandite materials were obtained, although we were close for $Ba_{1.2}Mn_7FeO_{16}$. Future research can be done on these materials, such as using different metal oxides as starting materials (e.g. Fe_3O_4) or nitrates (e.g. $Fe(NO_3)_3$), varying the target and ramping temperatures and improving refiring conditions.

Appendix B: Extended experimental results and information

B.1 $Bi_{1.7}V_8O_{16}$

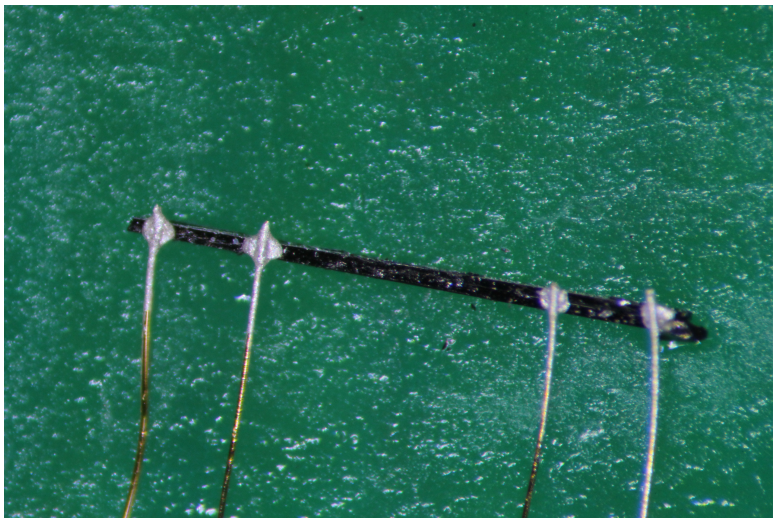

Figure B.1: $Bi_{1.7}V_8O_{16}$ single crystal wired for resistivity measurements.

Bibliography

[1] Turner, S.; Buseck, P. R. *Science* **1979**, *203*, 456–458.

[2] Post, J. E. *Proceedings of the National Academy of Sciences* **1999**, *96*, 3447–3454.

[3] Shen, Y.-f.; Zerger, R. P.; Suib, S. L.; McCurdy, L.; Potter, D. I.; O'Young, C.-L. *Journal of the Chemical Society, Chemical Communications* **1992**, *17*, 1213–1214.

[4] Shen, Y. F.; Zerger, R. P.; Deguzman, R. N.; Suib, S. L.; Mccurdy, L.; Potter, D. I.; O'Young, C. L. *Science* **1993**, *260*, 511–515.

[5] Suib, S. L. *Accounts of chemical research* **2008**, *41*, 479–487.

[6] Post, J. E.; Von Dreele, R. B.; Buseck, P. R. *Acta Crystallographica* **1982**, *B38*, 1056–1065.

[7] Suib, S. L. *Journal of Materials Chemistry* **2008**, *18*, 1623–1631.

[8] Gopalakrishnan, J. *Chemistry of Materials* **1995**, *7*, 1265–1275.

[9] West, A. R. *Basic Solid State Chemistry*, 2nd ed.; John Wiley & Sons, 1999.

[10] Davis, M. E.; Lobo, R. F. *Chemistry of Materials* **1992**, *4*, 756–768.

[11] Li, J.-R.; Kuppler, R. J.; Zhou, H.-C. *Chemical Society Reviews* **2009**, *38*, 1477–1504.

[12] Greedan, J. E. *Journal of Materials Chemistry* **2001**, *11*, 37–53.

[13] Moessner, R. *Canadian Journal of Physics* **2000**, *79*, 1283.

[14] Normand, B. *Contemporary Physics* **2009**, *50*, 533–552.

[15] Wannier, G. H. *Physical Review* **1950**, *79*.

[16] Anderson, P. W. *Physical Review* **1956**, *102*, 1008–1014.

[17] Balents, L. *Nature* **2010**, *464*, 199–208.

[18] Blundell, S. *Magnetism in Condensed Matter*; Oxford University Press, 2001.

[19] Greedan, J. E.; Raju, N. P.; Wills, A. S.; Morin, C.; Shaw, S. M.; Reimers, J. N. *Chem. Mater.* **1998**, *10*, 3058–3067.

[20] Villain, J. *Zeitschrift fur Physik B Condensed Matter and Quanta* **1979**, *33*, 31–42.

[21] Coey, J. M. D. *Magnetism and Magnetic Materials*; 2010; p 614.

[22] Rogado, N.; Lawes, G.; Huse, D. A.; Ramirez, A. P.; Cava, R. J. *Solid State Communications* **2002**, *124*, 229–233.

[23] Williams, M. S.; West, J. P.; Hwu, S.-j. *Chem. Mater.* **2014**, *2*, 2013–2015.

[24] Ramirez, A. P. *Annual Review of Materials Science* **1994**, *24*, 453–480.

[25] Obradors, X.; Labarta, A.; Isalgue, A.; Tejada, J.; Rodriguez, J.; Pernet, M. *Solid State Communications* **1988**, *65*, 189–192.

[26] Ramirez, A. P.; Espinosa, G. P.; Cooper, A. S. *Physical Review Letters* **1990**, *64*, 2070–2073.

[27] Broholm, C.; Aeppli, G.; Espinosa, G. P.; Cooper, a. S. *Physical Review Letters* **1990**, *65*, 3173.

[28] Shores, M. P.; Nytko, E. A.; Bartlett, B. M.; Nocera, D. G. *Journal of the American Chemical Society* **2005**, *127*, 13462–13463.

[29] Singh, R. R. P.; Huse, D. A. *Physical Review B - Condensed Matter and Materials Physics* **2007**, *76*, 1–4.

[30] Ran, Y.; Hermele, M.; Lee, P. A.; Wen, X. G. *Physical Review Letters* **2007**, *98*, 1–4.

[31] Sosin, S. S.; Prozorova, L. A.; Smirnov, A. I.; Golov, A. I.; Berkutov, I. B.; Petrenko, O. A.; Balakrishnan, G.; Zhitomirsky, M. E. *Physical Review B - Condensed Matter and Materials Physics* **2005**, *71*, 1–5.

[32] Subramanian, M. a.; Aravamudan, G.; Rao, G. V. S. *Review Literature And Arts Of The Americas* **1983**, *15*, 55–143.

[33] Gardner, J. S.; Ehlers, G.; Bramwell, S. T.; Gaulin, B. D. *J. Phys.:Condens. Matter* **2004**, *16*, S643–S651.

[34] Ramirez, A. P.; Subramanian, M. A. *Science* **1997**, *277*, 546–549.

[35] Hirakawa, K.; Kadowaki, H.; Ubukoshi, K. *Journal of the Physical Society of Japan* **1985**, *54*, 3526–3536.

[36] Takada, K.; Sakurai, H.; Takayama-muromachi, E. *Nature* **2003**, *422*.

[37] Takada, K.; Sakurai, H.; Takayama-Muromachi, E.; Izumi, F.; Dilanian, R. a.; Sasaki, T. *Advanced Materials* **2004**, *16*, 1901–+.

[38] Li, R. K.; Greaves, C. *Physical Review B* **2003**, *68*, 172403.

[39] Uchiyama, Y.; Sasago, Y.; Tsukada, I.; Uchinokura, K.; Zheludev, A.; Hayashi, T.; Miura, N.; Böni, P. *Physical Review Letters* **1999**, *83*, 632–635.

[40] Hase, M.; Terasaki, I.; Uchinokura, K. *Physical Review Letters* **1993**, *70*, 3651–3654.

[41] Suib, S. L.; Iton, L. E. *Chemistry of Materials* **1994**, *6*, 429–433.

[42] Byström, A.; Byström, A. M. *Acta Crystallographica* **1950**, *3*, 146–154.

[43] Gruner, J. W. *Am. Mineral.* **1943**, *28*, 497–506.

[44] Frondel, C.; Heinrich, E. W. *Am. Mineral* **1942**, *27*, 48–56.

[45] Ramsdell, L. S. *American Mineralogist* **1942**, *149*, 611–613.

[46] Richmond, W. E.; Fleischer, M. *American Mineralogist* **1942**, *149*.

[47] Fermor, L. L. *Transactions of the Mining and Geological Institute of India* **1906**, *1*, 69–136.

[48] Cheary, R. W. *Acta Crystallographica* **1986**, *B42*, 229–236.

[49] Zhang, J.; Burnham, C. W. *American Mineralogist* **1994**, *79*, 168–174.

[50] Rao, C. N. R.; Cheetham, A. K.; Mahesh, R. *Chem. Mater.* **1996**, *8*, 2421–2432.

[51] Ramirez, A. P.; Schiffer, P.; Cheong, S. W.; Chen, C. H.; Bao, W.; Palstra, T. T. M.; Gammel, P. L.; Bishop, D. J.; Zegarski, B. *Physical Review Letters* **1996**, *76*, 3188–3191.

[52] Schiffer, P.; Ramirez, A. P.; Bao, W.; Cheong, S.-W. *Physical Review Letters* **1995**, *75*, 3336–3339.

[53] Khomskii, D. *Spin Electronics* **2001**, 89–116.

[54] Hasegawa, K.; Isobe, M.; Yamauchi, T.; Ueda, H.; Yamaura, J.-I.; Gotou, H.; Yagi, T.; Sato, H.; Ueda, Y. *Physical Review Letters* **2009**, *103*, 146403.

[55] Mahadevan, P.; Kumar, A.; Choudhury, D.; Sarma, D. D. *Physical Review Letters* **2010**, *104*, 256401.

[56] Crespo, Y.; Andreanov, A.; Seriani, N. *Physical Review B* **2013**, *88*, 014202.

[57] Larson, A. M.; Moetakef, P.; Gaskell, K.; Brown, C. M.; King, G.; Rodriguez, E. E. *Chemistry of Materials* **2015**, *27*, 515–525.

[58] Chernova, N.; Ngala, J.; Zavalij, P.; Whittingham, M. *Physical Review B* **2007**, *75*, 014402.

[59] Shimizu, Y.; Okai, K.; Itoh, M.; Isobe, M.; Yamaura, J. I.; Yamauchi, T.; Ueda, Y. *Physical Review B - Condensed Matter and Materials Physics* **2011**, *83*, 155111.

[60] Ishige, Y.; Sudayama, T.; Wakisaka, Y.; Mizokawa, T.; Wadati, H.; Sawatzky, G. A.; Regier, T. Z.; Isobe, M.; Ueda, Y. *Physical Review B* **2011**, *83*, 125112.

[61] Komarek, A. C.; Isobe, M.; Hemberger, J.; Meier, D.; Lorenz, T.; Trots, D.; Cervellino, A.; Fernández-Díaz, M. T.; Ueda, Y.; Braden, M. *Physical Review Letters* **2011**, *107*, 027201.

[62] Feng, Q.; Kanoh, H.; Ooi, K. *Journal of Materials Chemistry* **1999**, *9*, 319–333.

[63] Brock, S. L.; Duan, N. G.; Tian, Z. R.; Giraldo, O.; Zhou, H.; Suib, S. L. *Chemistry of Materials* **1998**, *10*, 2619–2628.

[64] Sato, H.; Yamaura, J.-I.; Enoki, T.; Yamamoto, N. *Journal of Alloys and Compounds* **1997**, *262-263*, 443–449.

[65] Li, W.-N.; Yuan, J.; Gomez-Mower, S.; Sithambaram, S.; Suib, S. L. *The journal of physical chemistry. B* **2006**, *110*, 3066–70.

[66] Endo, T.; Kume, S.; Kinomura, N.; Koizumi, M. *Mat. Res. Bull.* **1976**, *11*, 609–614.

[67] Okada, H.; Kinomura, N.; Kume, S.; Koizumi, M. *Mat. Res. Bull.* **1978**, *13*, 1047–1053.

[68] Horiuchi, S.; Shirakawa, T.; Ohta, Y. *Physical Review B* **2008**, *77*, 155120.

[69] Isobe, M.; Koishi, S.; Kouno, N.; Yamaura, J.-I.; Yamauchi, T.; Ueda, H.; Gotou, H.; Yagi, T.; Ueda, Y. *Journal of the Physics Society Japan* **2006**, *75*, 073801.

[70] Isobe, M.; Koishi, S.; Yamazaki, S.; Yamaura, J.-i.; Gotou, H.; Yagi, T.; Ueda, Y. *Journal of the Physical Society of Japan* **2009**, *78*, 114713.

[71] Leligny, H.; Labbé, P.; Ledésert, M.; Raveau, B.; Valdez, C.; McCarroll, W. H. *Acta Crystallographica Section B Structural Science* **1992**, *48*, 134–144.

[72] Klimczuk, T.; Lee, W.-L.; Zandbergen, H.; Cava, R. *Materials Research Bulletin* **2004**, *39*, 1671–1677.

[73] Toriyama, T.; Watanabe, M.; Konishi, T.; Ohta, Y. *Physical Review B* **2013**, *88*, 235116.

[74] Hyatt, N. C.; Stennett, M. C.; Fiddy, S. G.; Wellings, J. S.; Dutton, S. S.; Maddrell, E. R.; Connelly, A. J.; Lee, W. E. Synthesis and characterisation of transition metal substituted barium hollandite ceramics. Materials Research Society Symposium Proceedings. 2006; pp 583–590.

[75] Moetakef, P.; Larson, A. M.; Hodges, B. C.; Zavalij, P.; Gaskell, K. J.; Piccoli, P. M.; Rodriguez, E. E. *Journal of Solid State Chemistry* **2014**, *220*, 45–53.

[76] Noami, K.; Muraoka, Y.; Wakita, T.; Hirai, M.; Kato, Y.; Muro, T.; Tamenori, Y.; Yokoya, T. *Journal of Applied Physics* **2010**, *107*, 073910.

[77] Pirrotta, I.; Fernandez-Sanjulian, J.; Moran, E.; Alario-Franco, M.; Gonzalo, E.; Kuhn, A.; Garcia-Alvarado, F. *Dalton Transactions* **2012**, *41*, 1840–1847.

[78] Sugiyama, J.; Nozaki, H.; Månsson, M.; Prša, K.; Amato, A.; Isobe, M.; Ueda, Y. *Physics Procedia* **2012**, *30*, 186–189.

[79] Isobe, M.; Koishi, S.; Ueda, Y. *Journal of Magnetism and Magnetic Materials* **2007**, *310*, 888–889.

[80] Toriyama, T.; Konishi, T.; Ohta, Y. *Journal of Physics: Conference Series* **2012**, *391*, 012109.

[81] Shlyk, L.; Niewa, R. *Zeitschrift Fur Naturforschung Section B-A Journal Of Chemical Sciences* **2011**, *66*, 1097–1100.

[82] Cheary, R. W.; Squadrito, R. *Acta Crystallographica Section B Structural Science* **1989**, *45*, 205–212.

[83] Shen, X.; Morey, A. M.; Liu, J.; Ding, Y.; Cai, J.; Durand, J.; Wang, Q.; Wen, W.; Hines, W. A.; Hanson, J. C.; Bai, J.; Frenkel, A. I.; Reiff, W.; Aindow, M.; Suib, S. L. *The Journal of Physical Chemistry* **2011**, *115*, 21610–21619.

[84] Cai, J.; Liu, J.; Gao, Z.; Navrotsky, A.; Suib, S. L. *Chemistry of Materials* **2001**, 4595–4602.

[85] Barbato, S.; Gautier, J. L. *Electrochimica Acta* **2001**, *46*, 2767–2776.

[86] Aubin-Chevaldonnet, V.; Deniard, P.; Evain, M.; Leinekugel-Le-Cocq-Errien, A. Y.; Jobic, S.; Courant, D.; Petricek, V.; Advocat, T. *Zeitschrift fuer Kristallographie* **2007**, *222*, 383–390.

[87] Liu, S. et al. *Scientific Reports* **2014**, *4*, 6203.

[88] Carter, R. L. *Molecular Symmetry and Group Theory*; 2005.

[89] Ching, S.; Driscoll, P. F.; Kieltyka, K. S.; Marvel, M. R.; Suib, S. L. *Chem. Commun.* **2001**, 2486–2487.

[90] Chen, X.; Shen, Y.-F.; Suib, S. L.; O'Young, C. L. *Chem. Mater.* **2002**, *14*, 940–948.

[91] Pahalagedara, L. R.; Dharmarathna, S.; King'ondu, C. K.; Pahalagedara, M. N.; Meng, Y.-T.; Kuo, C.-H.; Suib, S. L. *Journal Of Physical Chemistry C* **2014**, *118*, 20363–20373.

[92] Kijima, N.; Sakao, M.; Tanuma, Y.; Kataoka, K.; Igarashi, K.; Akimoto, J. *Solid State Ionics* **2013**, 10–13.

[93] Kadoma, Y.; Oshitari, S.; Ui, K.; Kumagai, N. *Solid State Ionics* **2008**, *179*, 1710–1713.

[94] Bursill, L. A.; Grzinic, G. *Acta Crystallographica* **1980**, *B36*, 2902–2913.

[95] Sasaki, T.; Komaba, S.; Kumagai, N.; Nakai, I. *Electrochemical and Solid-State Letters* **2005**, *8*, A471–A475.

[96] Zhang, X.; Xu, Z.; Tang, S.; Deng, Y.; Du, Y. **2011**, 2852–2857.

[97] Huang, H.; Meng, Y.; Labonte, A.; Dobley, A.; Suib, S. L. **2013**,

[98] Kijima, N.; Ikeda, T.; Oikawa, K.; Izumi, F.; Yoshimura, Y. *Journal of Solid State Chemistry* **2004**, *177*, 1258–1267.

[99] Yamamoto, N.; Endo, T.; Shimada, M.; Takada, T. *Japan Journal of Applied Physics* **1974**, *13*, 723–724.

[100] Luo, J.; Zhu, H. T.; Liang, J. K.; Rao, G. H.; Li, J. B.; Du, Z. M. **2010**, 8782–8786.

[101] Kadoma, Y.; Akahira, T.; Fukuda, T.; Ui, K.; Kumagai, N. *Functional Materials Letters* **2012**, *05*, 1250004.

[102] Kato, H.; Waki, T.; Kato, M.; Yoshimura, K.; Kosuge, K. *Journal of the Physical Society of Japan* **2001**, *70*, 325–328.

[103] Talanov, A.; Phelan, W. A.; Kelly, Z. A.; Siegler, M. A.; McQueen, T. M. *Inorganic chemistry* **2014**, *53*, 4500–4507.

[104] Ishiwata, S.; Bos, J. W. G.; Huang, Q.; Cava, R. J. *Journal Of Physics-Condensed Matter* **2006**, *18*, 3745–3752.

[105] Yang, X.; Tang, W.; Feng, Q.; Ooi, K. *Crystal Growth & Design* **2003**, *3*, 409–415.

[106] Yu, J.; Tang, S.; Wang, L.; Du, Y. *Chemical Physics Letters* **2010**, *496*, 117–121.

[107] Pecharsky, V. K.; Zavalij, P. Y. *Fundamentals of Powder Diffraction and Structural Characterization of Materials*; Springer Science + Business Media, LLC: New York, 2009.

[108] Hammond, C. *The Basics of Crystallography and Diffraction: Third Edition*; 2009.

[109] Dianoux, A.-J., Lander, G., Eds. *Neutron Data Booklet*, 2nd ed.; Old City Publishing Group: Philadelphia, PA, 2003.

[110] Brown, C. M. High Resolution Powder Diffractometer - BT1. 2015; www.ncnr.nist.gov/instruments/bt1/.

[111] NCNR, NIST Center for Neutron Research. 2017; https://ncnr.nist.gov/.

[112] Neutron Sciences. 2017; https://neutrons.ornl.gov/content/how-sns-works.

[113] Rietveld, H. M. *Journal of Applied Crystallography* **1969**, *2*, 65–71.

[114] Rodriguez-Carvajal, J. *Physica B* **1993**, *192*, 55–69.

[115] Cheary, R. W.; Squadrito, R. *Acta Crystallographica Section A Foundations of Crystallography* **1992**, *48*, 15–27.

[116] Goodenough, J. B. *Physical Review* **1955**, *100*, 564–573.

[117] Goodenough, J. B. *Journal of Physics and Chemistry of Solids* **1958**, *6*, 287–297.

[118] Kanamori, J. *J. Phys. Chem. Solids* **1959**, *10*, 87–98.

[119] Zener, C. *Physical Review* **1951**, *82*, 403–405.

[120] Carlin, R. L. *Magnetochemistry*; Springer-Verlag Berlin Heidelberg, 1986; Vol. 1; p 328.

[121] Shull, C.; Smart, J. S. *Physical Review* **1949**, *76*.

[122] Shull, C.; Strauser, W. A.; Wollan, E. O. *Physical Review* **1951**, *83*, 333–345.

[123] Wills, A. S. *Physica B* **2000**, *276-278*, 680–681.

[124] Van der Pauw, L. J. *Philips Technical Review* **1958**, *20*, 220–224.

[125] DeGuzman, R. N.; Awaluddin, A.; Shen, Y.-f.; Tian, Z. R.; Suib, S. L.; Ching, S.; Oyoung, C.-l. *Chemistry of Materials* **1995**, *7*, 1286–1292.

[126] Thurber, W. R. The Hall Effect. 2016; www.nist.gov/pml/engineering-physics-division/hall-effect.

[127] Cox, P. A. *The Electronic Structure and Chemistry of Solids*; Oxford University Press: Oxford, UK, 1987.

[128] Post, J. E.; Burnham, C. W. *American Mineralogist* **1986**, *71*, 1178–1185.

[129] Baur, W. H. *Acta Crystallographica Section B Structural Crystallography and Crystal Chemistry* **1976**, *32*, 2200–2204.

[130] Shannon, R. D. *Acta Crystallographica* **1976**, *A32*, 751–767.

[131] Brown, I. D.; Altermatt, D. *Acta Crystallographica* **1985**, *41*, 244–247.

[132] Brese, N. E.; O'Keeffe, M. *Acta Crystallographica Section B Structural Science* **1991**, *47*, 192–197.

[133] O'Keeffe, M.; Brese, N. E. *Journal of the American Chemical Society* **1991**, *113*, 3226–3229.

[134] Militello, M. C.; Gaarenstroom, S. W. *Surface Science Spectra* **2001**, *8*, 207.

[135] Stranick, M. A. *Surface Science Spectra* **1999**, *6*, 39.

[136] Stranick, M. A. *Surface Science Spectra* **1999**, *6*, 31.

[137] Oku, M.; Sato, Y. *Applied Surface Science* **1992**, *55*, 37–41.

[138] Melot, B. C.; Drewes, J. E.; Seshadri, R.; Stoudenmire, E. M.; Ramirez, A. P. *Journal of Physics: Condensed Matter* **2009**, *21*, 216007.

[139] Sato, H.; Enoki, T.; Yamaura, J.-I.; Yamamoto, N. *Physical Review B* **1999**, *59*, 12836–12841.

[140] Coleman, L. B. *The Review of scientific instruments* **1978**, *49*, 58.

[141] Mandal, S.; Andreanov, A.; Crespo, Y.; Seriani, N. *Physical Review B* **2014**, *90*, 104420.

[142] Hill, N. A. *The Journal of Physical Chemistry B* **2000**, *104*, 6694–6709.

[143] Ederer, C.; Spaldin, N. A. *Nature Materials* **2004**, *3*, 849–851.

[144] Risbud, A. S.; Spaldin, N. A.; Chen, Z. Q.; Stemmer, S.; Seshadri, R. *Physical Review B* **2003**, *68*, 205202.

[145] Van Aken, B. B.; Palstra, T. T. M.; Filippetti, A.; Spaldin, N. A. *Nature materials* **2004**, *3*, 164–170.

[146] Baettig, P.; Spaldin, N. A. *Applied Physics Letters* **2005**, *86*, 012505.

[147] Toriyama, T.; Nakao, A.; Yamaki, Y.; Nakao, H.; Murakami, Y.; Hasegawa, K.; Isobe, M.; Ueda, Y.; Ushakov, A. V.; Khomskii, D. I.; Streltsov, S. V.; Konishi, T.; Ohta, Y. *Physical Review Letters* **2011**, *107*, 266402.

[148] Ahmed, K. A. M.; Li, B.; Tan, B.; Huang, K. *Solid State Sciences* **2013**, *15*, 66–72.

[149] Ching, S.; Franklin, J. P.; Spencer, C. M. *Polyhedron* **2013**, *58*, 53–59.

[150] Ching, S.; Petrovay, D. J.; Jorgensen, M. L.; Suib, S. L. *Inorganic Chemistry* **1997**, *36*, 883–890.

[151] Cui, H.-J.; Shi, J.-W.; Fu, M.-L. *Journal of Cluster Science* **2012**, *23*, 607–614.

[152] O'Young, C.-L.; Suib, S. L. Octahedral Molecular Sieve Possessing (4x4) Tunnel Structure and Method of its Production. 1996.

[153] Shen, X.-f.; Ding, Y.-s.; Hanson, J. C.; Aindow, M.; Suib, S. L. *Journal of the American Chemical Society* **2006**, *128*, 4570–4571.

[154] Tang, X.; Li, J.; Hao, J. *Catalysis Communications* **2010**, *11*, 871–875.

[155] Händel, M.; Rennert, T.; Totsche, K. U. *Journal of colloid and interface science* **2013**, *405*, 44–50.

[156] Hashem, A. M. A.; Mohamed, H. A.; Bahloul, A.; Eid, A. E.; Julien, C. M. *Ionics* **2007**, *14*, 7–14.

[157] King'ondu, C. K.; Opembe, N.; Chen, C.-h.; Ngala, K.; Huang, H.; Iyer, A.; Garces, H. F.; Suib, S. L. *Advanced Functional Materials* **2010**, *21*, 312–323.

[158] Luo, J.; Zhu, H. T.; Zhang, F.; Liang, J. K.; Rao, G. H.; Li, J. B.; Du, Z. M. *Journal of Applied Physics* **2009**, *105*, 2–7.

[159] Meng, Y.; Song, W.; Huang, H.; Ren, Z.; Chen, S.-Y.; Suib, S. L. *Journal of the American Chemical Society* **2014**, *136*.

[160] Shen, X.-F.; Ding, Y.-S.; Liu, J.; Han, Z.-H.; Budnick, J. I.; Hines, W. a.; Suib, S. L. *Journal of the American Chemical Society* **2005**, *127*, 6166–7.

[161] Sun, M.; Ye, F.; Lan, B.; Yu, L.; Cheng, X.; Liu, S.; Zhang, X. *International Journal of Electrochemical Science* **2012**, *7*, 9278–9289.

[162] Son, Y.-c.; Makwana, V. D.; Howell, A. R.; Suib, S. L. *Angewandte Chemie International Edition* **2001**, *40*, 4280–4283.

[163] Espinal, A. E.; Yan, Y.; Zhang, L.; Espinal, L.; Morey, A.; Wells, B. O.; Aindow, M.; Suib, S. L. *Small (Weinheim an der Bergstrasse, Germany)* **2014**, *10*, 66–72.

[164] Liu, J.; Son, Y.-c.; Cai, J.; Shen, X.; Suib, S. L.; Aindow, M. *Chem. Mater.* **2004**, *16*, 276–285.

[165] Kuwabara, T.; Isobe, M.; Gotou, H.; Yagi, T.; Nishio-Hamane, D.; Ueda, Y. *Journal Of The Physical Society Of Japan* **2012**, *81*, ARTN 104701.

[166] Strobel, P.; Le Page, Y. *Journal of Crystal Growth* **1982**, *56*, 645–651.

[167] Strobel, P.; Vicat, J.; Qui, D. T. *Journal of Solid State Chemistry* **1984**, *55*, 67–73.

[168] Vicat, J.; Fanchon, E.; Strobel, P.; Qui, D. T. *Acta Cryst.* **1986**, *B42*, 162–167.

[169] Chen, Y.; Lynn, J. W.; Huang, Q.; Woodward, F. M.; Yildirim, T.; Lawes, G.; Ramirez, A. P.; Rogado, N.; Cava, R. J.; Aharony, A.; Entin-Wohlman, O.; Harris, A. B. *Physical Review B - Condensed Matter and Materials Physics* **2006**, *74*, 1–12.

[170] Kachi, S.; Kosuge, K.; Okinaka, H. *Journal of Solid State Chemistry* **1973**, *6*, 258–270.

[171] Isobe, M.; Ueda, Y. *Journal of the Physical Society of Japan* **1996**, *65*, 1178–1181.

[172] Seo, H.; Fukuyama, H. *Journal of the Physics Society Japan* **1998**, *67*, 2602–2605.

[173] Botana, A. S.; Pardo, V.; Baldomir, D.; Ushakov, A. V.; Khomskii, D. I. *Physical Review B - Condensed Matter and Materials Physics* **2011**, *84*, 1–8.

[174] Ohama, T.; Yasuoka, H.; Isobe, M.; Ueda, Y. *Physical Review B* **1999**, *59*, 3299–3302.

[175] Yamada, H.; Ueda, Y. *Journal of the Physical Society of Japan* **1999**, *68*, 2735–2740.

[176] Isobe, M.; Ueda, Y. *Molecular Crystals and Liquid Crystals Science and Technology. Section A. Molecular Crystals and Liquid Crystals* **2000**, *341*, 271–276.

[177] Corr, S. A.; Shoemaker, D. P.; Melot, B. C.; Seshadri, R. *Physical Review Letters* **2010**, *105*, 1–4.

[178] Liu, M.; Hwang, H. Y.; Tao, H.; Strikwerda, A. C.; Fan, K.; Keiser, G. R.; Sternbach, A. J.; West, K. G.; Kittiwatanakul, S.; Lu, J.; Wolf, S. a.; Omenetto, F. G.; Zhang, X.; Nelson, K. a.; Averitt, R. D. *Nature* **2012**, *487*, 345–8.

[179] Qazilbash, M. M.; Brehm, M.; Chae, B.-G.; Ho, P.-C.; Andreev, G. O.; Kim, B.-J.; Yun, S. J.; Balatsky, A. V.; Maple, M. B.; Keilmann, F.; Kim, H.-T.; Basov, D. N. *Science* **2007**, *318*, 1750–1753.

[180] Whittaker, L.; Patridge, C. J.; Banerjee, S. *Journal of Physical Chemistry Letters* **2011**, *2*, 745–758.

[181] Biermann, S.; Poteryaev, A.; Lichtenstein, A. I.; Georges, A. *Physical Review Letters* **2005**, *94*, 1–4.

[182] Kim, S.; Kim, B. H.; Kim, K.; Min, B. I. *Physical Review B* **2016**, *93*, 045106.

[183] Abraham, F.; Mentre, O. *Journal of Solid State Chemistry* **1994**, *109*, 127–133.

[184] Sheldrick, G. M. *Acta Cryst. A* **2008**, *64*, 112–122.

[185] Sheldrick, G. M. *Bruker SHELXTL Software* **2012**,

[186] Isobe, M.; Koishi, S.; Ueda, Y. *Journal of Physics: Conference Series* **2008**, *121*, 032007.

[187] Waki, T.; Kato, H.; Kato, M.; Yoshimura, K. *Journal of Physics and Chemistry of Solids* **2002**, *63*, 961–964.

[188] Waki, T.; Kato, H.; Kato, M.; Yoshimura, K. *Journal of the Physics Society Japan* **2004**, *73*, 275–279.

[189] Carter, M. L.; Withers, R. L. *Z. Kristallogr.* **2004**, *219*, 763–767.

[190] Carter, M. L.; Withers, R. L. *Journal of Solid State Chemistry* **2005**, *178*, 1903–1914.

[191] Maignan, A.; Lebedev, O. I.; Van Tendeloo, G.; Martin, C.; Hébert, S. *Physical Review B* **2010**, *82*, 035122.

[192] Wu, X.; Fujiki, Y.; Ishigame, M.; Horiuchi, S. *Acta Crystallographica Section A* **1991**, *47*, 405–413.

[193] Kanke, Y.; Takayama-Muromachi, E.; Kato, K.; Kosuda, K. *Journal of Solid State Chemistry* **1994**, *113*, 125–131.

[194] Mentre, O.; Dhaussy, A.-C.; Abraham, F. *Journal of Materials Chemistry* **1999**, *9*, 1023–1027.

[195] Shibata, Y.; Ohta, Y. *Journal of the Physical Society of Japan* **2002**, *71*, 513–518.

[196] Waki, T.; Kato, M.; Yoshimura, K. *Physica B: Condensed Matter* **2005**, *359-361*, 1309–1311.

[197] Bonner, J. C.; Fisher, M. E. *Physical Review* **1964**, *135*, A640–A658.

[198] Bleaney, B.; Bowers, K. D. *Proc. Roy. Soc.* **1952**, *A214*, 451–465.